UNIVERSITY OF OKLAHOMA

GRADUATE COLLEGE

SIMULATED IMPACTS OF TROPOPAUSE-PENETRATING CONVECTION ON THE CHEMICAL COMPOSITION OF THE UPPER TROPOSPHERE AND LOWER STRATOSPHERE

A DISSERTATION

SUBMITTED TO THE GRADUATE FACULTY

in partial fulfillment of the requirements of the

Degree of

DOCTOR OF PHILOSOPHY

BY

DANIEL PHOENIX
Norman, Oklahoma
2019

SIMULATED IMPACTS OF TROPOPAUSE-PENETRATING CONVECTION ON THE CHEMICAL COMPOSITION OF THE UPPER TROPOSPHERE AND LOWER STRATOSPHERE

A DISSERTATION APPROVED FOR THE
SCHOOL OF METEOROLOGY

BY THE COMMITTEE CONSISTING OF

Dr. Cameron Homeyer, Chair

Dr. Richard Zielinski

Dr. Petra Klein

Dr. Steven Cavallo

Dr. Xiaoming Hu

Dr. Mary Barth

Acknowledgments

The author acknowledges ECMWF for providing the ERA-Interim reanalysis output, which were obtained from the Research Data Archive (RDA) maintained by the Computational and Informational Systems Laboratory (CISL) at the National Center for Atmospheric Research (NCAR); the original data are available at http://has.ncdc.noaa.gov/ and http://rda.ucar.edu/, respectively. The author also acknowledges use of MOZART-4 global model output available at http://www.acom.ucar.edu/wrf-chem/mozart.shtml, the use of the WRF-Chem preprocessor tool {mozbc, fire_emiss, etc.} provided by the Atmospheric Chemistry Observations and Modeling Lab (ACOM) of NCAR, and Stu Mckeen for (NOAA/ESRL) for providing 4 km gridded anthropogenic emissions from the EPA Inventory, and the National Center for Atmospheric Research is supported by the National Science Foundation. The high-performance computing support from Cheyenne (doi:10.5065/D6RX99HX), used for part of this project, was provided by NCAR's Computational and Information Systems Laboratory, sponsored by the National Science Foundation. Additional computing for this project was performed at the OU Supercomputing Center for Education & Research (OSCER) at the University of Oklahoma (OU). This work was supported by the National Science Foundation grant number AGS-1522910. The author acknowledges the NCAR Advanced Study Program, Atmospheric Chemistry, Observation, and Modeling (ACOM) laboratory, and Mesoscale and Microscale Meteorology (MMM) laboratory for supporting an extended visit to work on part of this dissertation, as well as Drs. Mary Barth and Stanley Trier for co-sponsoring the visit and their contributions to the project. The author thanks Drs. Ken Bowman, Gretchen Mullendore, Laura Pan, and Ted Mansell for their useful discussions related to this work. Lastly, the author thanks the committee members—Drs. Petra Klein, Steven Cavallo, Xiaoming Hu, Richard Zielinski, and Mary Barth—and advisor, Dr. Cameron Homeyer, for their useful feedback and contributions throughout the project.

Table of Contents

List of Tables

List of Figures

Abstract

Tropopause-penetrating convection is capable of rapidly transporting air from the lower troposphere to the upper troposphere and lower stratosphere (UTLS). Since the vertical redistribution of gases in the atmosphere by convection can have important impacts on the chemistry of the UTLS, the radiative budget, and climate, it has become a recent focus of observational and modeling studies. Despite being otherwise limited in space and time, recent aircraft observations from field campaigns such as the Deep Convective Clouds and Chemistry experiment have provided new high-resolution observations of convective transport. Modeling studies, on the other hand, offer the advantage of providing high-resolution spatially and temporally continuous output related to the physical, dynamical, and chemical characteristics of storms and their environments. While it is currently known that stratosphere-to-troposphere transport and troposphere-to-stratosphere transport are possible, it is not understood what mechanisms are responsible for transport and what impact convection has on UTLS composition.

Since the characteristics of simulated convection depend on the chosen model design, the sensitivity of simulated convective transport to the choice of physical (bulk microphysics or BMP and planetary boundary layer or PBL) and chemical parameterizations was examined in the Weather Research and Forecasting model coupled with Chemistry (WRF-Chem). In particular, multiple cases where in situ observations are available from the recent (2012) Deep Convective Clouds and Chemistry (DC3) experiment were simulated. Model output is evaluated using ground-based radar observations of each storm and in situ trace gas observations from two aircraft operated during the DC3 experiment. Model results show measurable sensitivity of the physical characteristics of a storm and the transport of water vapor and additional trace gases into the UTLS to the choice of BMP. The physical characteristics of the storm and transport of insoluble trace gases are largely insensitive to the choice of PBL scheme and chemical mechanism, though several soluble trace gases (e.g., SO_2, CH_2O, HNO_3) exhibit some measurable sensitivity.

To evaluate the mechanisms responsible for stratosphere-to-troposphere transport of ozone-rich air, high-resolution simulations of a case with observed stratosphere-to-troposphere transport around the anvil of a mesoscale convective system (MCS) were performed using WRF-Chem. Several hypotheses, which include dynamic instabilities, mass conservation, and ageostrophic circulations driven by pressure perturbations are evaluated. Model results suggest that this transport pathway occurs as a two-step process: (1) downwelling that is driven by mass conservation as the MCS deposits air into the UTLS and (2) differential advection of outflow air in the upper troposphere, which wraps high ozone air around and under the MCS anvil. Dynamic instabilities are not a leading contributor to this transport process. Although WRF-Chem appears to adequately simulate this transport, trajectory calculations indicate that the transported air does not originate above the lapse-rate tropopause (LRT). Since observations showed ozone mixing ratios in excess of 200 ppb (typical of the lower stratosphere), this suggests that the model did not fully represent this transport process.

To examine the impact of tropopause-penetrating convection on the chemical composition of the UTLS, two 10-day periods of high frequency, tropopause-penetrating convection over the United States were simulated with WRF-Chem. One period representative of springtime convection (May 18-27, 2011) and one period representative of summertime convection (August 5-15, 2013) were chosen to examine the differences in convective transport between the two seasons. Overall, springtime convection has a larger impact than summertime convection, with a net effect of increasing water vapor in the lower stratosphere and increasing ozone in the upper troposphere. Springtime convection frequently increases the water vapor mixing ratio in the lowermost stratosphere by over 20% while changes in stratospheric water vapor from summertime convection are much lower (~7-11% increase). Increases in the upper tropospheric ozone mixing ratio range from 8-19% from springtime convection and are minimal from summertime convection. Changes in the composition of the UTLS are largely sensitive to the height of the tropopause, with the largest changes being in environments with tropopause heights between 11 and 13 km (typical of springtime environments in the United States). An objective algorithm to detect stratosphere-to-troposphere transport of ozone-rich air shows that while this air occasionally descends in the troposphere around

the anvil of convective storms, the air is of upper tropospheric origin and little air comes from the stratosphere. The algorithm suggests that large springtime convective systems in low-tropopause environments are most responsible for this downward transport.

Chapter 1

Introduction and Background

1.1 Stratosphere-Troposphere Exchange

Stratosphere-troposphere exchange (STE) is an important mixing event in which mass and chemical species are transported between the troposphere and stratosphere. Mixing of stratospheric and tropospheric air masses can have significant impacts on the chemistry and radiation budget of those layers. Many processes contribute to STE, including large-scale processes such as the Brewer-Dobson circulation, stratospheric intrusions, and transport along the warm conveyor belt of an extratropical cyclone. In general, these large-scale processes have been studied extensively, and are fairly well understood [*Holton et al*., 1995]. In recent years, STE from deep convection has received considerable attention.

1.1.1 Chemical Composition of the UTLS

Water vapor (H_2O), ozone (O_3), and carbon monoxide (CO) in the troposphere and stratosphere are ideal tracers for transport studies due to their lifetime and unique composition in each layer. Here, the typical UTLS composition of each will be discussed. H_2O is highly variable in the atmosphere. In the troposphere, the H_2O content of the air is tied to the availability of liquid/solid water and the efficiency of the evaporation/sublimation process near the surface. In general, H_2O decreases with height from O(10^5 ppm) near the surface to ~5-10 ppm in the stratosphere. The mixing ratio of H_2O in the stratosphere is primarily controlled by large-scale transport from the troposphere in the tropics [*Brewer*, 1949] and also from methane oxidation in the stratosphere [*LeTexier et al.,* 1998]. The amount of H_2O that can be transported across the tropopause depends on the coldest temperature the air will encounter [*Mote et al*., 1996; *Holton et al*., 1995; *Sherwood and Dessler*, 2001; *Fueglistaler et al*., 2009]. Changes in the cold point have been linked to changes in stratospheric H_2O and are expected to dominate the H_2O variations in the lowermost stratosphere [*Solomon et al.*,

2010]. The contribution of methane oxidation to stratospheric H_2O is low, especially near the tropopause, and estimates of the radiative forcing from such changes are small [*Rohs et al*., 2006].

There are several known and well-understood sources of O_3 in the troposphere and these include: 1) photochemical production in the upper troposphere [e.g., *Chameides,* 1978; *Liu et al.*, 1980; *Jaeglé et al.,* 1998], especially in convective outflow regions where lightning-generated nitrogen oxides (LNOx) accelerate O_3 production [e.g. Pickering et al., 1990], 2) slow downward transport from the stratosphere via large scale circulation and synoptic-scale dynamical processes [*Holton et al*., 1995; *Sprenger and Wernli*, 2003; *Hsu et al*., 2005] such as stratospheric intrusions [*Danielson*, 1968; *Shapiro*, 1980; *Pan et al.,* 2010; *Lin et al.,* 2012; *Langford et al*., 2012], and 3) production from anthropogenic and natural precursors near the surface [e.g., *Logan,* 1985; *Lelieveld and Dentener,* 2000] that are subsequently lofted by convection and other mechanisms. Tropospheric O_3 is low compared to that in the stratosphere. O_3 may be high close to the surface in urban areas, in which mixing ratios can be high enough to affect human health and cause damage to plants and buildings. In general, however, it is typically less than ~80 ppb throughout the depth of the troposphere and increases sharply around the tropopause. Stratospheric O_3 is primarily controlled by photochemical production and loss involving nitrogen oxides (NO_X = NO + NO_2), hydrogen oxides (HO_X = OH + HO_2), and oxygen and generally peaks at about 10 ppm in the mid-stratosphere (between ~20-30 km).

CO is generally produced by oxidation of methane and nonmethane hydrocarbons and fossil fuel combustion and is abundant in the boundary layer [e.g., *Levy*, 1973; *Crutzen*, 1973], particularly in biomass burning plumes originating from the surface [*Duncan et al*., 2003]. Above the boundary layer, CO mixing ratios are fairly constant and decrease sharply at the tropopause. While sources of CO are generally high near the surface, CO can be transported to the UTLS through large-scale and small-scale processes, and most efficiently by deep convection. Unlike H_2O, CO is not removed by condensation, and while it is oxidized by OH [e.g., *Levy*, 1973; *Crutzen*, 1973], there are no UT sources of CO, unlike with O_3. Therefore, CO acts as a fairly good tropospheric tracer for transport studies.

1.1.2 Transport Pathways

Transport and mixing can occur in both the upward and downward directions: stratosphere-to-troposphere transport (STT) and troposphere-to-stratosphere transport (TST). Both transport types can occur through several pathways. TST primarily occurs through the Brewer-Dobson circulation, which is characterized by slow ascent of tropospheric air in the tropics, poleward transport in the stratosphere, and subsidence in the extratropics, which takes several years to complete [*Brewer*, 1949; *Dobson*, 1946]. Other transport pathways take place on timescales of ~days-weeks, including upwelling in the Asian monsoon anticyclone [*Randel et al*., 2010] and quasi-lateral isentropic transport of tropical upper troposphere air into the extratropical lower stratosphere above the subtropical jet [e.g., *Olsen et al*., 2008; *Olsen et al.,* 2010; *Pan et al*., 2009; *Pan et al*., 2010]. The latter has been found to occur during large-scale Rossby wave breaking events [e.g., *Newman and Schoeberl*, 1995; *Vaughan and Timmis*, 1998; *O'Connor et al*., 1999; *Bradshaw et al*., 2002], which not only transports TTL air into the lower most stratosphere (LMS), but also extratropical LS air into the tropical UT [e.g., *Waugh and Polvani*, 2000; *Waugh*, 2005].

TST from deep convection differs from the aforementioned processes in that it occurs rapidly, such that air may be transported from the boundary layer to the UTLS in less than one hour [*Mullendore et al.*, 2005]. The pathway is particularly efficient in transporting very short-lived species (VSLS) from the surface, preserving the chemical mixing ratio of the air while synoptic scale and turbulent mixing would require days and months, respectively, to achieve the same mixing [*Sigmond et al.*, 2000; *Dickerson*, 1987]. The rapid transport of these gases [*Mullendore et al.* 2005], many of which typically have a short lifetime near the surface, can have a large impact on the chemistry of the UTLS [*Barth et al.,* 2012] as will be discussed in the following section.

An important pathway for STT is stratospheric intrusions, or tropopause folds, which can lead to irreversible transport of stratospheric air if inertia-gravity waves [e.g., *Danielsen et al*., 1991], Kelvin-Helmholtz instabilities [e.g., *Shapiro*, 1980], boundary layer mixing [e.g., *Johnson and Viezee*, 1981], or diabatic processes such as latent heating and radiative cooling from clouds near the tropopause [e.g., *Price and Vaughan*, 1993; *Lamarque and Hess*, 1994] occur along the boundary between troposphere and

stratosphere air. Convective injection into a stratospheric intrusion may also lead to irreversible mixing and could potentially have large impacts given the deep descent of stratospheric intrusions and the rapid transport of air in a convective updraft. Recent observations have also shown that stratospheric air is capable of being wrapped around the anvil of an MCS and into the upper troposphere [*Pan et al*., 2014]. While this transport process was the focus of speculation in previous studies [*Dickerson et al*., 1987; *Poulida et al*., 1996; *Stenchikov et al.,* 1996], the observations presented in *Pan et al*. [2014] were the first unambiguous presentation of this process.

1.1.3 Effects on Chemistry and the Radiation Budget

Cross-tropopause mixing has an important impact on the chemistry and radiation budget of the UTLS. The UTLS layer is typically characterized by sharp gradients in O_3, CO, H_2O, and other trace gases. O_3 and H_2O are particularly important because they are greenhouse gases in the UTLS and changing their mixing ratios has important impacts on the radiation budget of the troposphere and stratosphere [e.g., *Forster and Shine,* 1999].

Lacis et al. [1990] showed that O_3 variations in the UTLS are most effective in changing the radiative forcing because the greenhouse efficiency on a per molecule basis is greatest for O_3 changes around the tropopause. O_3 is particularly complex because it absorbs both shortwave (solar) and longwave (infrared) radiation, and plays a large role in determining the energy balance of the troposphere and stratosphere. Furthermore, mixing ratios of other radiatively active and inactive gases are capable of affecting O_3 mixing ratios, particularly in the stratosphere where they play a role in O_3 destruction [*WMO*, 1982; *WMO*, 1986]. It is also possible that other trace gases may react and thereby modify O_3 in the UTLS, which may produce a significant climate forcing since the greenhouse effect is larger for O_3 in the troposphere than stratosphere [*Ramanathan and Dickerson*, 1979; *Wang et al*., 1980].

Solomon et al., [2010] showed that increases (decreases) in stratospheric H_2O result in troposphere warming (cooling) and others have suggested that changes in stratospheric H_2O may have a significant effect on climate change [*Forster and Shine*, 1999; *Smith et al.*, 2001; *Shindell*, 2001]. Stratospheric H_2O primarily absorbs outgoing longwave (infrared) radiation, but also absorbs some incoming shortwave (solar)

radiation. Kernal function calculations for vertical changes (i.e., the radiative forcing per layer) show that the influence of stratospheric H_2O on longwave radiation is larger than shortwave radiation with the highest peak in the kernel function around the tropopause [*Solomon et al*., 2010].

Convection is also important because it can uniquely and rapidly transport VSLS to the UTLS. Specifically, transported species such as non-methane hydrocarbons (NMHCs), peroxides, formaldehyde (CH_2O), and methanol (CH_3OH), can react to form HO_2 and RO_2 and produce O_3 [e.g., *Pickering et al.,* 1992] while lightning-produced nitrogen oxides (LNOx) are also an important precursor in O_3 production [*Ridley et al.,* 1994, 2004]. NMHCs, sulfur dioxide (SO_2), and volatile organic compounds (VOCs) can react and create new aerosols when transported to the UT [e.g., *Thornton et al.,* 1997]. Some halogen species can be transported to the stratosphere where they can affect O_3 chemistry [*Dvortsov et al.,* 1999]. As noted, the exchange of longer-lived greenhouse gases such as O_3 and H_2O within convection and from other processes can significantly impact the radiation budget [e.g., *Forster and Shine,* 1999].

The recent observation of STT of O_3-rich air around an MCS anvil is potentially important for our understanding of O_3 in the UTLS. First, it challenges the current understanding of the impact of LNO_X on the production of upper tropospheric O_3. A summertime enhancement in upper troposphere O_3 is typically observed in the SE United States and has been attributed to photochemical production from LNOx [*Cooper et al*., 2006; 2007]. This additional transport pathway from the stratosphere complicates the understanding of LNOx-induced O_3 production since this process was previously unaccounted for [*Jourdain et al.,* 2010; *Barth et al.,* 2012]. Secondly, global climate models do not consider this transport process because they cannot resolve convective transport. Since hundreds of tropopause-reaching/overshooting convective storms occur over the United States each year, this could be a significant source of UT O_3 [*Bedka et al.,* 2010; *Cooney et al.,* 2018].

1.2 Transport Mechanisms in Convection

It is desirable to understand the mechanisms responsible for irreversible transport. Understanding these processes not only helps to clarify the transport mechanisms, but

also provides a conceptual basis for in situ aircraft measurements. Furthermore, such knowledge will afford modelers the ability to perform quantitative computations so as to obtain more accurate estimates and better transport parameterizations for global models. *Wang et al*. [2003] investigated the transport of H_2O into the lower stratosphere with high resolution numerical simulations. The results showed that breaking gravity waves at cloud top can cause H_2O and cloud ice to be injected into the stratosphere in the form of plumes above a thunderstorm anvil. The study found that there are two types of plumes, anvil sheet plumes and overshooting plumes, and that the injection process is diabatic. Other convectively-driven transport processes, such as the transport of stratospheric air around an MCS anvil, are not fully understood. Given the importance of UT O_3 on the radiation budget and UT chemistry, it is important to understand the mechanisms responsible.

1.3 Tropopause Definitions

Quantifying STE requires a proper definition of the tropopause. The tropopause represents a physical boundary that separates the upper troposphere from the lower stratosphere [*de Bort*, 1902; *Assman*, 1902]. While there are several definitions for characterizing the tropopause, each is poorly defined in the vicinity of deep convection. In fact, it has been suggested that there is no definition of the tropopause during active deep convection [*Maddox and Mullendore*, 2018]. Therefore, depending on the tropopause definition, transport calculations may vary considerably. *Maddox and Mullendore* [2018] outline several tropopause definitions that are important for STE studies: the temperature lapse rate, potential vorticity, static stability, and chemical tracers.

1.2.1 Thermal Tropopause

The temperature lapse rate definition follows the criteria of *World Meteorological Organization* [1957] in which the tropopause is defined to be the "lowest level at which the lapse rate decreases to 2°C/km or less provided also the average lapse rate between this level and all higher levels with 2 km does not exceed 2°C/km." Multiple tropopauses,

which are often observed around the jet stream, fronts, storms, and stratospheric intrusions [*Shapiro*, 1980], are permitted using this definition under scenarios where the lapse rate is greater than 3°C/km for 1 km above the first tropopause and the tropopause criteria is met again at a higher altitude. Since the LRT is derived from vertical temperature soundings, it also marks the vertical discontinuity in static stability [e.g., *Vömel et al*., 2007; *Logan et al*., 1999; *Birner et al*., 2002; *Pan et al*., 2004]. This definition is attractive because similar thermal structures are observed at all latitudes and it exhibits breaks near the jet streams. This definition is also particularly useful for transport studies because the transition of chemical tracers (e.g., CO, O_3, and H_2O) is typically centered on the thermal tropopause [*Pan et al*., 2004].

1.2.2 Dynamic Tropopause

The potential vorticity (PV), or "dynamical tropopause" definition is commonly used for synoptic-scale events or climatological studies in the extratropics, or studies that desire a material surface that separates stratospheric and tropospheric air masses. This definition requires three-dimensional temperature and wind data and represents changes in both static stability and vorticity, which is representative of the dynamic stability [*Danielsen*, 1964], as opposed to the thermal tropopause, which represents static stability. Therefore, PV is able to represent the discontinuity in static stability at the tropopause as well as gradients in vorticity, such as those found around the flanks of the subtropical jet. The definition of PV by *Rossby* [1940] and *Ertel* [1942] using isentropic coordinates and the hydrostatic approximation is as follows:

$$PV = \frac{\zeta_\theta + f}{\sigma} \tag{1}$$

where ζ_θ is the relative vorticity evaluated on isentropic coordinates, f is the Coriolis parameter, and σ is the isentropic density, defined as:

$$\sigma = \rho\left(\frac{\partial\theta}{\partial z}\right)^{-1} = -\left(g\frac{\partial\theta}{\partial p}\right)^{-1} \tag{2}$$

where ρ is density, θ is potential temperature, z is altitude, g is gravity, and p is pressure. Alternatively, PV can be expressed directly in terms of static stability N^2:

$$PV = N^2 \frac{\theta}{\rho g}(\zeta_\theta + f) \quad (3)$$

PV is conserved for adiabatic and inviscid flow, which makes it a quasi-material surface and thus, an attractive tropopause definition for studies involving large-scale dynamics in the extratropical UTLS [*Hoskins et al*., 1985]. Since a large PV gradient exists in the UTLS, studies typically subjectively choose a potential vorticity threshold to serve as the barrier between the troposphere and stratosphere [*Gettleman et al.,* 2011]. For synoptic-scale studies, a 2 potential vorticity unit (PVU; 1 PVU = 10^{-6} K kg^{-1} m^2 s^{-1}) threshold is typically chosen, however, other values have been chosen to represent the WMO thermal tropopause or chemical transition and can range from 1.5 – 5 PVU, depending on season [e.g., *Hoerling et al*., 1991; *Kunz et al*., 2011]. However, since PV approaches a value of zero near the equator, the dynamic tropopause ceases to represent the troposphere-stratosphere boundary at lower latitudes (typically those equatorward of the subtropical jet), and therefore is not appropriate for transport studies in the tropics.

1.2.3 Static Stability Tropopause

The irreversible transport of mass from one reservoir to another (e.g., from troposphere to the stratosphere) depends on the buoyancy of the air parcels. Air parcels originating in the troposphere and transported to the stratosphere will, unless heated, be negatively buoyant and return to the troposphere. To be irreversibly transported to the stratosphere, those air parcels must be heated by some process, which typically occurs (in the case of convective transport) through latent heating in the updraft or turbulent mixing at cloud top [e.g., *Mullendore et al*., 2005]. Therefore, the discontinuity in static stability, defined by the vertical gradient in potential temperature, can be used to determine the transition between the troposphere and stratosphere. Similar to the temperature LRT, the potential temperature lapse rate also exhibits a distinct change. The troposphere is less stable and as such the potential temperature increases much slower with height compared to the stable stratosphere, in which potential temperature increases rapidly with height. Transport studies typically subjectively determine a potential temperature lapse rate threshold from the pre-convective environment to use as the tropopause. For example, *Mullendore et al.* [2005] used a threshold of 0.00935 K m^{-1} and *Maddox and Mullendore*

used a threshold of 0.012 K m^{-1} to represent the tropopause in their studies of convective transport. Air that has crossed this threshold will likely remain in the other layer long enough to be sufficiently mixed and irreversibly transported.

1.2.4 Chemical Tropopause

As noted in section 1.1.1, the chemical composition of the UTLS is characterized by sharp gradients in several trace gases, allowing for certain trace gases to be identified as troposphere tracers (i.e., being most prevalent in the troposphere) or stratosphere tracers. Common troposphere tracers are CO and H_2O, while O_3 is commonly used as a stratosphere tracer. The strong gradients of these tracers near the tropopause are a result of the sharp change in static stability (as discussed in section 1.2.3), which inhibits vertical motion in the absence of diabatic processes or isentropic wave breaking.

The long history of ozonesonde (balloon-borne) measurements have provided a robust understanding of the vertical profile of O_3 in the lower and middle atmosphere. As such, the vertical O_3 gradient has most often been used to identify a chemical tropopause [*Browell et al*., 1996; *Bethan et al*., 1996]. However, estimates of the tropopause using both O_3 threshold values and its vertical gradient can sometimes differ from the thermal tropopause by 800m [*Bethan et al*., 1996]. More recently, the chemical transition has been identified using tracer-tracer correlations. In this approach, the chemical tropopause is identified as the altitude corresponding to the inflection point in the correlation between a troposphere tracer and stratosphere tracer. *Pan et al*. [2004] showed that this approach to defining the chemical tropopause was statistically centered on the altitude of the thermal tropopause.

1.4 Analysis Methods

1.4.1 Past Observational Studies and Motivation for Modeling

Many recent observational and modeling studies have focused on documenting the effects of extratropical tropopause-penetrating convection on the composition of the UTLS and investigating the mechanisms responsible for exchange. Aircraft observations from individual events have been used to identify how tropopause-penetrating convection

redistributes trace gases in the atmosphere [e.g., *Fischer et al.,* 2003; *Hegglin et al.,* 2004; *Ray et al.,* 2004; *Hanisco et al.,* 2007; *Anderson et al.,* 2012; *Homeyer et al.,* 2014a; *Pan et al.,* 2014]. However, *in situ* observations of the convective overshoot (that extending well above the tropopause) are not possible with current research aircraft.

Observational studies using satellite retrievals have identified the role that deep convection plays in stratosphere-troposphere exchange using different techniques incorporating visible or near-infrared image texture and reflectance [e.g., *Berendes et al*., 2008; *Lindsey and Grasso*, 2008; *Rosenfeld et al*., 2008]. While these algorithms perform well during daytime hours, they suffer from enhanced texture at large solar zenith angles, effectively reducing their ability to detect only daytime storms. This becomes problematic since many tropopause-penetrating storms occur at night and would not be detected by these algorithms [*Bedka et al.,* 2010]. *Homeyer et al.,* [2014] notes that satellite data does not adequately support analysis on the vertical extent of the storm and associated transport into the stratosphere since cloud top heights are inferred by LW IR temperatures and a reference tropopause temperature but do not include thermodynamic modifications of the environment from convection and mixing of the overshooting top in the LS. Additionally, fixed IR temperature-based detection criteria often induces biases in the detection of overshooting tops [*Bedka and Khlopenkov,* 2016]. Other studies have used a technique based on the difference between the 6-7 μm water vapor channel and ~11 μm infrared window channel brightness temperature for overshooting convection [e.g., *Fritz and Laszlo*, 1993; *Ackerman*, 1996; *Schmetz et al*., 1997; *Setvak et al*., 2007; *Martin et al*., 2008], however, this technique requires the stratospheric lapse rate to be inverted and the environmental temperature to increase with height [*Setvak et al*., 2013], which is often violated in reality. Furthermore, since long-lasting overshooting tops are usually composed of many smaller overshooting turrets (< 1 km) that last for very short periods (1-2 min; *Fujita*, 1974), high-resolution sampling and spatial resolution is necessary.

Modeling studies have been employed to provide new insights that could not be found through *in situ* observations [e.g., *Stenchikov et al.,* 1996; *Gray,* 2003; *Wang,* 2003; *Mullendore et al.,* 2005; *Lane et al.,* 2014b; *Bigelbach et al.,* 2014]. Studies involving numerical simulations have shown the importance of gravity wave breaking in

irreversibly transporting tropospheric air into the stratosphere. Gravity wave breaking has been shown to be responsible for direct injection of cloud material from an overshooting top and has been shown to be a necessary condition for the formation of an above anvil cirrus plume [*Wang*, 2003; 2016; *Homeyer et al*., 2017]. Other studies have shown that this mechanism can result in the hydration of the lower stratosphere [e.g., *Hassim and Lane*, 2010]. Idealized modeling studies have shown that the efficiency of transport and overall mass transport varies by storm organization [e.g., *Mullendore et al.,* 2005; *Bigelbach et al.,* 2012]. However, there has not been a modeling study of the bulk impacts of convection on UTLS composition during a multi-week period at a horizontal resolution of less than 4 km.

Since studies of convection-driven STE have only recently become the topic of observational and modeling studies, our current understanding of the impacts of overshooting convection on UTLS composition is limited. While it is currently well known that troposphere-to-stratosphere transport (TST) and stratosphere-to-troposphere transport (STT) are both possible, it is not entirely known how often STE occurs via deep convection, the depth and magnitude of chemical impact, the mechanisms responsible for irreversible transport, and the response of overshooting convection to a changing climate. Since satellite and aircraft observations can be limited in space and time and in situ chemical observations are rare, numerical model simulations are needed to better understand the effects of extratropical convection

1.4.2 Tropopause-Relative Analyses

The goal of most transport studies is to evaluate the amount of mass transported across the tropopause or changes in mixing ratios of key tracers above and below the tropopause. It is often advantageous to examine profiles of key trace gases with the tropopause-relative altitude as the vertical coordinate. This framework provides an advantage over using either potential temperature or altitude as the vertical coordinate in that these coordinates require knowledge of the tropopause altitude to assess changes in UTLS composition.

1.4.3 Tracer-Tracer Correlations

To examine the chemical impact of tropopause-penetrating convection on the UTLS layer, tracer-tracer diagrams were analyzed to identify unique mixing signatures. Tracer-tracer diagrams have been used in many studies to identify irreversible mixing between the UT and LS [e.g., *Hintsa et al.,* 1998; *Fischer et al.,* 2000; *Hoor et al*., 2002; *Pan et al.*, 2004, 2007; *Tilmes et al.,* 2010*; Homeyer et al.,* 2011; *Konopka and Pan,* 2012; *Homeyer et al.,* 2014]. The tracer-tracer diagram is a scatterplot (or correlation) between a tropospheric tracer (H_2O or CO) and a stratospheric tracer (O_3). The scatterplot of a troposphere and stratosphere tracer results in an "L"-shaped correlation for air masses with no mixing between the stratosphere and troposphere (Figure 1). The vertical branch is the stratospheric branch, in which the stratospheric tracer is highly variable while the tropospheric tracer remains fairly constant. The horizontal branch is the tropospheric branch, in which the tropospheric tracer is highly variable while the stratospheric tracer remains constant. The space in between the two branches is the transition layer, which is influenced by the amount of mixing between the stratospheric and tropospheric tracers.

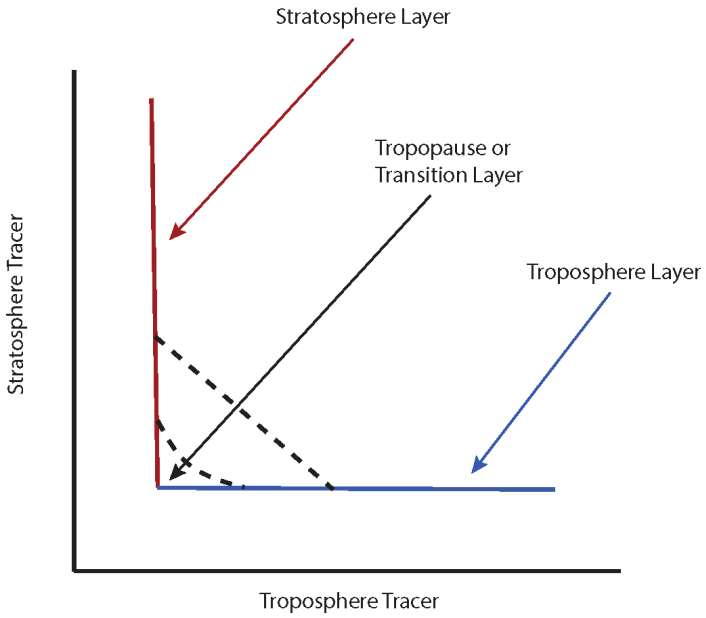

Figure 1. Schematic demonstrating the identification of the troposphere, stratosphere and transition layer branches in tracer-tracer space. Adapted from Figure 6 in *Pan et al*., [2004].

Chapter 2

Sensitivity of Tropopause-Penetrating Convection to Physical Parameterization in WRF-Chem

To better understand the mechanisms responsible for transport and mixing and the significance of convection-driven transport to UTLS composition, new numerical simulations of extratropical tropopause-penetrating convection are needed. However, since the evolution, vertical extent, and intensity of convection are sensitive to the model design, it is important to determine the choices that best reproduce the physical and chemical transport characteristics of observed storms. Model sensitivity tests for the choice of horizontal and vertical grid resolution have recently been completed, and show that the depth of overshooting and cross-tropopause transport increase with finer horizontal grid spacing, but decrease with finer vertical grid spacing [*Homeyer*, 2015].

2.1 Model Design, Data, and Methods

2.1.1 Model Description and Initialization

Version 3.7.1 of the Weather Research and Forecasting model [*Skamarock et al.,* 2008] coupled with Chemistry [*Grell et al.,* 2005; *Fast el al.,* 2006] is used in this study. Simulations are run with one-way nesting from a parent domain with a horizontal grid spacing of 10 km to a nested domain with 2 km grid spacing. The vertical grid consists of 101 levels with a nominal grid spacing of ~ 250 m in the free troposphere and a model top of 30 hPa (~24 km). A 5-km damping layer is employed to prevent reflection of spurious waves off the model top. Strong overshooting convection is capable of reaching altitudes of 17-18 km. Therefore, the model top must be high enough that these storms do not reach the damping layer, which begins ~19 km with this model setup. Meteorological initial and boundary conditions are provided every 6 hours from the ERA-Interim reanalysis, which are available with a horizontal resolution of ~80 km and a vertical resolution ranging from 650 – 1000 m in the extratropical UTLS [*Dee et al.,* 2011].

Chemical initial and boundary conditions are defined using output from the Model of Ozone and Related chemical Tracers, version 4 (MOZART-4; *Emmons et al.,* [2010]) chemical transport model.

Three bulk microphysics parameterizations (BMP), planetary boundary layer (PBL) parameterizations, and chemical mechanisms are tested in this study. The full list of simulations conducted is provided in Table 1. The chosen microphysics parameterizations are the Morrison 2-moment (MOR; *Morrison et al.,* [2005]), the Milbrandt and Yau 2-moment (MY; *Milbrandt and Yau,* [2005]), and the NSSL 2-moment (NSSL; *Mansell et al.,* [2010]) schemes. The chosen PBL parameterizations are the Yonsei University (YSU; *Hong et al.,* [2006]), the quasi-normal scale elimination (QNSE; *Sukoriansky et al.,* [2005]), and the asymmetric convective model, version 2 (ACM2; *Pleim,* [2007a]) schemes. The chosen chemical mechanisms are the Regional Atmospheric Chemistry Model (RACM-ESRL; *Stockwell et al.,* [1997]; *Ahmadov et al.,* [2012]) coupled with the Modal Aerosol Dynamics Model for Europe/Secondary Organic Aerosol Model (MADE/SORGAM; *Ackermann et al.*, [1998]; *Schell et al.,* [2001]), the Carbon Bond Mechanism, version Z, (CBMZ; *Zaveri and Peters,* [1999]) coupled with Model of Simulating Aerosol Interactions and Chemistry 4-bin aerosol model (MOSAIC; *Zaveri et al.,* [2008]), and the Model of Ozone and Related chemical Tracers chemical mechanism (MOZART; *Emmons et al.,* [2010]) coupled with the Georgia Institute of Technology–Goddard Global Ozone Chemistry Aerosol Radiation and Transport aerosol model (GOCART; *Chin et al.,* [2000a]; *Ginoux et al.,* [2001]). While testing the model sensitivity to each type of parameterization, the remaining two were held constant (Table 1), resulting in 7 independent simulations of each targeted convective event (described in more detail below). In particular, the schemes held fixed in each sensitivity test are the NSSL microphysics parameterization, YSU PBL parameterization, and RACM-ESRL chemical mechanism (control run).

Additional model design choices held constant in all simulations are as follows: Smagorinsky first-order closure was used for horizontal subgrid-scale mixing. The RRTMG scheme was used for both short-wave and long-wave radiation [*Iacono et al.,* 2008]. Anthropogenic emissions were generated using the 2011 National Emissions Inventory (NEI 2011). Biogenic emissions were calculated online with the Model of

Emissions of Gases and Aerosols from Nature (MEGAN V2.04; *Guenther et al.,* [2006]). Photolysis rates were calculated using the Fast-J scheme [*Wild et al.,* 2000; *Fast et al.,* 2006].

The reflectivity calculation for the simulations was done using the Center for Analysis and Prediction of Storms (CAPS) Polarimetric Radar data Simulator (CAPS-PRS; e.g., *Jung et al.,* [2008]; *Dawson et al.,* [2014]). The CAPS-PRS is capable of computing polarimetric radar variables from high-resolution numerical simulations using microphysics schemes with one, two, and three moments. Polarimetric variables are expressed as a function of hydrometeor mixing ratio as well as their drop size distribution and densities. The melting layer is accounted for using a continuous melting process for the entire spectrum of varying density and dielectric constants [*Jung et al.,* 2010]. However, the simulator may over-predict simulated reflectivity in the stratiform rain region due to the assumption of a fixed drop size distribution (DSD) intercept parameter for hail and ice particles due to the neglection of non-Rayleigh scattering effects [*Jung et al.,* 2008]. Reflectivity calculations were done using a T-matrix method, which differentiates between Rayleigh and Mie scattering where appropriate and is more accurate than the online WRF radar reflectivity calculation, which only uses Rayleigh scattering.

2.1.2 Descriptions of the Model Parameterizations

Tables 2-4 list some distinguishing features of each parameterization tested in this study. Justification for choosing each scheme is briefly elaborated upon here.

2.1.2.1 Bulk Microphysics

Storms that penetrate the tropopause are often very intense convective events that produce large hail, strong winds, and sometimes tornadoes at the Earth's surface. These storms also have unique physical features, such as strong updrafts, overshooting tops, and sometimes above-anvil cirrus plumes, which are important for STE of water vapor. Since the physical characteristics of these storms depend on microphysical processes, model representations can vary considerably with the choice of BMP. In addition, since each

BMP assumes certain hydrometeor types and sedimentation rates, we expect the choice of BMP to impact the simulated hydration of the UTLS. Based on these anticipated sensitivities, three BMPs of 2nd order or higher were selected (Table 2) instead of single-moment schemes, since double-moment schemes are generally more successful at reproducing observed convective storms [*Igel et al.,* 2015].

The MOR, MY, and NSSL 2-moment schemes were chosen. These schemes differ in the number of predicted hydrometeor classes, assumptions about the gamma function in the size distribution, and the ability to interact with chemistry modules. MY and NSSL each predict the number concentration and mass mixing ratio for 6 hydrometeor classes: cloud droplets, rain, snow, cloud ice, graupel, and hail. MOR only predicts 5 hydrometeor classes: cloud droplets, rain, snow, cloud ice, and graupel or hail. In this study, hail is predicted for MOR. In the gamma function, MY allows the shape parameter to vary as a function of mean-mass diameter which results in more reliable size sorting and sedimentation rates, while the other two BMPs do not. NSSL, however, predicts the density of hail and graupel and assigns a shape parameter based on the predicted densities. Lastly, MOR and NSSL allow aerosols predicted by WRF-Chem to affect droplets number concentrations and subsequent cloud physics. However, while prognostic aerosol effects were turned on, other aerosol effects (aerosol-radiation) were turned off such that the sensitivity to each parameterization could be individually evaluated without complexities arising from different interactions between the meteorology and chemistry schemes.

2.1.2.2 Planetary Boundary Layer

The PBL scheme in a numerical model such as WRF-Chem determines the subgrid-scale turbulence and vertical mixing, as well as the vertical thermodynamic and kinematic profiles of the lowest model levels. Thus, the choice of PBL scheme will impact the simulated PBL height, the location and timing of convection initiation, and the source of the air ingested by the storm and transported to the UTLS. Current PBL schemes available in WRF-Chem can be classified into three different groups based on their treatment of subgrid-scale mixing: local, non-local, and hybrid (i.e., both local and non-local). The basic difference between local and non-local mixing involves the depth over

which vertical levels influence a variable at a given point. That is, in a local mixing scheme, a variable is only influenced by variables at directly adjacent vertical levels. In a non-local mixing scheme, a variable may be influenced by a number of vertical levels. For a hybrid scheme, the stability of the boundary layer determines whether local or non-local mixing is used (i.e., for neutral or stable conditions, it uses local closure and turns off non-local transport). To evaluate PBL schemes here, we chose one scheme from each category (Table 3): QNSE (local), YSU (non-local), and ACM2 (hybrid).

2.1.2.3 Chemical Mechanism

In WRF-Chem, numerous options are available for the chemical mechanism. Among the 30 different options are seven gas-phase chemical mechanisms with different couplings to aerosol schemes, optional incorporation of aqueous chemistry, adaptions to use the Kinetic Pre-Processor library (KPP) and the Rosenbrock solver [*Sandu et al.,* 2006], or other deviations from the default procedure of each mechanism. Since the chemical effects of convection-driven STE can be represented differently depending on the chemical mechanism used, three commonly used gas-phase mechanisms were chosen (Table 4), each coupled to aerosol modules of varying complexity.

The representation of aerosol chemistry varies from a simple representation in MOZCART to more complex approaches in CBMZ-MOSAIC and RACM-ESRL with MADE/SORGAM. In particular, RACM-ESRL is coupled to the MADE/SORGAM/VBS aerosol module that represents secondary organic aerosol formation (SOA) and thus is designed to give more representative concentrations of particulate matter at diameters 2.5 microns and less ($PM_{2.5}$) than the other two chemical mechanisms presented here. SOA formation in CBMZ-MOSAIC follows a simplified approach [e.g., *Zaveri et al.,* 2008; *Hodzic and Jimenez*, 2011] and MOZCART does not include SOA formation. The SOA formation used in CBMZ-MOSAIC follows an empirical parameterization based on the ratio between observed SOA concentrations to excess CO and the photochemical age of the airmass. In this formulation, organic mass is emitted as lumped SOA precursor surrogate in proportion to anthropogenic or biomass burned CO emissions following the observed SOA and CO ratio in aged air. This surrogate then reacts with OH to form a single non-volatile species that condenses to form SOA [*Hodzic and Jimenez*, 2011]. The

SOA parameterization in RACM-ESRL follows the method described in *Ahmadov et al.* [2012]. Briefly, the parameterization is based on a four bin volatility basis set. VOCs are oxidized by the hydroxyl radical, O_3, and nitrate radical into anthropogenic and biogenic compounds. Organic mass in each bin is produced for both high and low NO_X regimes, and partitioned into aerosol and gas phase. Couplings to less complex aerosol modules (i.e., fewer bins or modes) were chosen over more detailed treatments since the main goal of this study is to assess the model sensitivity for bulk transport of trace gases and water. The wet scavenging scheme employed in RACM-ESRL and CBMZ follows the *Easter et al.* [2004] approach while in MOZCART follows the *Neu and Prather* [2012] approach for gases and *Easter et al.* [2004] for aerosols. Both methods treat wet deposition by grid-resolved precipitation, scavenging of cloud-phase aerosols and gases by collection and freezing, interstitial-phase aerosols by impaction, and gas-phase gases by mass transfer and reaction. The main difference between the two approaches is the treatment of nitric acid (HNO_3). In the *Neu and Prather* [2012] approach, HNO_3 is partitioned into cloud ice as a function of temperature based on a burial model. As noted in section 2.2.1, prognostic aerosols were turned on for these simulations. However, aerosol-cloud interactions only worked with the RACM-ESRL and CBMZ scheme, and not MOZCART. Additionally, aerosol effects on the radiation scheme were turned off.

2.1.3 Observations for Model Evaluation

To conduct a robust evaluation of the selected model parameterizations, three observed cases from the Deep Convective Clouds and Chemistry (DC3) field campaign [*Barth et al.,* 2015] were simulated: 19-20 May 2012, 29-30 May 2012, and 1-2 June 2012. Figure 2 shows the DC3 flight paths for each case and the boundary of the WRF nested domain used for analysis. For brevity, we only discuss results from the 19-20 May case in this paper, but the results for the remaining cases are comparable (Figures 15-31).

Trace gas measurements from two DC3 aircraft are used to evaluate the model simulated trace gas distributions in the troposphere and lower stratosphere: the National Science Foundation-National Center for Atmospheric Research (NSF-NCAR) Gulfstream V (GV) and the National Aeronautics and Space Administration (NASA) DC-8. Measurements of O_3, CO, and H_2O from each aircraft were obtained at a rate of 1 Hz,

which corresponds to a horizontal resolution of 100-200 m at aircraft cruise speed. Measurements of CH_2O, SO_2, and HNO_3 were obtained at a resolution of 1-2 s, 2-10 s, and 1-2 s, respectively. Cloud measurements from the NASA DC-8 were incomplete during DC3 especially before 29 May when the cloud particle imager was added to the aircraft, such that a cloud indicator based on forward-facing video camera and cloud particle imaging (when available) was created to facilitate analysis of cloudy and clear-sky conditions during the entire campaign. Additional detail on this manually developed cloud indicator is available in *Pollack et al.* [2016]. On the NSF-NCAR GV, cloud particles were measured throughout the field campaign using the 2D-C probe [*National Center for Atmospheric Research,* 2013]. More information about the instruments on board the GV and DC-8 used in this study is given in Table 5.

The structure, intensity, and evolution of the simulated storms are evaluated in this study using three-dimensional composites of individual radar volumes from the Next Generation Weather Radar (NEXRAD) program Weather Surveillance Radar—1988 Doppler (WSR-88D) network [*Crum and Alberty,* 1993]. When operating in convective mode, data from individual radars are available every 4-7 minutes on native spherical grids with 14 elevation scans. These individual radar volumes were obtained from the National Centers from Environmental Information (NCEI) and merged into large-area multi-radar composites following the methods outlined in *Homeyer* [2014] and updated in *Homeyer and Kumjian* [2015]. The composites have a temporal resolution of 5 minutes, a horizontal resolution of 0.02° longitude-latitude (~2 km), and a vertical resolution of 1 km.

2.1.4 Background and Analysis of 19 May DC3 storm

On 19 May 2012 a deep convective line in central Oklahoma and Kansas initiated along a surface cold front. The storm was sampled by the NSF-NCAR GV and NASA DC-8 between 21:00 UTC on 19 May and 02:15 UTC on 20 May. A double tropopause was present at the time as a result of a poleward breaking Rossby wave, which transported air from the tropical upper troposphere to the extratropical lower stratosphere [e.g., *Pan et al.,* 2009; *Homeyer et al.,* 2011b]. It has also been hypothesized that the double tropopause environment facilitated the large depth of overshooting, with storm top

altitudes reaching up to 4 km above the unperturbed primary tropopause [*Homeyer et al.,* 2014].

The analysis period was 22:30 UTC – 03:00 UTC for the model simulations and 21:00 UTC – 02:15 UTC for the observed storm, corresponding to comparable stages in the evolutions of the observed and modeled storms. The analysis area was a subset of the nested domain shown in Figure 2, which was subjectively determined in the model simulations to correspond to the convective system sampled by the DC3 aircraft. All figures shown were generated using this analysis area and time frame, unless otherwise noted.

2.2 Results

2.2.1 Structure and Organization of the Simulated 19-20 May Storm

Figure 3 shows simulated column-maximum radar reflectivity for each independent model run and the observed storm at comparable times. Based on the radar reflectivity fields, it is apparent that the simulated storm is most sensitive to the choice of BMP and least sensitive to the choice of chemical mechanism. While the choice of BMP has little impact on the timing and location of the simulated storm (Figure 4), there are some clear differences in the horizontal scale and mode of convective organization. In particular, the NSSL BMP gives a more horizontally narrow storm than MOR or MY, which best agrees with the observed storm (Fig. 3). This is likely due to the NSSL scheme's design, which allows the density of hail and graupel to vary and arguably leads to more reliable differential size sorting and sedimentation rates as described in *Dawson et al.,* [2014]. The authors of this study performed, idealized simulations of an observed supercell storm with the NSSL 2-moment bulk microphysics scheme were done while allowing and disallowing size sorting for hydrometeor species, considering several velocity-diameter relationships for hail fall speed, and compared fixed and variable bulk densities that span the graupel-to-hail spectrum. The best performing simulations were the ones in which size sorting was allowed for rain and hail, and the bulk density and fall-speed curve for

hail were predicted. Thus, the differential size sorting of the NSSL BMP is likely the reason for the better representation of the simulated storm.

In contrast to the BMPs, the physical characteristics of the simulated storm are less sensitive to the three selected PBL schemes. The main difference, however, is the timing (Figure 4), with simulations using the YSU and QNSE PBL schemes initiating the convective line about 30 minutes - 1 hour earlier than the simulation using ACM2. The hybrid non-local and local mixing in ACM2 produced a PBL height higher than in YSU and QNSE, which was likely responsible for the later convective initiation. YSU and QNSE PBL schemes initiated convection 1.5 hours later than the observed storm, with ACM2 initiating convection about 2.5 hours later than observed.

For the chemical mechanisms there are a few differences between the three realizations, due to the inclusion of cloud-aerosol interactions. Other chemistry interactions (e.g., aerosol-radiation, cloud chemistry) were turned off. With those options included, there would be increased potential for measurable differences (Figure 5). In Figure 3, the only distinguishing feature among the three chemical mechanism sensitivity simulations is the shape of the discrete cell to the north of the convective line which is likely due to aerosol-cloud interactions.

2.2.2 Vertical Extent of Simulated Storms

To assess the sensitivity of storm top altitudes to model parameterization, simulated cloud top and 10 dBZ radar reflectivity echo top box plots are compared to the observed NEXRAD composite 10 dBZ echo tops (Figure 6). Cloud tops are determined in WRF simulations as the highest altitude in a column where the cloud-mixing ratio was at least 0.1 g/kg. Note that the vertical sampling from NEXRAD (1 km) is coarser than the vertical resolution in WRF (250 m). Box plots of WRF output were generated with a coarser resolution to match the NEXRAD resolution and showed no significant difference (not shown). Therefore, it should be noted that WRF results are good to within 1 km of the NEXRAD data.

Overall, the simulated echo tops are underestimated for all BMPs, though the median echo top in MY is slightly closer to that observed. Similar to the BMPs, model-simulated echo tops are low for all PBL schemes. The echo top distribution with the

ACM2 PBL scheme is closer to the observed echo top distribution than the other PBL schemes. Among the chemical mechanisms, there is essentially no difference between them.

Simulated cloud top altitudes are all higher than the observed echo top, which is expected since NEXRAD WSR-88D radars detect only precipitation-sized particles. This result is in agreement with previous studies [e.g., *Homeyer et al.,* 2014; *Homeyer,* 2015] of simulated tropopause-penetrating convection, which show that model simulated echo tops are typically lower than observed, while cloud top altitudes are higher. In contrast to the model simulated echo tops, which showed little variability in the upper bounds (75% and maximum) of the echo top distribution, there are notable differences between the BMPs. NSSL has the highest cloud top altitudes, with maxima more than 1 km above those in MOR.

2.2.3 Chemical Distributions of Simulated Storms

To evaluate the model simulated chemical distribution, simulated vertical profiles of several trace gases superimposed on the DC3 aircraft observations are presented. Vertical profiles were created for the minimum, median, and maximum mixing ratios over a sub-section of the nested domain. The selected area is comparable to the area observed by the aircraft and at comparable times in the storm's evolution (between the observed and simulated storm). In order to analyze only background and anvil-cloud points, profiles of trace gases were first filtered to remove any convective influence by removing columns where the surface precipitation accumulation is greater than 0 mm and updraft speed is greater than 5 ms^{-1}. Next, profiles were stratified into in-cloud and out-of-cloud populations, where in-cloud are simply those where cloud particles exist in both simulations and observations. The threshold for cloud particles is the same as described in the above section (e.g., cloud indicator for DC8, 2D-C measurements with threshold of 0.1 g kg^{-1} for GV, and qtot with threshold of 0.1 g kg^{-1} for WRF simulations).

For H_2O, the median profiles are in general agreement among the microphysics schemes (Figure 7), but the maximum mixing ratios differ, especially above the tropopause. Since H_2O injection is an important aspect of STE from extratropical

convection due to its chemical and radiative impacts, accurately simulating this process is a key criterion for the evaluation of these simulations. In both in-cloud and out-of-cloud profiles, the MOR and MY schemes simulates maximum mixing ratios less than 200 ppmv, while the NSSL scheme simulates a maximum mixing ratio as high as 300 ppmv. In comparison, the maximum H_2O mixing ratio observed in the stratosphere by DC3 aircraft was 250 ± 12 ppmv. Thus, it can be concluded that the MOR and MY schemes underrepresent H_2O injection while the NSSL scheme simulates mixing ratios that were slightly higher than observed.

As noted earlier, the NSSL scheme's design allows for more complex differential size sorting and sedimentation rates compared to the other two BMPs. In particular, simulations with the NSSL BMP had a higher mass mixing ratio of cloud ice in the thunderstorm anvil above the tropopause (Figure 8), which likely produced more rapid sublimation and enhancement of water vapor in the stratosphere. Larger frozen hydrometeors (i.e., snow, graupel, and hail) could potentially hydrate the stratosphere, but such hydrometeors are typically located in the interior of the cloud where they require strong upward motion to remain suspended. Ice particles are located near the exterior of the cloud and are directly exposed to the dry stratospheric air, thereby permitting rapid sublimation. MY had the lowest ice mass mixing ratio, but the most snow. MOR BMP has the highest mass mixing ratio of graupel/hail compared to the other two BMPs. These differences in hydrometeor class partitioning are likely responsible for the identified differences in H_2O enhancements in the stratosphere (Figure 7).

For the O_3 and CO out-of-cloud profiles (Fig. 7), differences are found between the simulations in the extremes, especially in the depth of mixing above and below the tropopause. The MOR and MY schemes exhibit a similar depth of mixing (3-4 km), while the NSSL scheme shows a shallower layer (1-2 km). It is currently hypothesized that this difference in mixing layer depth is due to the depth of their respective anvil clouds, which extend above the tropopause level. Cross sections, arbitrarily taken, demonstrate the differences in the depths of the simulated storm anvils (Figure 9). MOR and MY have similar anvil depths, while NSSL has a shallower anvil. A photograph of the observed storm taken from aircraft show that the anvil was shallower and best reproduced by the NSSL scheme. Furthermore, the observations, though somewhat

limited, seem to suggest a shallower layer of mixing (~2 km), in agreement with the NSSL scheme.

These simulations also demonstrate the impact of different transport processes (e.g., air mass mixing versus convective injection of ice) as shown in the differences in the peak altitude of the CO/O_3 and H_2O perturbations. Although the aircraft only sampled air ~1 km above the tropopause, WRF-Chem simulations suggest that H_2O enhancements extended up to 5 km above the tropopause. Transport of constituents into the stratosphere is deeper for H_2O compared to CO and O_3 in part because the cloud and tracer boundaries are often not coincident in WRF-Chem. More importantly, H_2O enhancements in the stratosphere are sourced by two processes: 1) air mass transport from the troposphere (the only process relevant for O_3 and CO) and 2) rapid sublimation of convectively lofted ice, which can be lofted to higher altitudes than that achieved by convective ascent when gravity wave breaking occurs. In addition, since air is often near saturation and cooling as it ascends, H_2O enhancement from air mass transport is limited to the saturation vapor pressure, which typically reaches 5-10 ppmv at the tropopause. Thus, most of the stratospheric water vapor enhancement is due to the detrainment and sublimation of cloud ice rather than air mass transport. This suggests that changes in CO and O_3 in the UTLS are largely controlled by a different process (i.e., air mass transport) than those affecting H_2O, which enables their influence on UTLS composition to vary considerably.

For other trace gases that are important for O_3 and heterogeneous chemistry in the UTLS (e.g., soluble species such as HNO_3, SO_2, CH_2O), there is more variability among the BMPs (Figure 10). For HNO_3, all three BMPs underestimate the observed maximum HNO_3 mixing ratio in the UTLS by about 1000 pptv for both in-cloud and out-of-cloud profiles, suggesting that the model is over-scavenging HNO_3, a result consistent with *Bela et al.* [2016]. Additionally, since HNO_3 has a relatively long atmospheric lifetime, it is possible that some is transported to the UT from the LS, which may not have been represented adequately in the model (see Chapter 3). However, the HNO_3 observations measured with a 0.1 ppb precision and 50% bias. A difference of 1000 pptv between the model and observations would be within the instrument's range of uncertainty. MOR and MY have higher HNO_3 mixing ratios below the tropopause compared to NSSL (and observations), possibly due to the higher precipitation mixing ratios in MOR and MY.

The wet scavenging schemes deplete trace gas mixing ratios based on production of precipitation and therefore more HNO_3 should be depleted at low levels to around 2 km below the tropopause. However, due to the complexities of the cloud physics, it is difficult to say why HNO_3 mixing ratios are higher in MOR and MY. Explaining these differences should be a part of future studies.

For SO_2, NSSL underestimates mixing ratios in the UTLS out-of-cloud while MOR and MY do a good job reproducing the SO_2 out-of cloud profile. However, MOR greatly overestimates SO_2 mixing ratios within cloud. For CH_2O, all three BMPs are in good agreement with observations within cloud. For out-of-cloud profiles, MOR and MY overestimate CH_2O while NSSL underestimates CH_2O in the UTLS. Comparison of soluble trace gas profiles within a region not affected by the storm (not shown) reveals very few differences between the BMPs, suggesting that most of the differences (i.e., sensitivity) outlined here are due to differences in the wet scavenging method employed in each chemical mechanism (see Table 4). A deeper investigation into the differences between the parameterizations used is beyond the scope of this study.

Figure 11 shows the chemical profiles of O_3, H_2O and CO for the three PBL schemes. There is little impact of PBL scheme choice on the vertical distribution of these trace gases. There are some small differences for CO and other trace gases (e.g., SO_2, CH_2O (Figure 12)), but in comparison with the aircraft observations, there is no objectively superior PBL scheme.

Vertical profiles of trace gases exhibit some sensitivity to the choice of chemical mechanism. Overall, there is little sensitivity for O_3, H_2O, and CO (Figure 13), however, for other trace gases (Figure 14), MOZCART and CBMZ remain consistent, while RACM-ESRL is measurably different. In general, MOZCART and CBMZ best reproduce the chemical profiles of HNO_3 and CH_2O while greatly overestimating the maximum SO_2 concentrations in the UTLS. RACM-ESRL tends to underestimate concentrations of HNO_3 and SO_2 throughout the model domain. In RACM-ESRL, the lower SO_2 concentrations are due to a SO_2 conversion to SO_4 from cloud chemistry that is not done in MOZCART or CBMZ. The differences in HNO_3, however, are not clear at this time, but potentially due to differences in wet scavenging. An in depth look into these differences is the subject of future work.

2.3 Discussion

Overall, it was found that WRF-Chem simulations of the physical characteristics and STE of tropopause-penetrating convection are most sensitive to the choice of bulk microphysics parameterization. This is not surprising since microphysics play a large role in the structure, organization, and intensity of storms and their ability to hydrate or otherwise modify the composition of the UTLS. Based on the available aircraft observations from the case presented as well as the other two DC3 cases simulated (Figures 15-31), the NSSL 2-moment BMP best represented the physical and chemical characteristics of the simulated storms. This conclusion was based largely on the scheme's representation of stratospheric water vapor enhancements (from air mass transport and ice injection), which is one of the most important processes that simulations of tropopause-penetrating convection seek to reproduce. Though not shown, the cloud boundary and O_3/CO boundaries in overshooting convection are often not coincident in WRF-Chem, which leads to some of the differences in the depth of change in their stratospheric concentrations compared to that for H_2O. Further work should determine whether or not this offset between the cloud and tracer boundaries is representative of reality.

The choice of PBL parameterization shows less sensitivity than the BMP, but does show some differences in convection initiation and chemical composition due to differences in mixing and the height of the PBL—which may impact the chemical composition of the air ingested by the convection near cloud base. Among the three PBL schemes, while the physical characteristics were fairly similar, the timing of convective initiation with ACM2 occurred nearly one hour later than the other two simulations and 2.5 hours later than that observed. For the chemical distributions, there were more noticeable, albeit small, differences for the in-cloud profiles than out-of-cloud profiles, though all PBL schemes were very similar. The differences were likely due to differing representations of vertical mixing, which can lead to differences in PBL height and, consequently, air source. Vertical mixing in QNSE is achieved by a local mixing scheme, which gives a lower PBL height, consistent with previous studies comparing local and non-local schemes [e.g., *Cohen et al.,* 2015; *Coniglio et al.,* 2013]. This could have

resulted in a source of air that was more polluted (e.g., higher CO) than the other two schemes (not shown).

While the simulations presented in this study show that the choice in chemical mechanism offers little sensitivity, it should be reiterated that the goals of this study were to assess the sensitivity to bulk transport of mainly passive tracers (e.g., O_3 and CO) and H_2O. Thus, for alternative research questions (e.g., wet scavenging, cloud chemistry, etc.) it should be noted that the sensitivity may be larger to the choice of chemical mechanism. Other complexities of the chemical mechanisms, such as gas-aerosol schemes would arguably be better suited for studies in which an accurate representation of aerosols is needed. For example, RACM-ESRL is coupled to the MADE/VBS aerosol module that was designed to give more representative SOA and $PM_{2.5}$ concentrations than the other two chemical mechanisms presented here. However, in line with the goals of this study, aerosol-radiation effects and cloud-chemistry were turned off. With those interactions enabled, the physical and chemical characteristics would likely have differed, suggesting that the inclusion of these effects offers more sensitivity to STE from extratropical convection than the chosen gas-phase chemical mechanism (Figure 5). As noted, prognostic aerosols were turned on, though only the RACM-ESRL and CBMZ chemical mechanism allowed aerosol-cloud interactions. Turning prognostic aerosols off resulted in higher water vapor perturbations in the stratosphere and a shallower layer of mixing of CO/O_3 out of cloud, and a slightly deeper layer of mixing in-cloud (Figure 31). For soluble trace gases, there was little difference outside the area of convective influence. Within cloud, the inclusion of aerosol-cloud interactions resulted in an increase in SO_2 in the UTLS, however, for HNO_3 and HCHO, there were increases in the concentrations of those gases, but the magnitude may vary by chemical mechanism (Figure 32)

2.4 Conclusions

Of the three different model parameterization types tested in this study, WRF-Chem simulations of tropopause-penetrating convection and STE are most sensitive to the choice in BMP. As expected, there is measurable sensitivity of the organization and vertical extent of simulated convection to the choice of BMP. Furthermore, the simulations in this study show that convectively injected water into the stratosphere is

also sensitive to the choice of BMP. Among the three BMPs tested, the NSSL 2-moment scheme provided the best representation of both the observed physical characteristics of the storm and the composition of the UTLS.

There was little sensitivity of the physical characteristics of the storms to the chosen chemical mechanism. For assessing bulk transport of mostly passive trace gases, there were little apparent differences. Thus, the choice in chemical mechanism should be based on the specific research questions the user wants to investigate. For the PBL schemes tested, there was little sensitivity in both the physical structure of the simulated storm and composition of the UTLS, though there were small differences in the timing of convective initiation.

Since the simulations in this study were only performed for 24 hours, the evaluation of long-term convective transport and the resulting chemistry could not be assessed. *Barth et al.,* [2012] noted that most convection-induced O_3 production occurs within the first 24 hours. Ending the simulation at 1200 UTC may not have allowed adequate time for such chemistry to take place in the model. Furthermore, simulated trace gas profiles were calculated and evaluated during active convection while the tropopause is actively perturbed. While the observations were also obtained during active convection, it would be useful to evaluate the model performance of long-term transport. Simulations could have been extended for 12-24 hours following convection and compared with observations obtained over that same time horizon. These additions could have resulted in a better evaluation of the chemical mechanisms. Despite these caveats, the differences in simulated LS hydration are noteworthy and should aid in decisions regarding model design for future studies involving the effects of convection on LS H_2O.

Table 1. Description of simulations performed.

Test group	**BMP**	**PBL**	**CHEM**
Control run	NSSL	YSU	RACM-ESRL
BMP-1	MOR	YSU	RACM-ESRL
BMP-2	MY	YSU	RACM-ESRL
PBL-1	NSSL	QNSE	RACM-ESRL
PBL-2	NSSL	ACM2	RACM-ESRL
CHEM-1	NSSL	YSU	MOZCART
CHEM-2	NSSL	YSU	CBMZ

Table 2. Predicted hydrometeor moments and other unique details of the bulk microphysics parameterizations (BMPs) employed in this study.

	MOR	NSSL	MY
Predicted mass mixing ratios	Q_c, Q_r, Q_s, Q_i, $Q_{g/h}$	Q_c, Q_r, Q_s, Q_i, Q_g, Q_h	Q_c, Q_r, Q_s, Q_i, Q_g, Q_h
Predicted number concentrations	N_c, N_r, N_s, N_i, $N_{g/h}$	N_c, N_r, N_s, N_i, N_g, N_h	N_c, N_r, N_s, N_i, N_g, N_h
Other	Prognostic aerosols turned on; Hail option turned on	Prognostic aerosols turned on; Predicts graupel and hail density; assigns shape parameter based on graupel/hail density	Allows shape parameter to vary in particle size distribution
Reference	*Morrison et al.* [2005]	*Milbrandt and Yau* [2005]	*Mansell et al.* [2010]

Table 3. Characteristics of the planetary boundary layer (PBL) parameterizations employed in this study. Adapted from Cohen et al. (2015).

	YSU	QNSE	ACM2
Mixing	Non-local (meteorology) Local (chemistry)	Local	Hybrid
Advantages	Simulates deeper vertical mixing in buoyancy-driven PBL	Intended to account for wave phenomena within stable PBL	Potential Temperature and velocity depicted with greater accuracy; Same mixing for chemical species; Default BL model in CMAQ
Disadvantages	Too deep PBL for springtime convection	Too cool, moist, and shallow PBL	Too deep PBL
Reference	*Hong et al.* [2006]	*Sukoriansky et al.* [2005]	*Pleim* [2007a]

Table 4. Characteristics of the chemical mechanisms employed in this study.

	RACM-ESRL	CBMZ	MOZART
Aerosol Scheme	MADE/SORGAM/VBS (Modal – 3 modes)	MOSAIC (Bin – 4 bins)	GOCART (Bulk)
Aerosol/cloud interactions	Yes	Yes	No
SOA Formation	*Ahmadov et al.* [2012]	*Zaveri et al.* [2008]; *Hodzic and Jimenez* [2011]	None
Wet Scavenging	*Easter et al.* [2004]	*Easter et al.* [2004]	*Neu and Prather* [2012]
No. Reactions	214 (gas-phase)	132	157 (gas-phase)
No. Species	77	52	85

Table 5. Precision and uncertainty of measurements from aircraft-based instruments used in model evaluation.

Instrument	Variable	Precision and Uncertainty	Aircraft	Reference
NCAR	O_3	2 ppbv±5%	GV	*Ridley et al.* [1992]
NCAR vUV	CO	3 ppbv±3%	GV	Similar to *Gerbig et al.* [1999]
VCSEL	H_2O	<2 %±5%	GV	*Zondlo et al.* [2010]
GT-CIMS	SO_2	0.0119 ppb	GV	*Kim et al.* [2007]
GT-CIMS	HNO_3	0.0396 ppb	GV	*Huey* [2017]
CAMS	CH_2O	0.02-0.03 ppb ± 0.02-0.03 ppb	GV	*Fried et al.* [2016]
2D-C	Cloud	N/A	GV	*NCAR* [2013]
NOAA CL	O_3	0.6 ppbv±5%	DC8	*Davis et al.* [2007]; *Dorsi et al.* [2014]
DACOM	CO	2 ppbv±2%	DC8	*Ryerson et al.* [1999]
NASA DLH	H_2O	1 ppmv±5%	DC8	*Diskin et al.* [2002]
GT-CIMS	SO_2	0.002 ppb	DC8	*Kim et al.* [2007]
GT-CIMS	HNO_3	0.1 ppb±50%	DC8	*Huey* [2017]
DFGAS	CH_2O	0.05 ppb± 0.05 ppb	DC8	*Fried et al.* [2016]
Cloud Indicator	Cloud	---	DC8	---

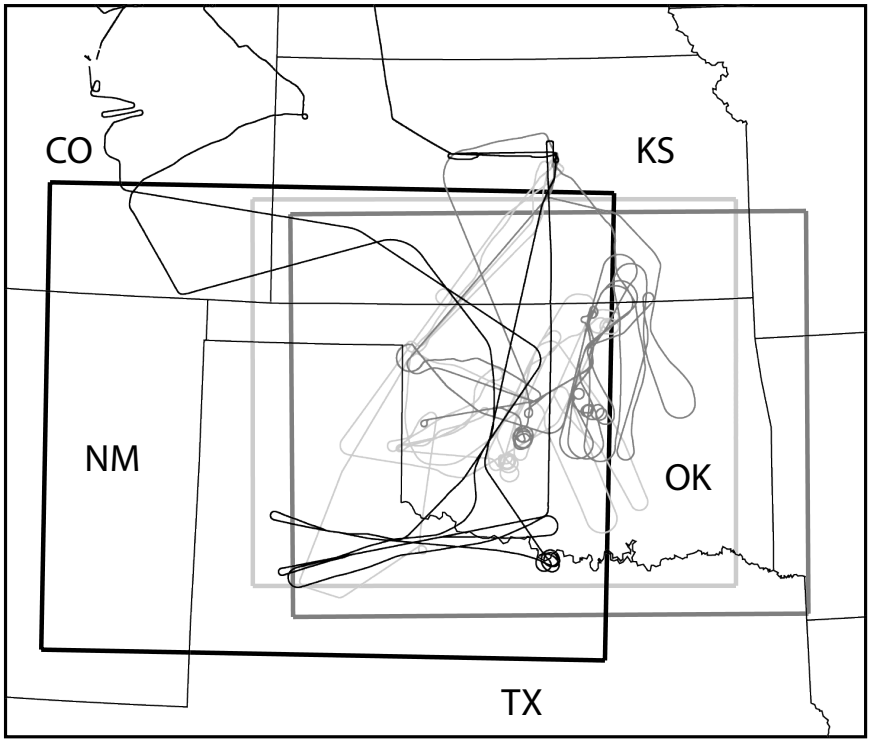

Figure 2. DC3 aircraft flight paths for the 19 May (light gray), 29 May (dark gray), and 1 June (black) research flights, with the boundary of the WRF 2-km grid shown by the thick polygons of equivalent color. Thin black lines in the background show state boundaries.

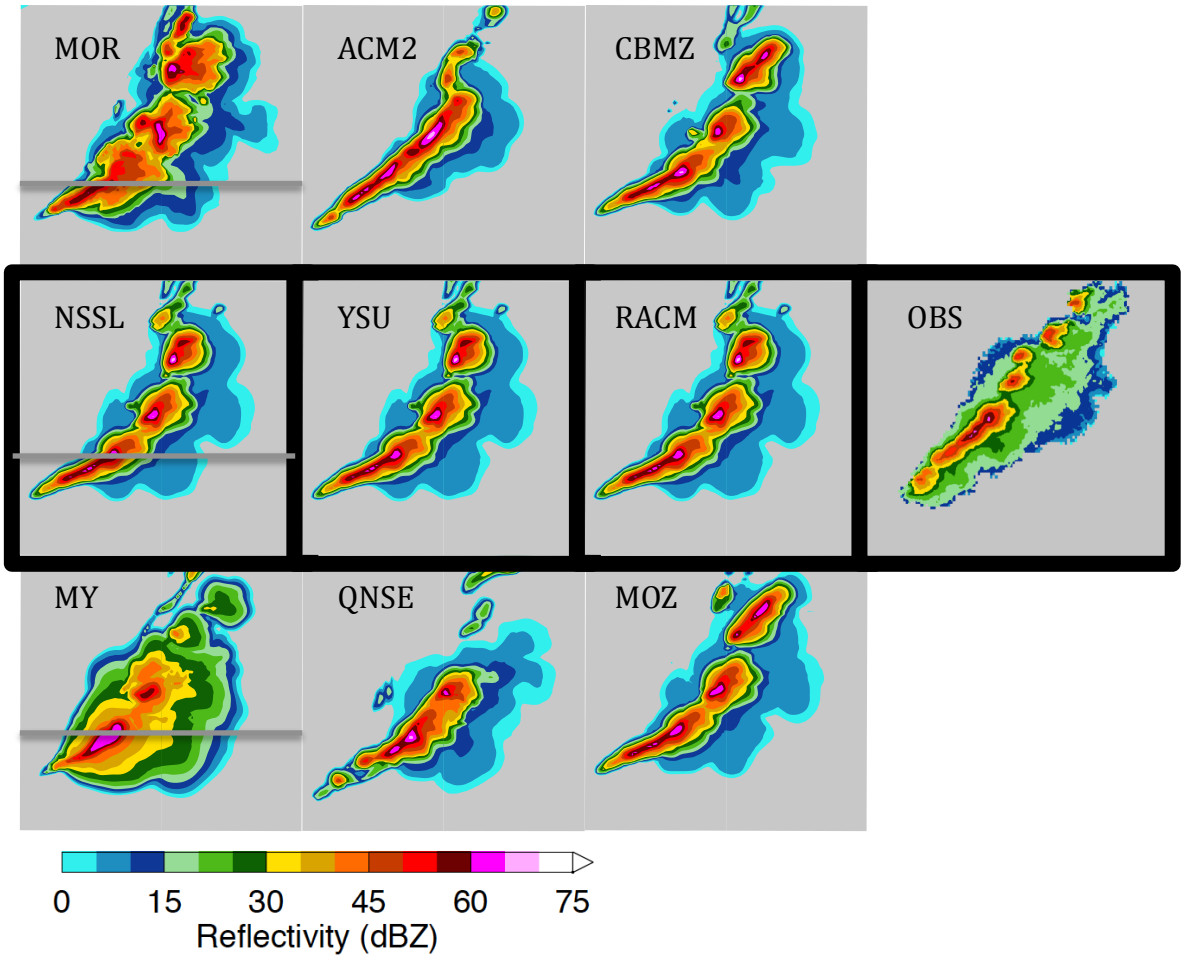

Figure 3. Model simulated column-maximum radar reflectivity for each independent model run compared to the observed radar reflectivity (far right). The left/middle/right columns show the result of varying BMP/PBL/Chemical mechanism. The middle row (outlined with the thick black border) shows the parameterization choices held constant during the sensitivity tests of each. The gray lines through the three BMP (left panel) images show the cross section line used for Figure 9.

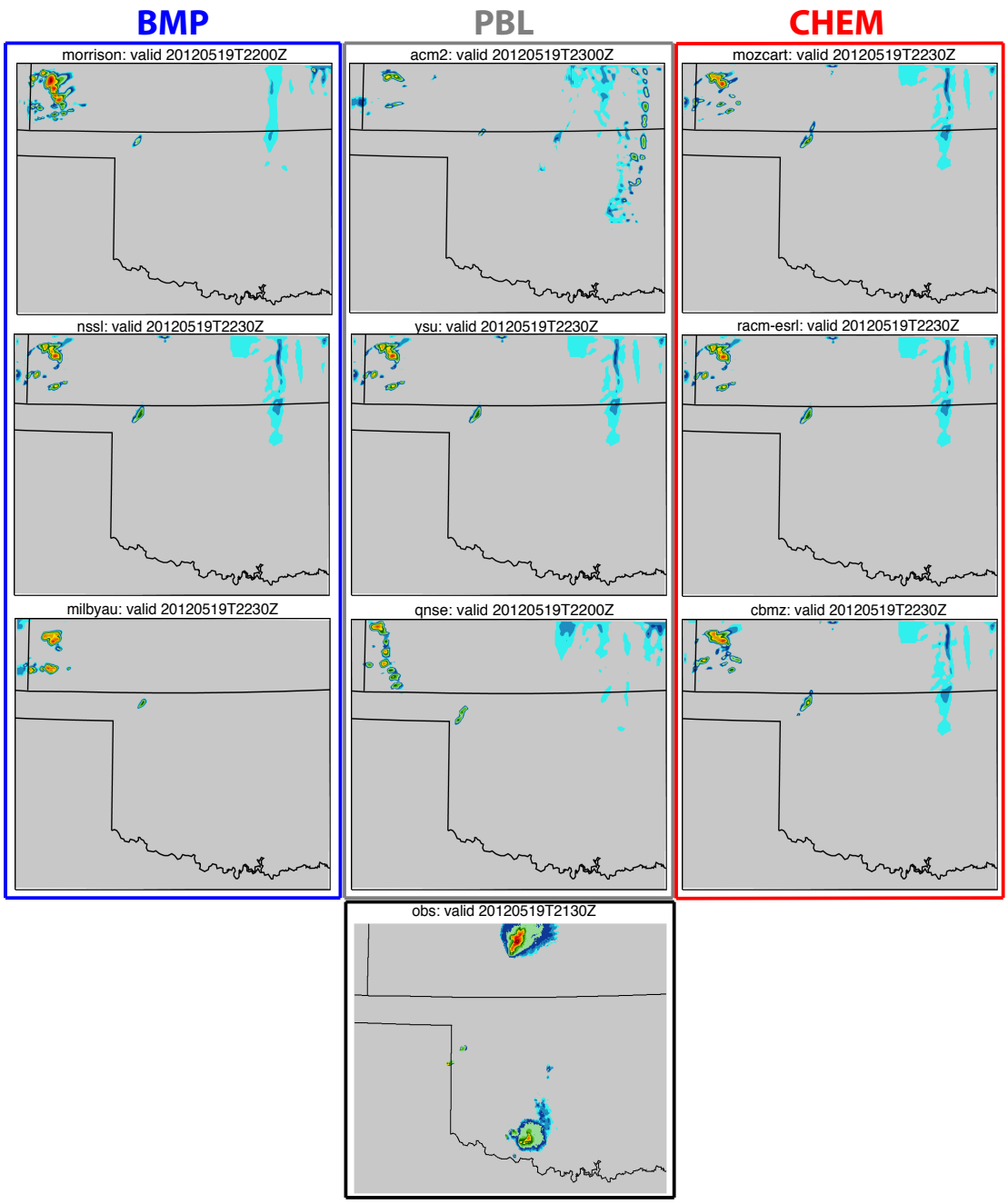

Figure 4. Observed and WRF-simulated reflectivity at the time of convective initiation to nearest half hour. Bulk microphysics parameterizations are shown in the left column (blue outline), planetary boundary layer schemes are shown in the middle column (gray outline), and chemical mechanisms are shown in the right column (red outline). The observed storm is shown in the middle column at the bottom (black outline). The scheme name and time of convective initiation is shown in the heading above each frame.

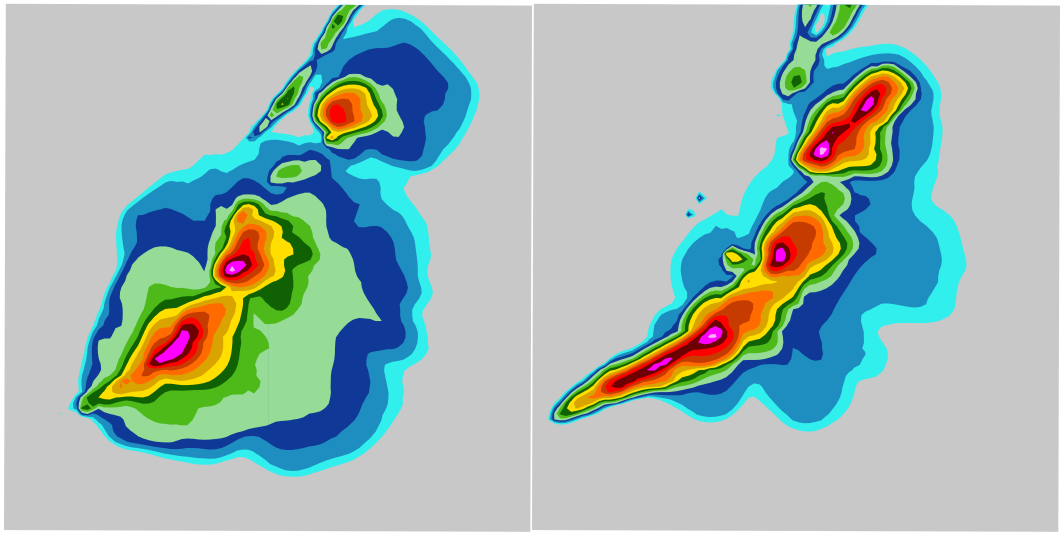

Figure 5. Column maximum reflectivity at 0100 UTC 20 May 2012 from the two simulations run with CBMZ chemistry and MOSAIC 4-bin aerosols. The simulation with aerosol direct and indirect effects is shown on the left and the simulation without these interactions is shown on the right.

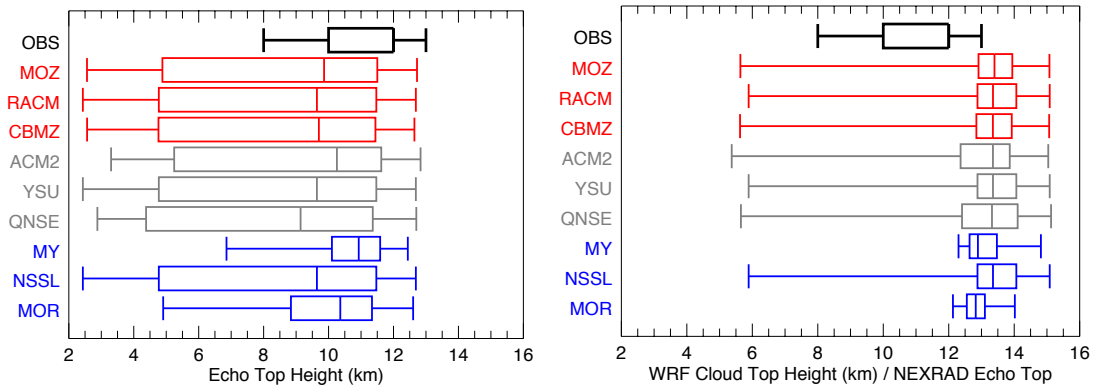

Figure 6. Box-and-whisker plots of simulated 10 dBZ echo tops (left) and cloud tops (right) and observed 10 dBZ echo tops (left and right; black box-and-whiskers). The observed 10 dBZ echo top is shown with the simulated cloud tops for comparison. The chemical mechanisms, PBL schemes, and BMPs are shown in red, gray, and blue, respectively. The extrema of the box-and-whiskers show the minima and maxima of each distribution and the vertical lines of the boxes show the 25th, 50th, and 75th percentiles of the distribution. Note that the median for the observations overlaps with the 25th percentile.

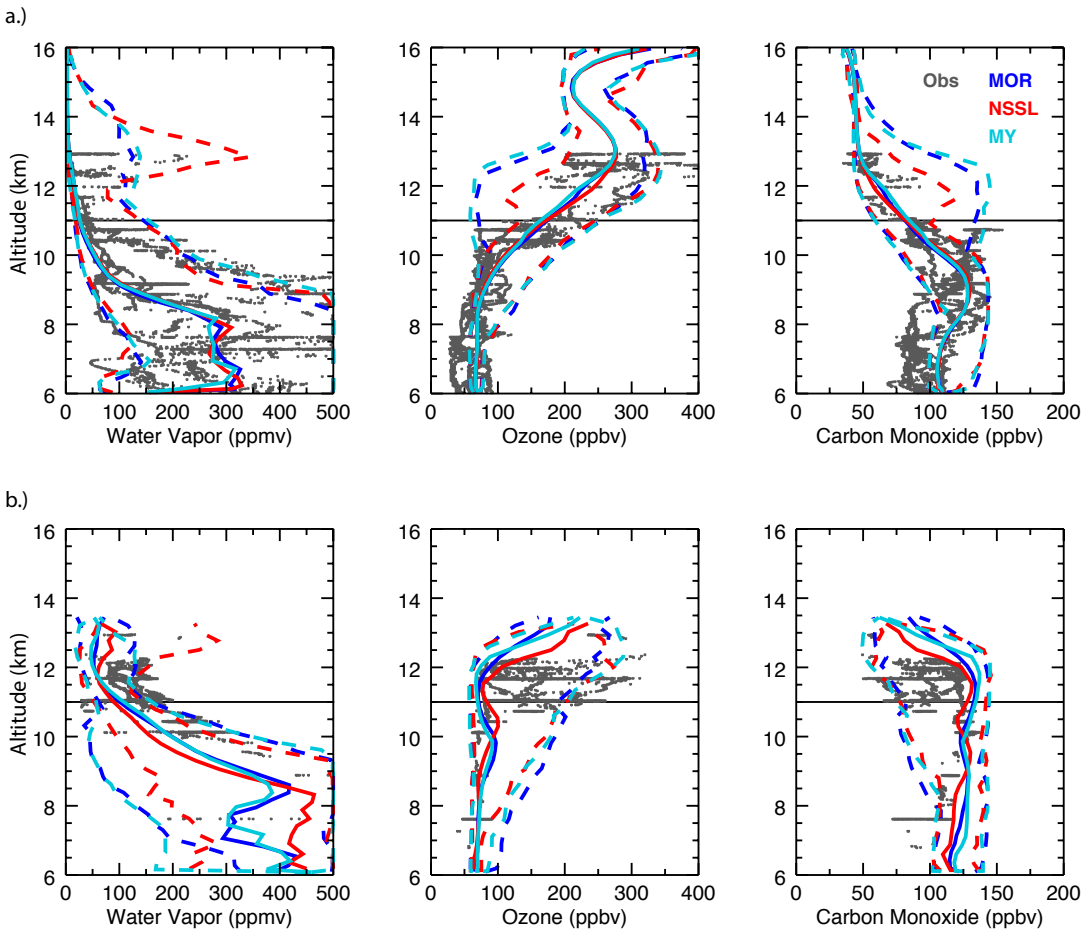

Figure 7. Simulated trace gas profiles of water vapor (left), ozone (middle), and carbon monoxide (right) for the three BMPs compared to the observed concentrations from the DC8 and GV (dark gray dots in each panel). Out-of-cloud profiles are shown on top (7a.) while in-cloud profiles are shown on the bottom (7b.). The dashed lines to the left of the solid line represent the minimum simulated concentration, the solid lines represent the median concentration, and the dashed lines to the right of the solid line represent the maximum concentration. The black line at an altitude of ~11 km denotes the location of the environmental LRT.

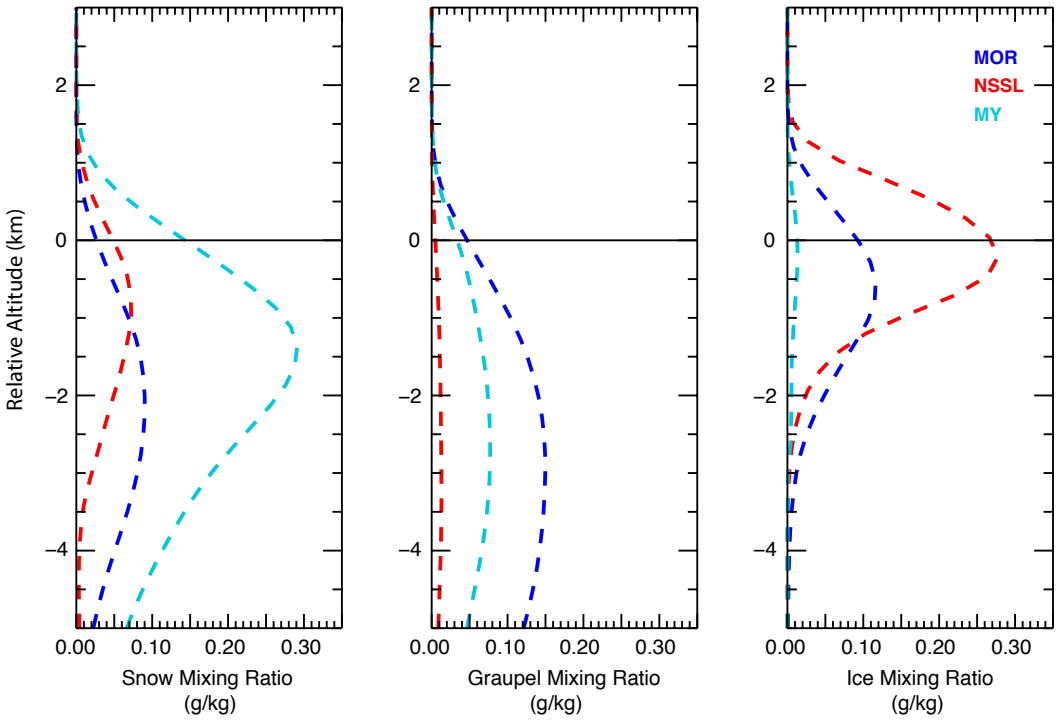

Figure 8. Mean mass mixing ratio of frozen hydrometeors at relative altitude to the tropopause in the three simulations run with different BMPs. Concentrations of snow (left), graupel (middle), and ice (right) were averaged over a subset of the 2-km nested domain shown in Figure 2.

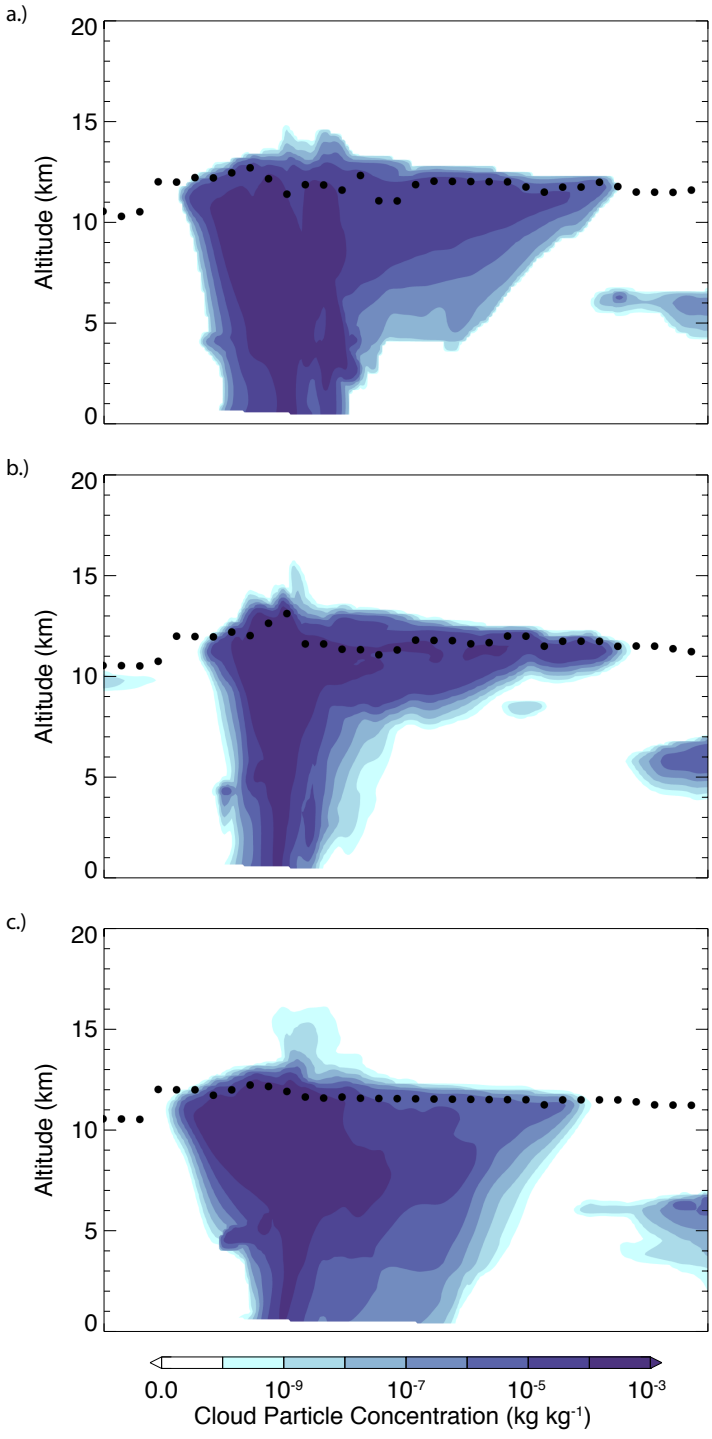

Figure 9. Vertical cross sections of cloud particle concentration (color fill) for simulations with the 3 BMPs: (a) Morrison, (b) NSSL, and (c) Milbrandt and Yau. The black dots show the location of the LRT. The location of the cross section line is shown in Figure 3 and is comparable to each storm (i.e. the cross sections are insensitive to the exact placement of the cross section line).

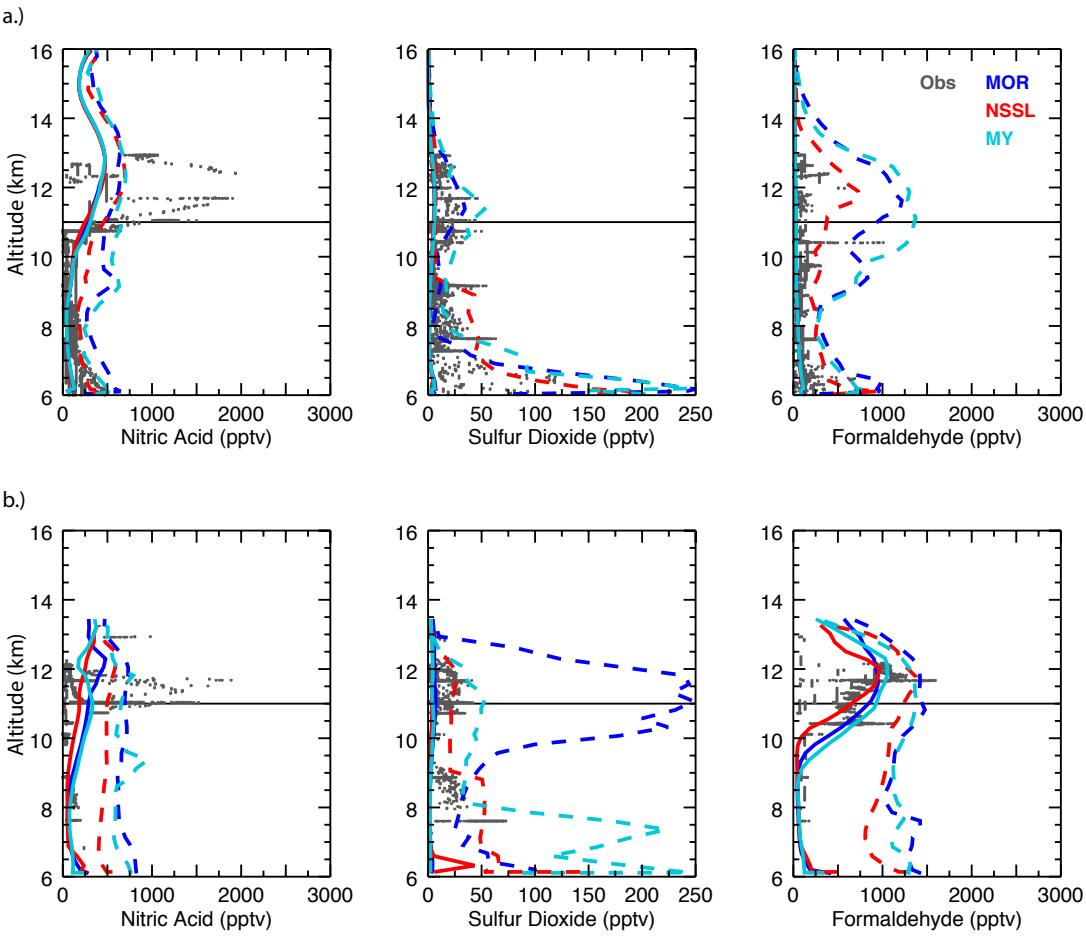

Figure 10. As in Fig. 7, but for three soluble trace gases: nitric acid (left), sulfur dioxide (middle), and formaldehyde (right).

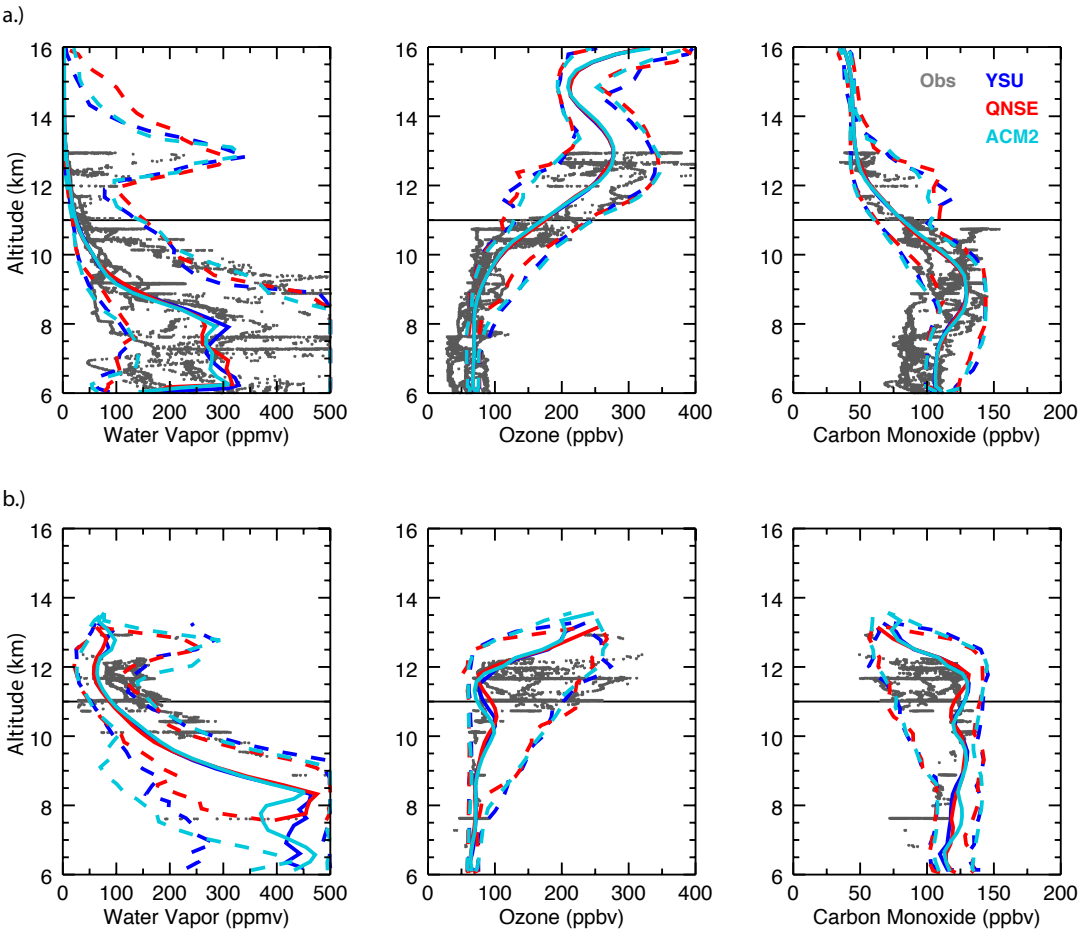

Figure 11. As in Fig. 7, but for the PBL schemes.

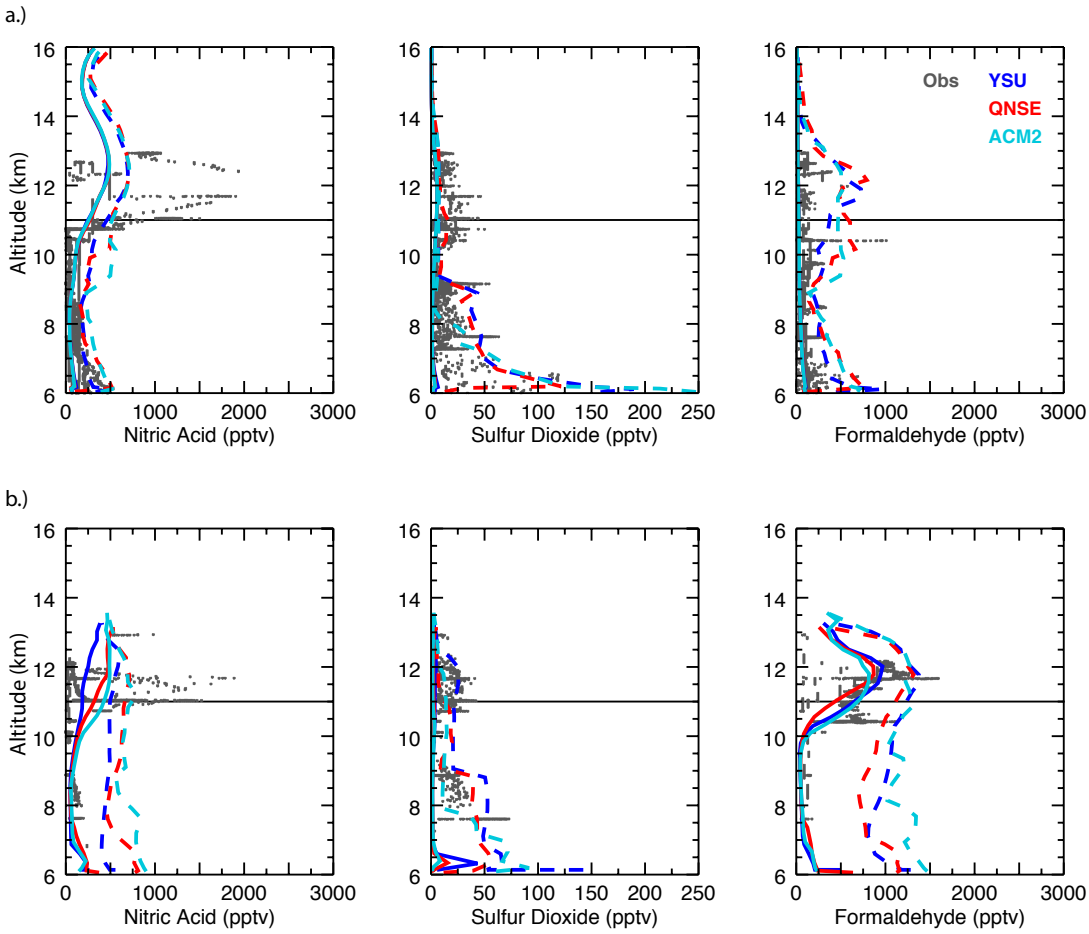

Figure 12. As in Fig. 10 but for the PBL schemes.

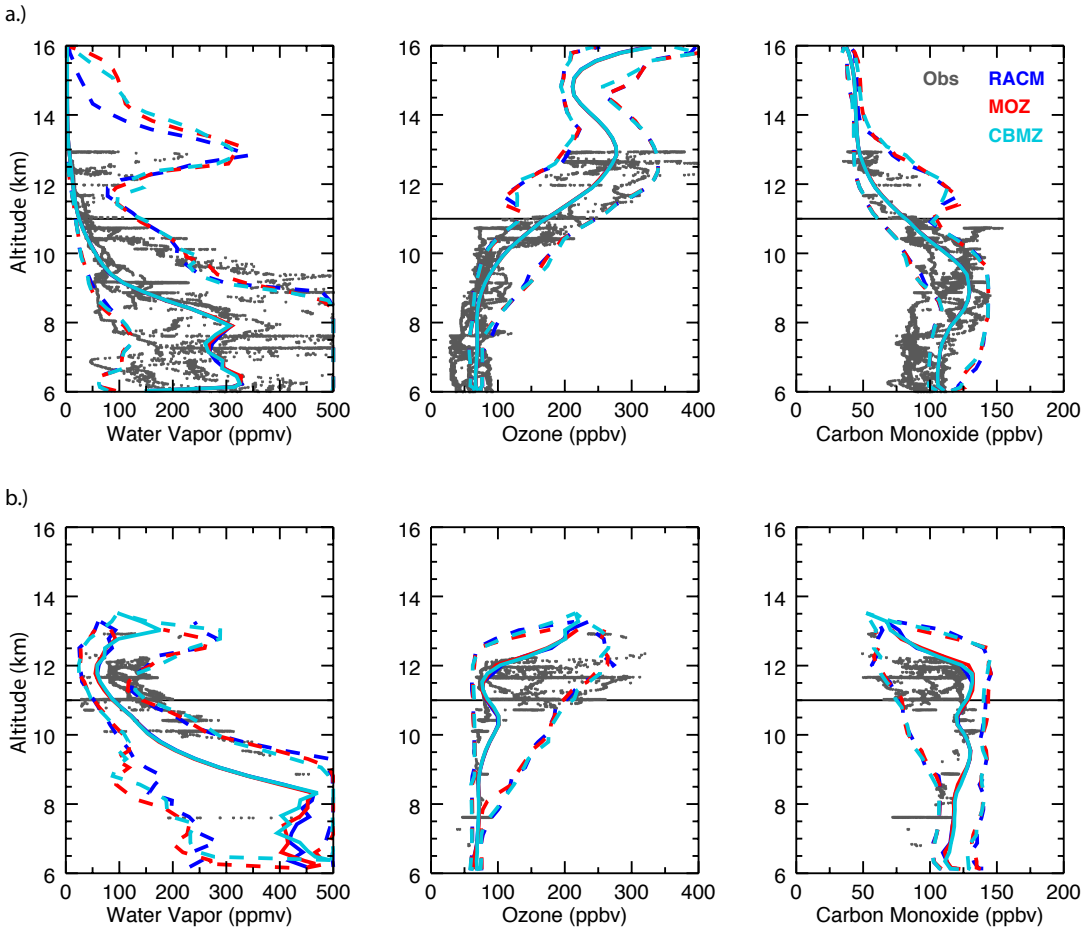

Figure 13. As in Fig. 7, but for the chemical mechanisms.

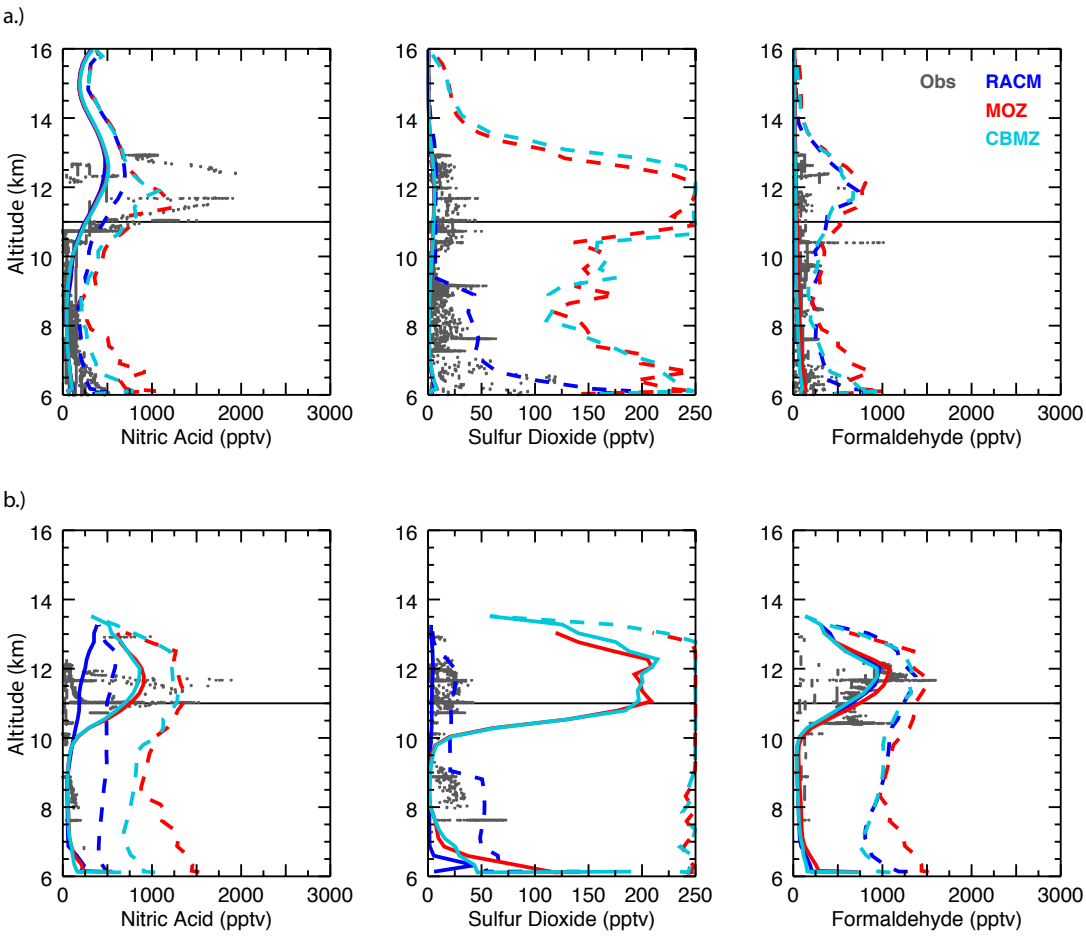

Figure 14. As in Fig. 10, but for the chemical mechanisms.

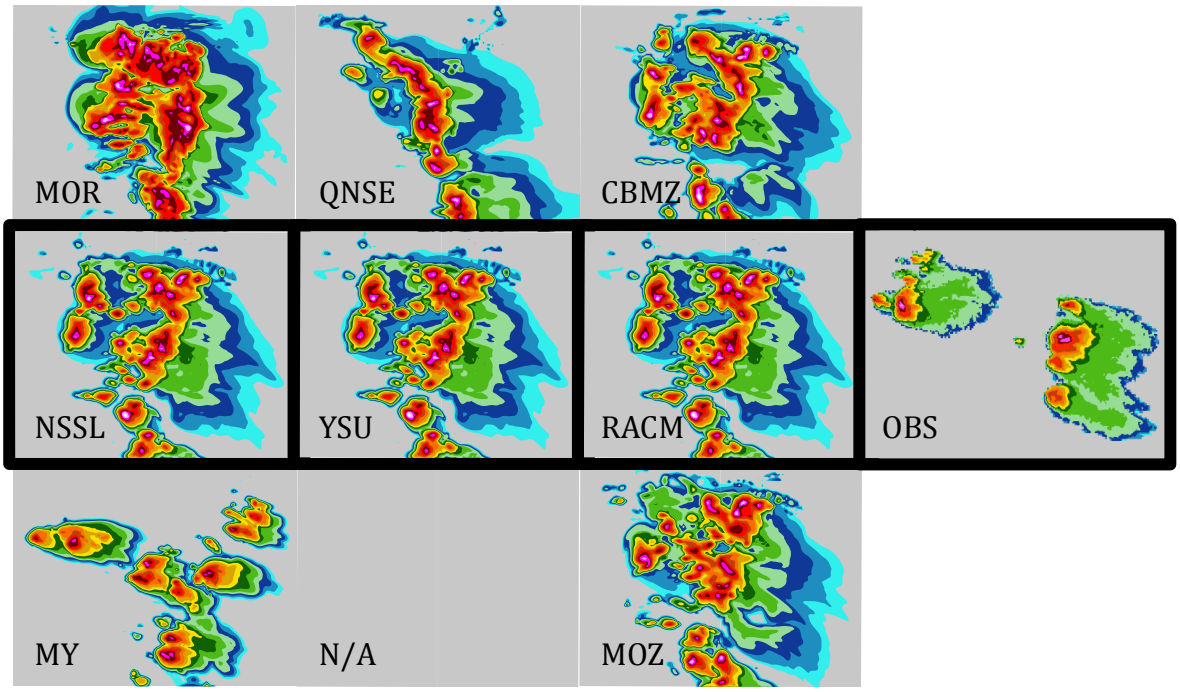

Figure 15. Model simulated column-maximum radar reflectivity for each independent model run compared to the observed radar reflectivity (far right) for the 29 May 2012 case. The left/middle/right columns show the result of varying BMP/PBL/Chemical mechanism. The middle row (outlined with the thick black border) shows the parameterization choices held constant during the sensitivity tests of each. The blank gray box labeled 'N/A' is shown in place of ACM2.

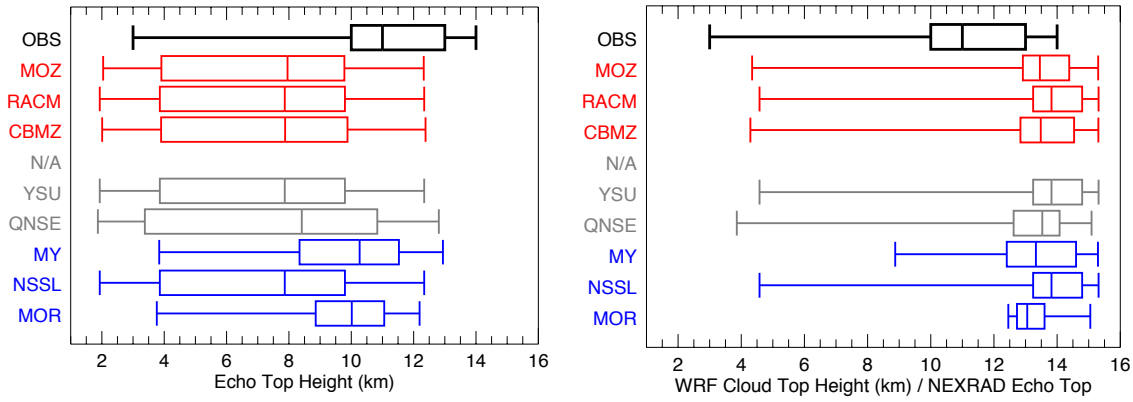

Figure 16. Box-and-whisker plots of simulated 10 dBZ echo tops (left) and cloud tops (right) and observed 10 dBZ echo tops (left and right; black box-and-whiskers) for the 29 May 2012 case. The chemical mechanisms, PBL schemes, and BMPs are shown in red, gray, and blue, respectively. The extrema of the box-and-whiskers show the minima and maxima of each distribution and the vertical lines of the boxes show the 25th, 50th, and 75th percentiles of the distribution.

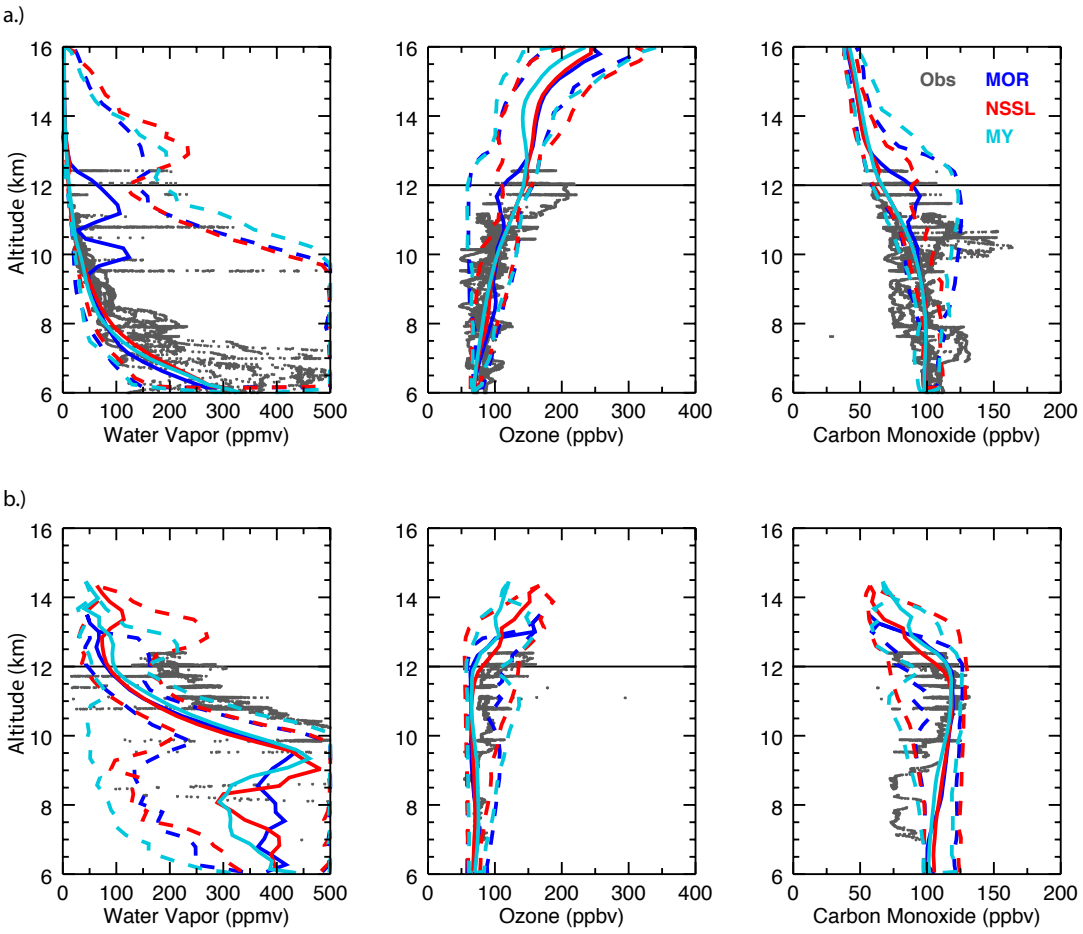

Figure 17. Simulated trace gas profiles at relative altitude to the tropopause of water vapor (left), ozone (middle), and carbon monoxide (right) for the three BMPs compared to the observed concentrations from the DC8 and GV (gray dots in each panel) for the 29 May 2012 case. Out-of-cloud profiles are shown on top (a) while in-cloud profiles are shown on the bottom (b). The dashed lines to the left of the solid line represent the minimum simulated concentration, the solid lines represent the median concentration, and the dashed lines to the right of the solid line represent the maximum concentration. The solid horizontal line marks the location of the tropopause.

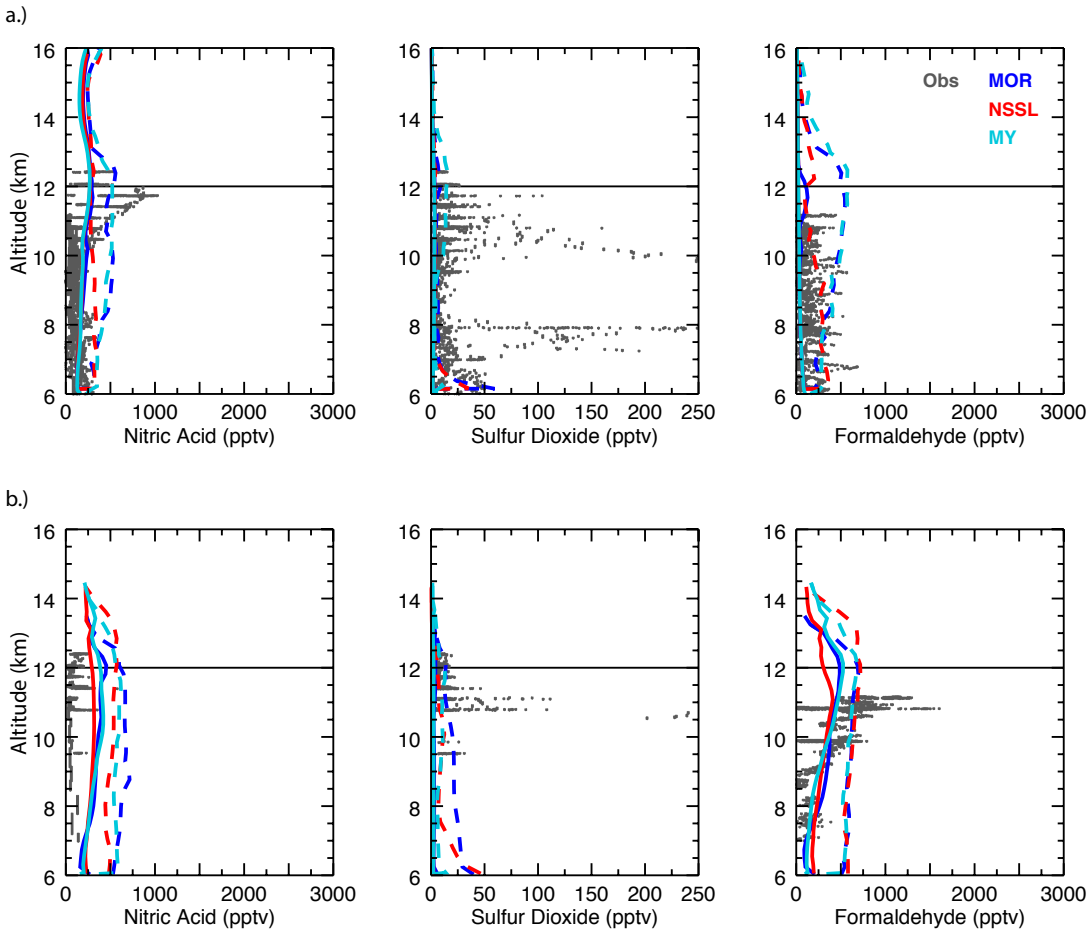

Figure 18. As in Figure 17, but for three soluble trace gases: nitric acid (left), sulfur dioxide (middle), and formaldehyde (right).

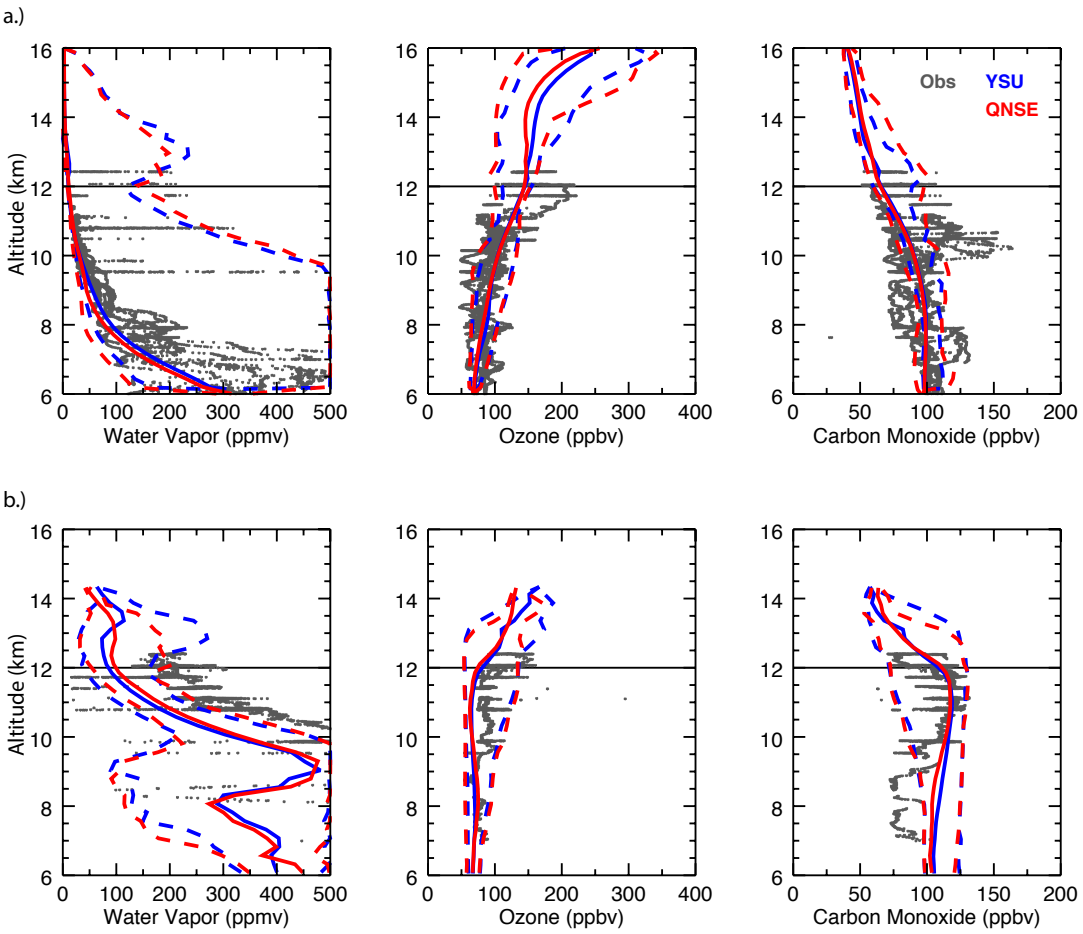

Figure 19. As in Figure 17, but for the PBL schemes.

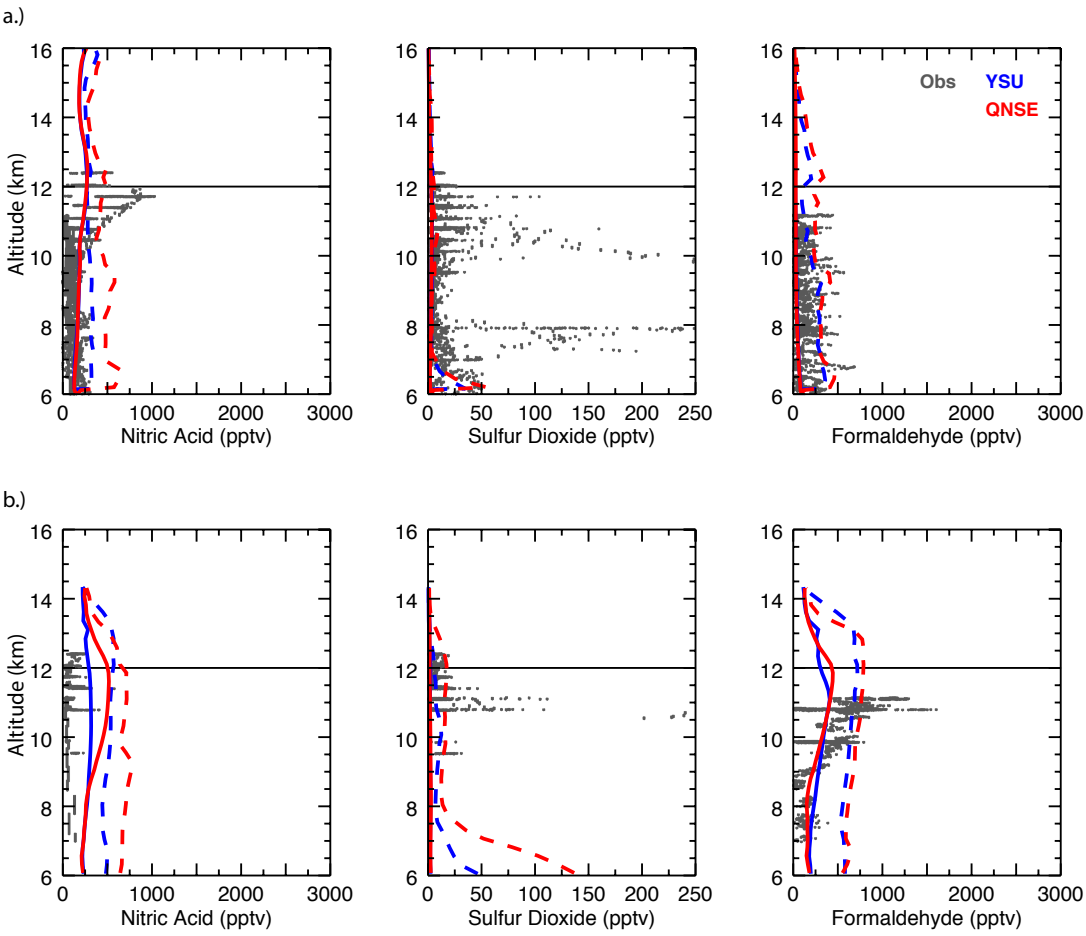

Figure 20. As in Figure 18, but for the PBL schemes.

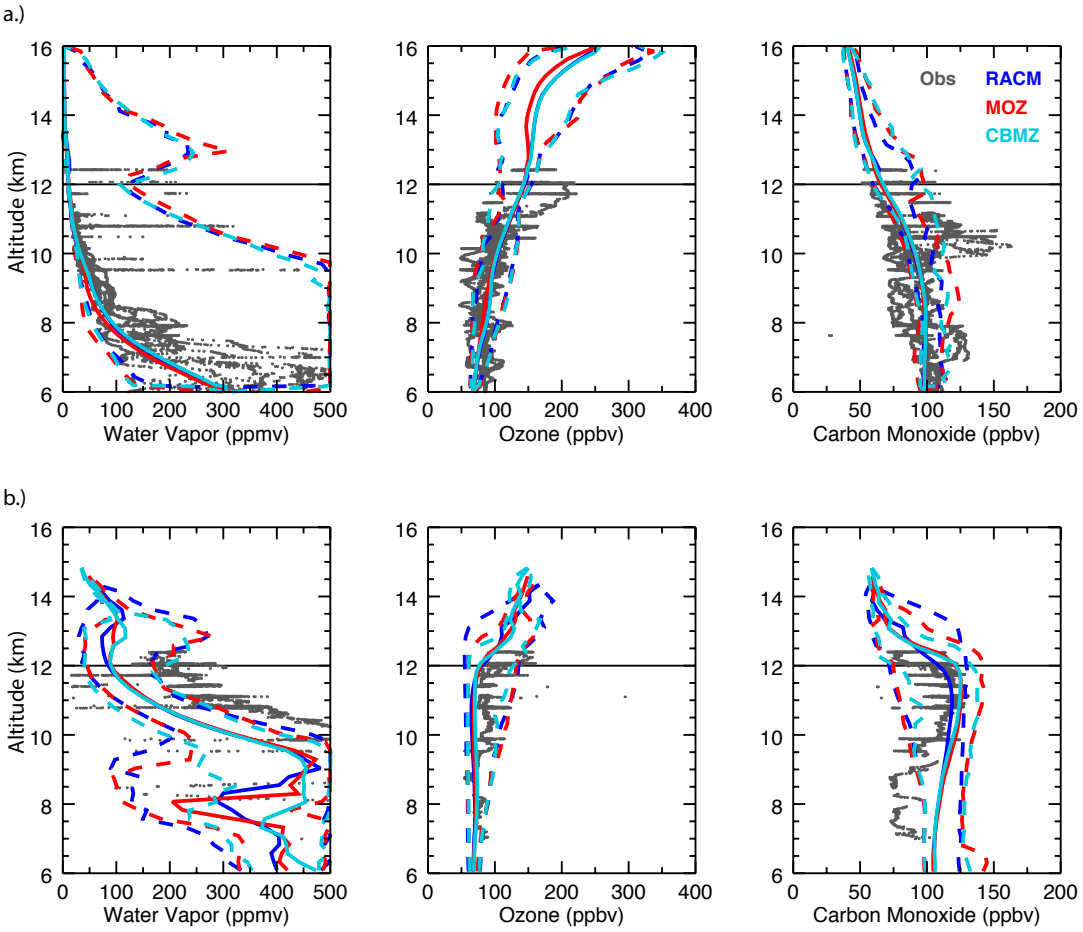

Figure 21. As in Figure 17, but for the chemical mechanisms.

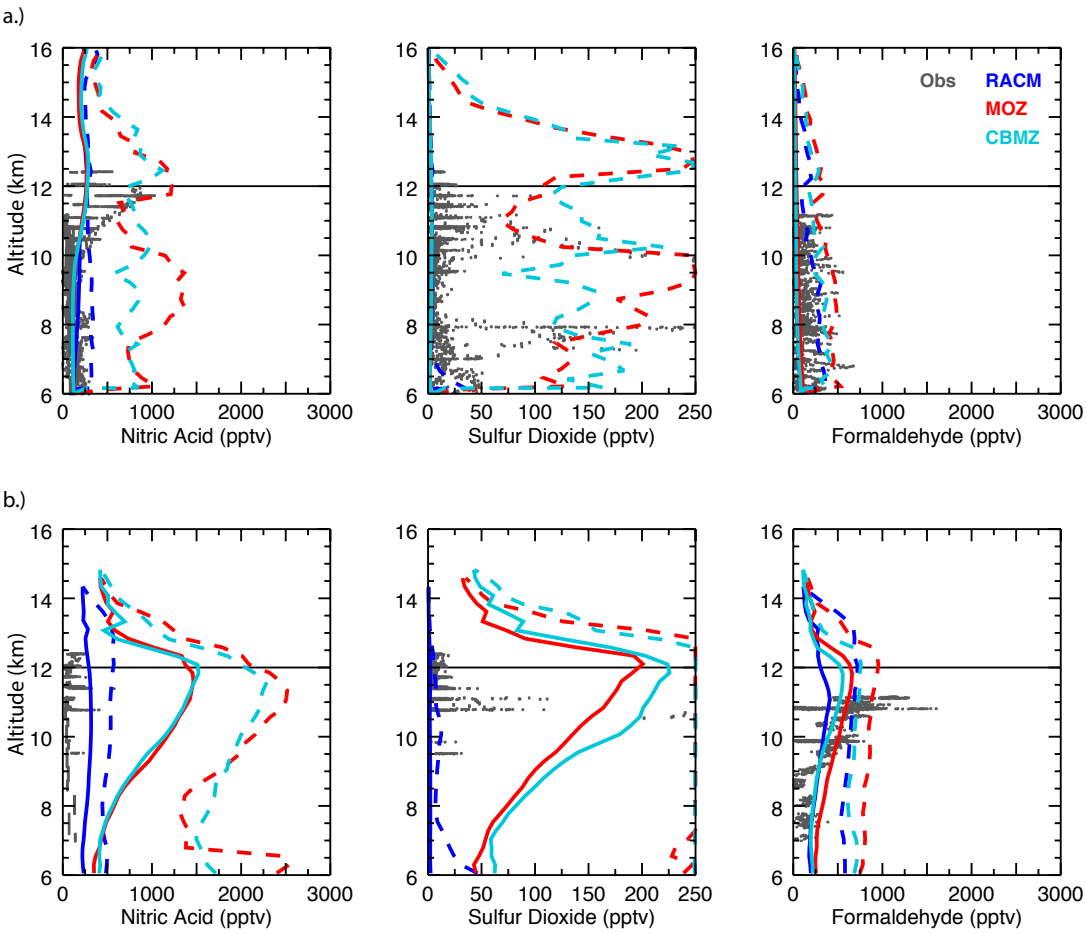

Figure 22. As in Figure 18, but for the chemical mechanisms.

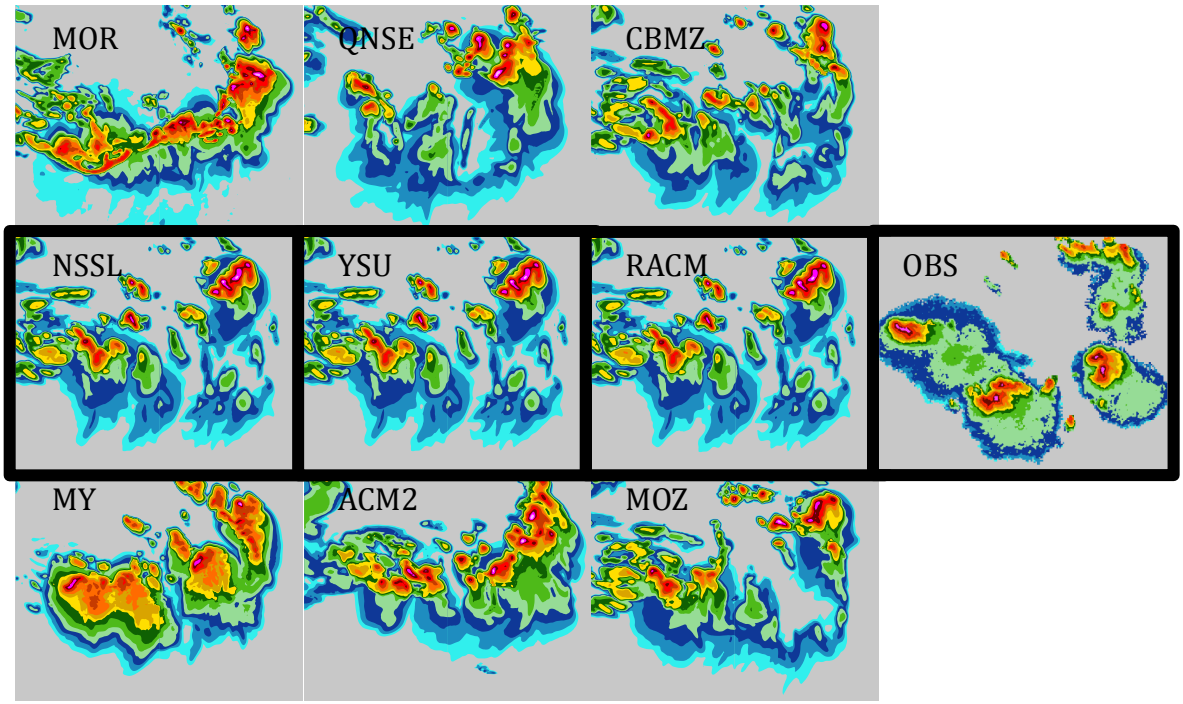

Figure 23. As in Figure 15, but for the 1 June 2012 case.

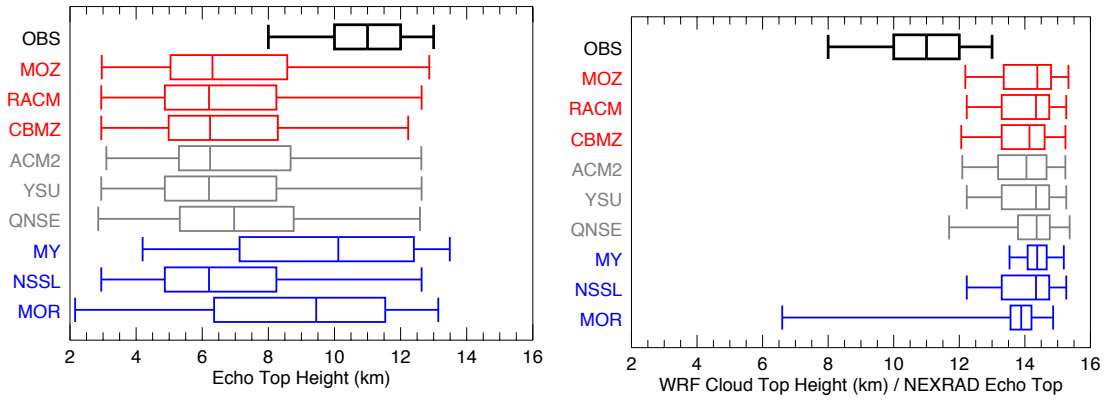

Figure 24. As in Figure 16, but for the 1 June 2012 case.

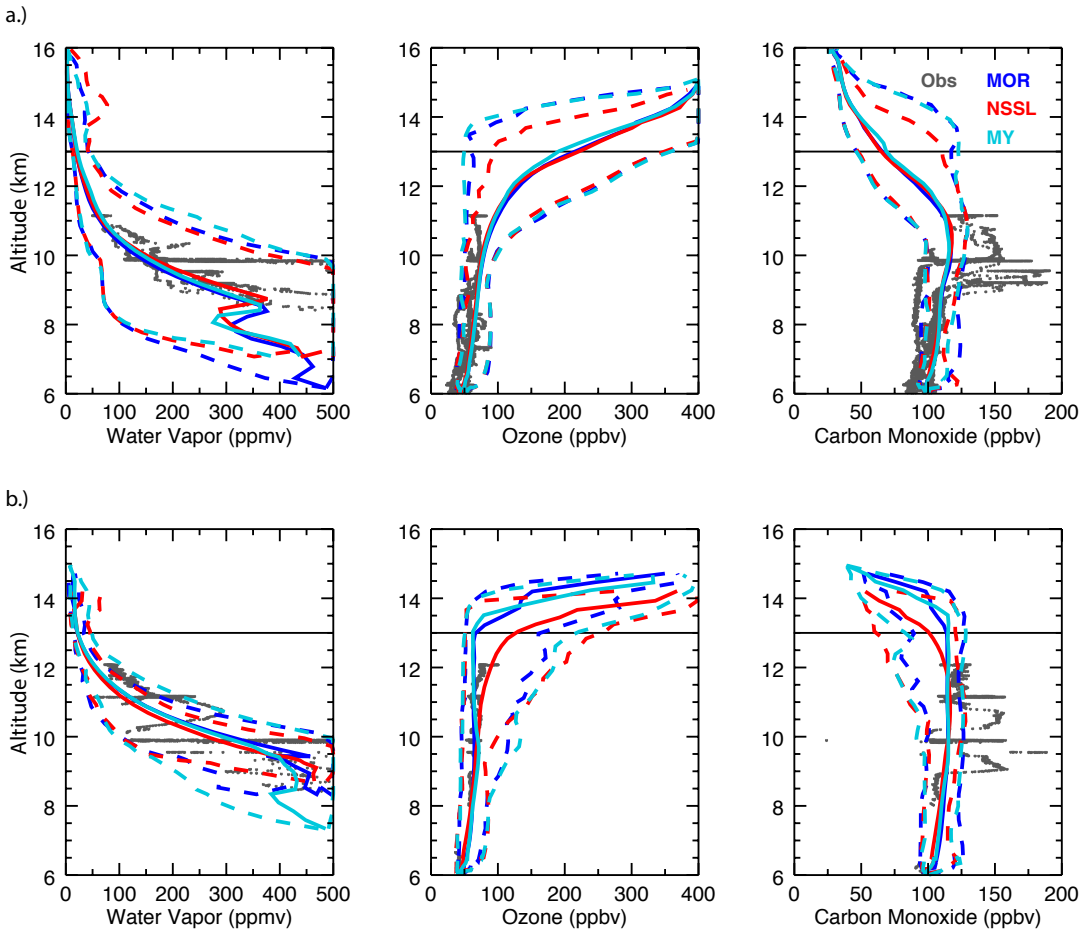

Figure 25. As in Figure 17, but for the 1 June 2012 case.

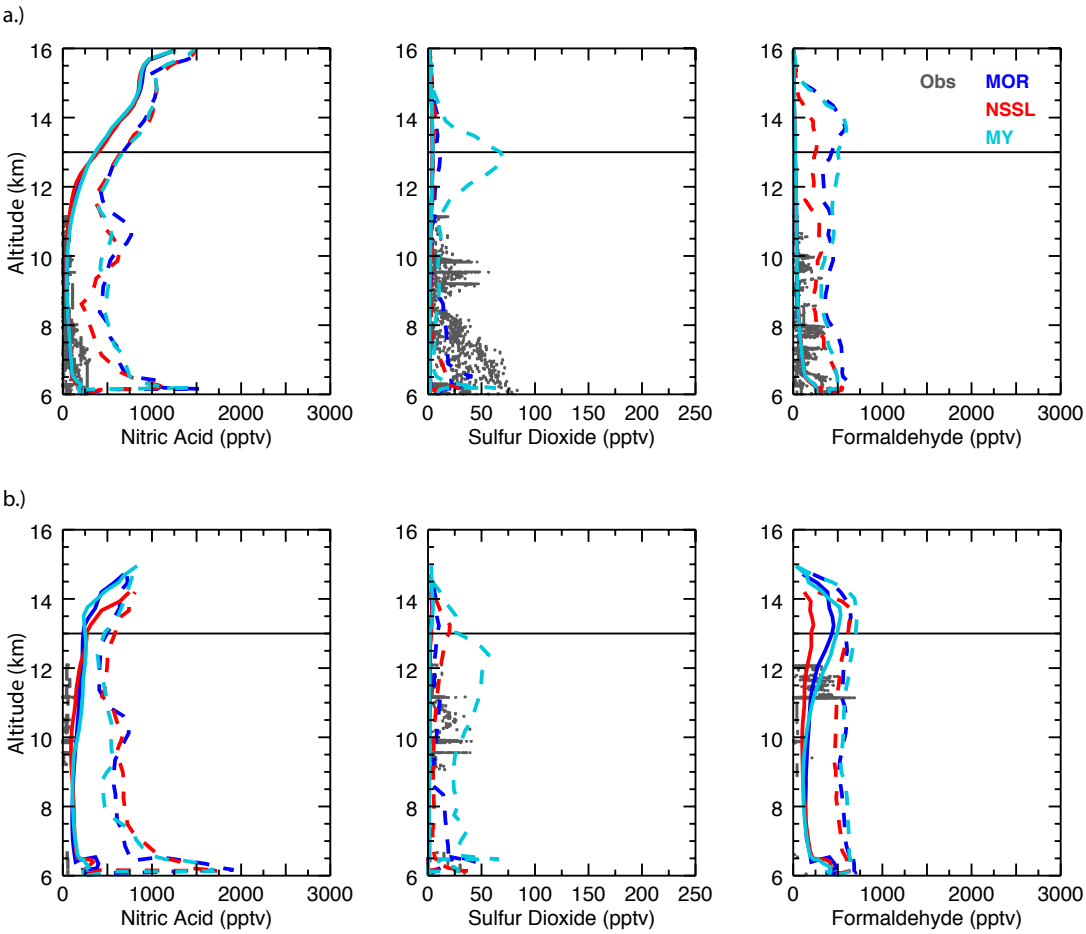

Figure 26. As in Figure 18, but for the 1 June 2012 case.

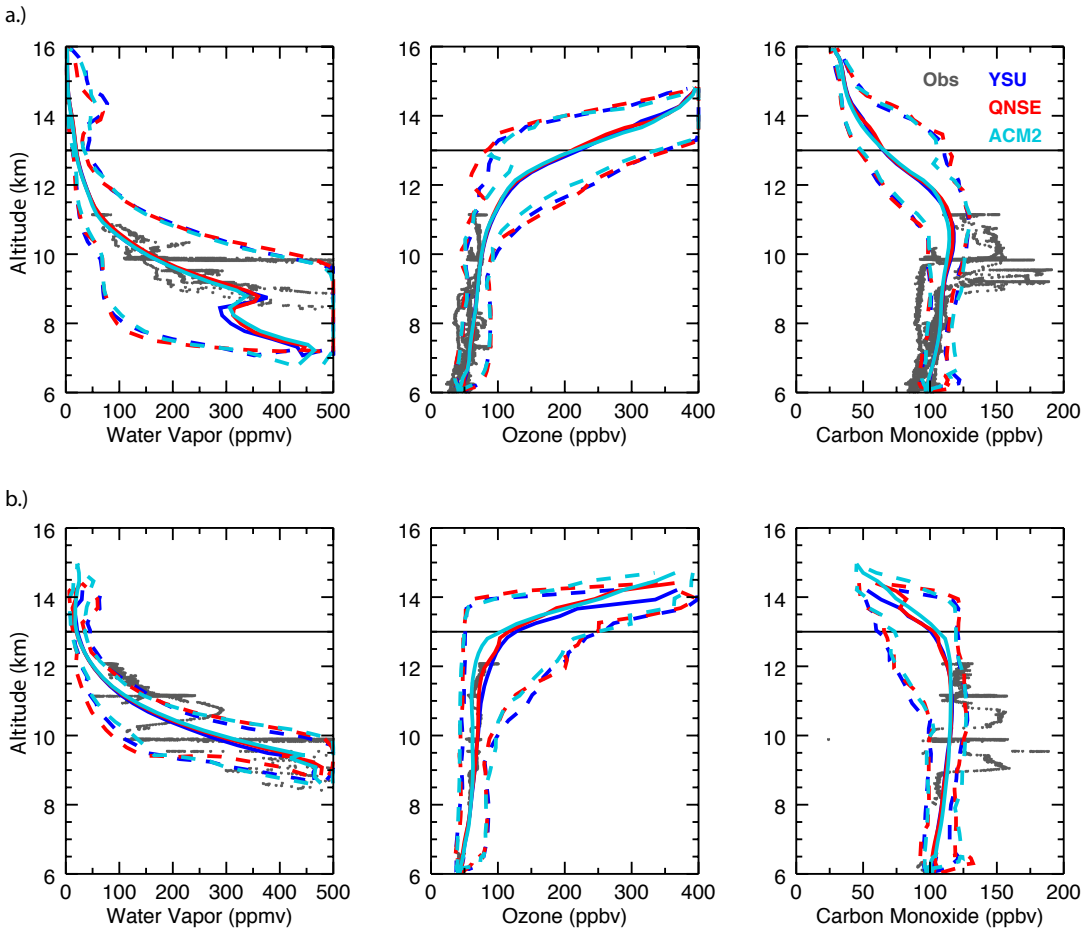

Figure 27. As in Figure 19, but for the 1 June 2012 case.

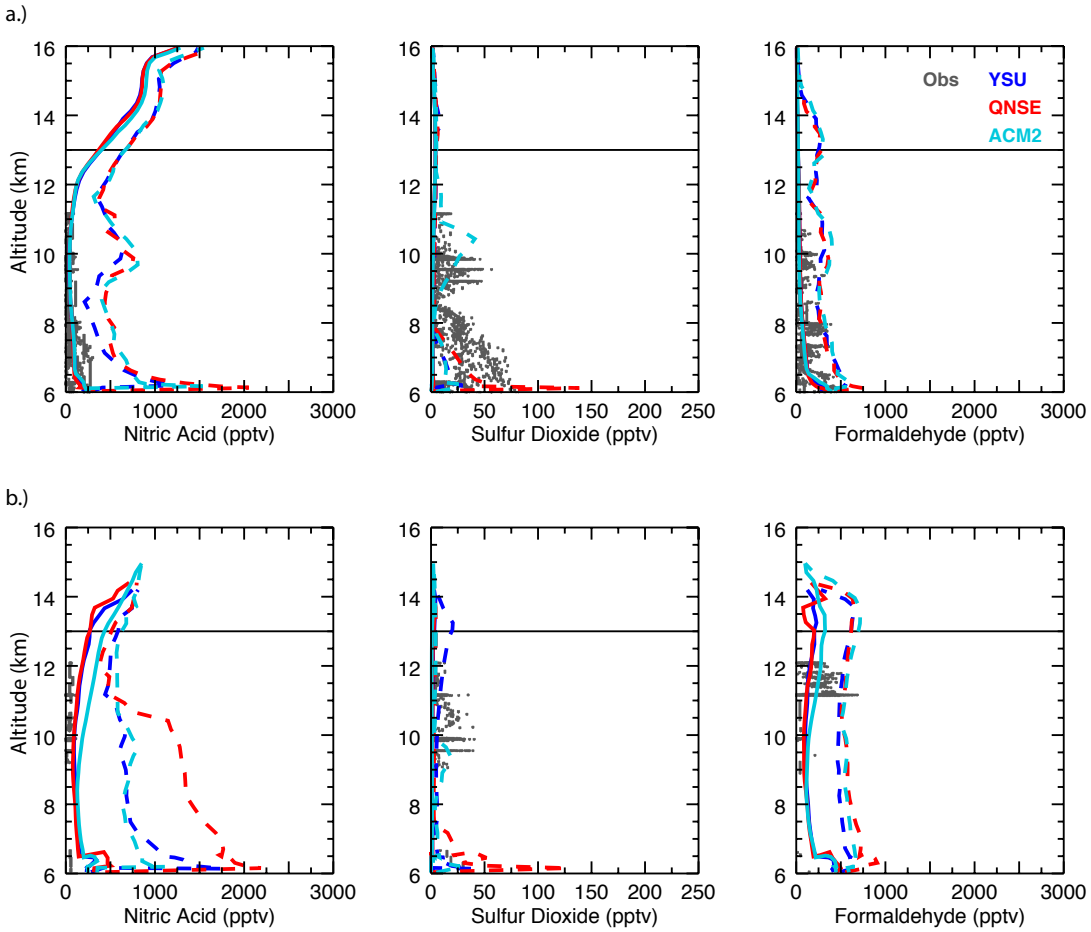

Figure 28. As in Figure 20, but for the 1 June 2012 case.

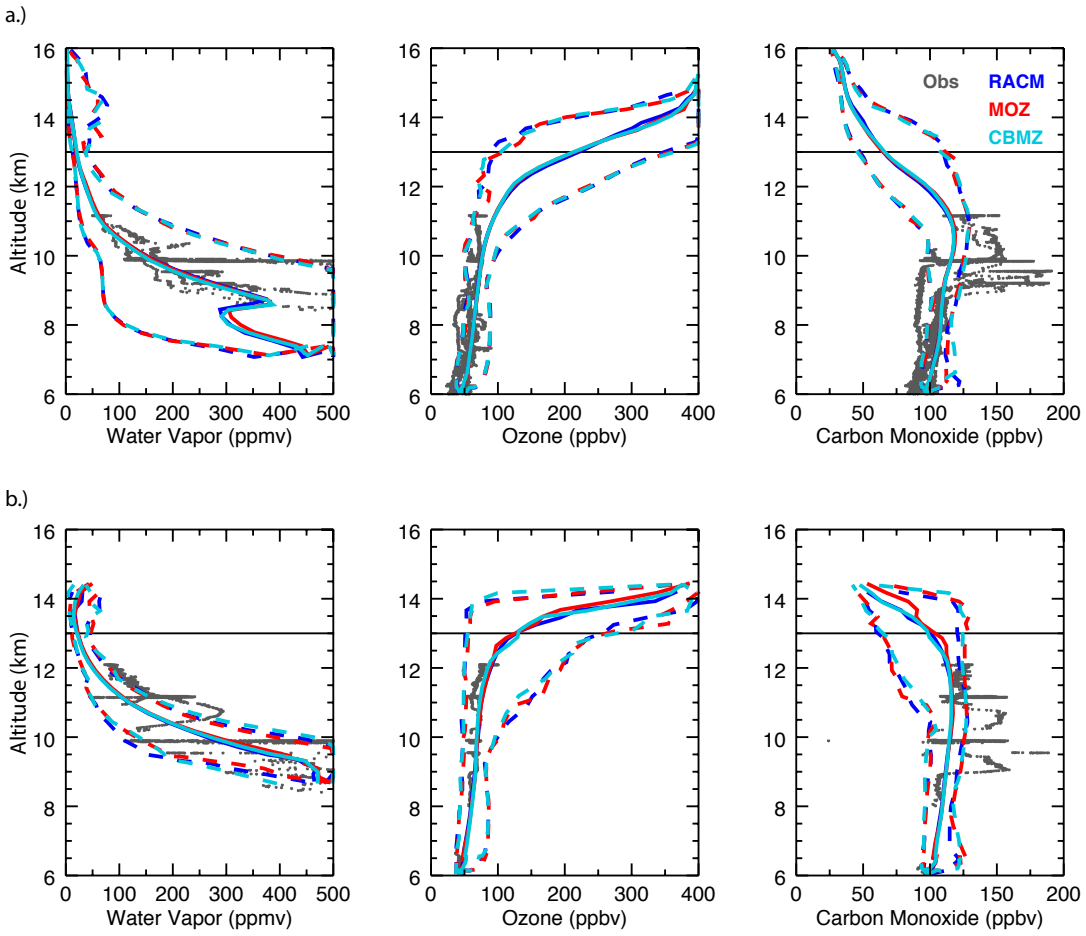

Figure 29. As in Figure 21, but for the 1 June 2012 case.

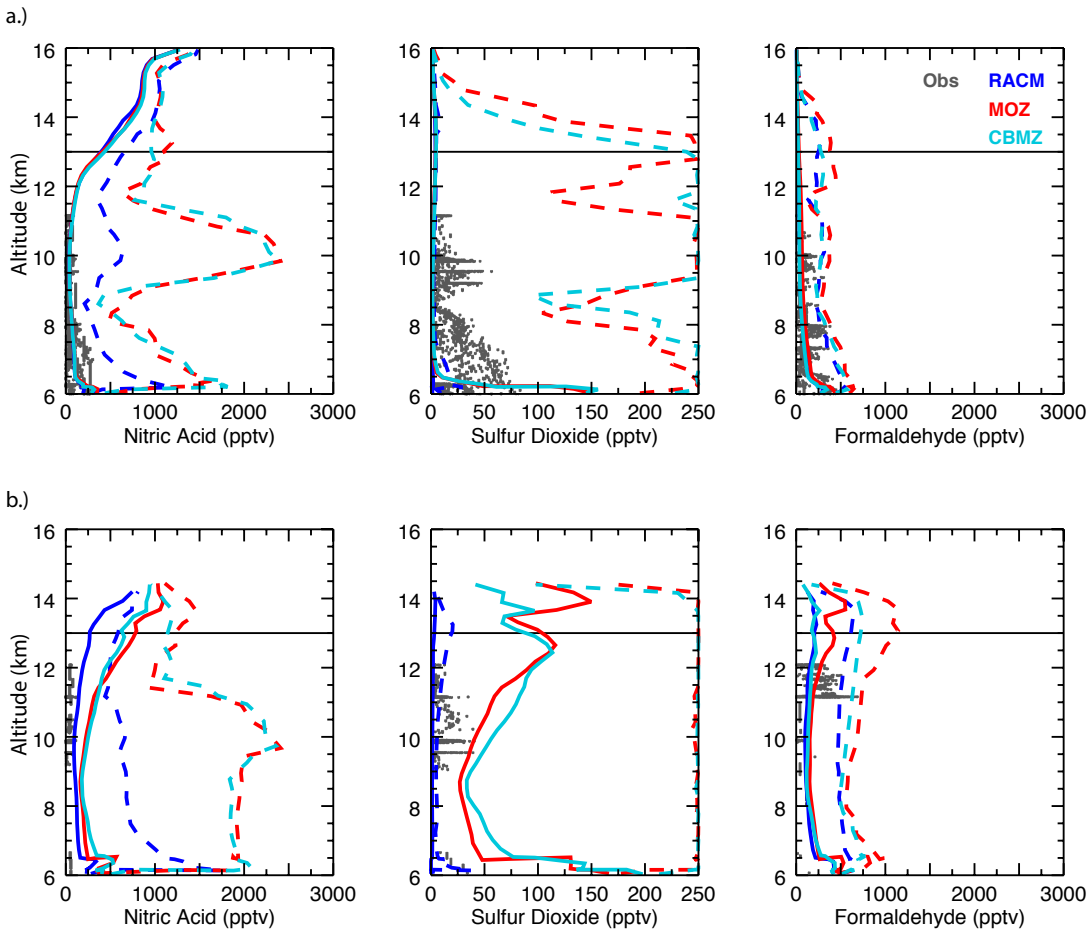

Figure 30. As in Figure 22, but for the 1 June 2012 case.

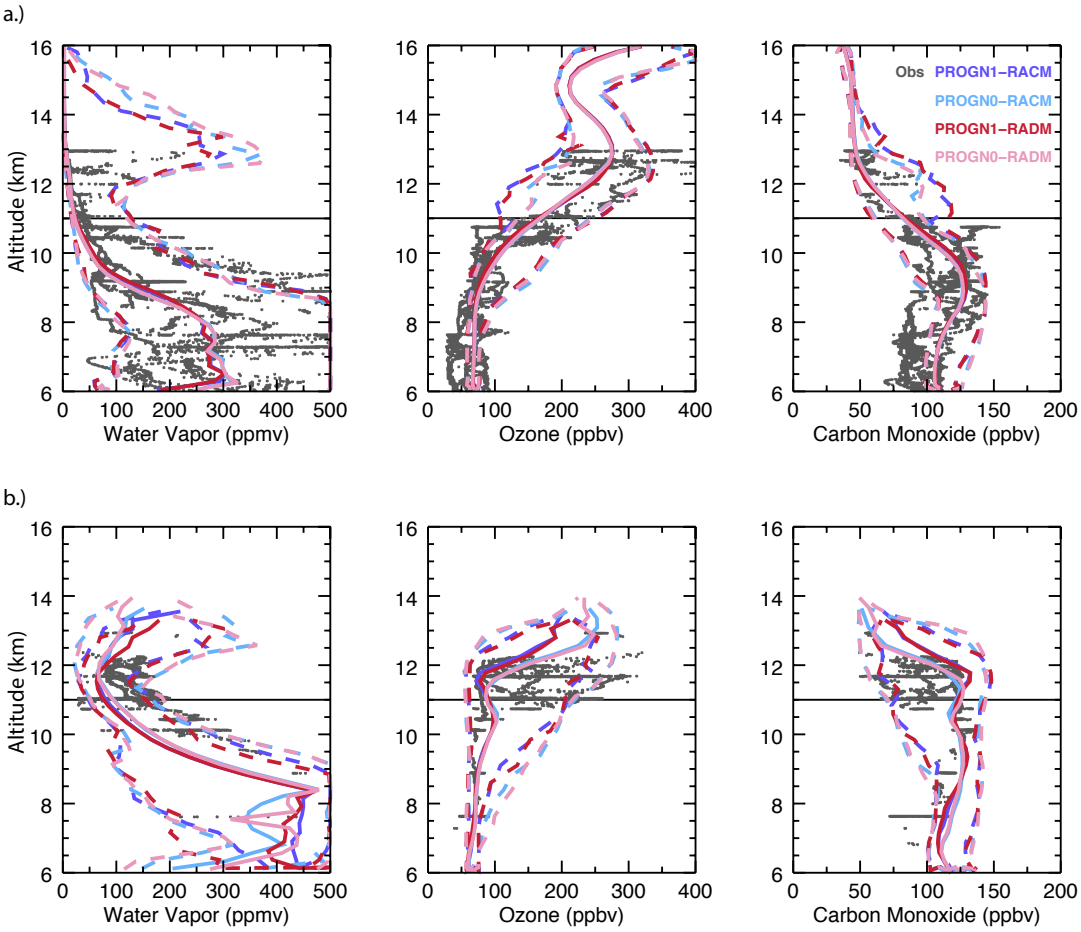

Figure 31. As in Figure 17, but for simulations run with and without prognostic aerosols. Blue shades show simulations run with RACM-ESRL chemistry while red shades show simulations run with RADM2 chemistry. Lighter shades show the simulations run with prognostic aerosols turned off.

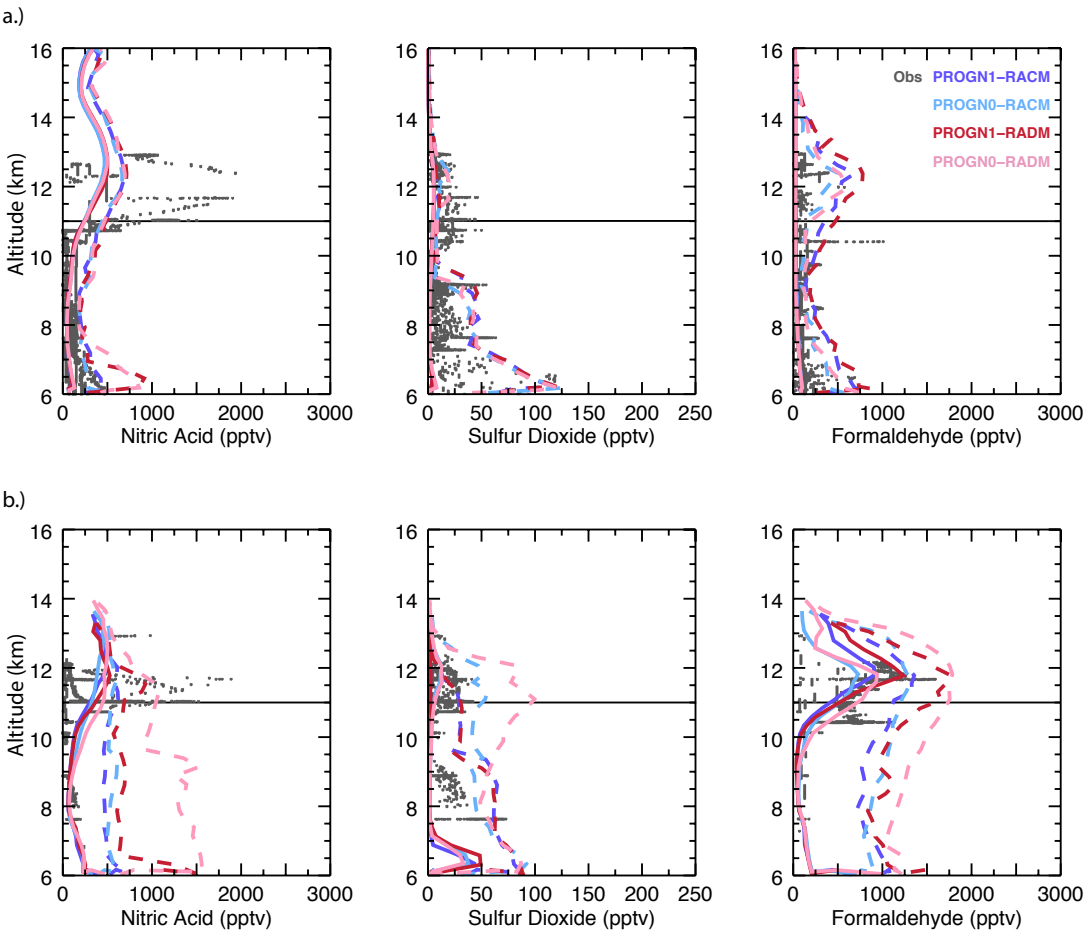

Figure 32. As in Figure 18, but for simulations run with and without prognostic aerosols. Blue shades show simulations run with RACM-ESRL chemistry while red shades show simulations run with RADM2 chemistry. Lighter shades show the simulations run with prognostic aerosols turned off.

Chapter 3

Mechanisms Responsible for Stratosphere-to-Troposphere Transport Around a Mesoscale Convective System Anvil

Recent observational studies have shown that stratospheric air rich in O_3 is capable of being transported into the upper troposphere in association with tropopause-penetrating convection (anvil wrapping) [*Pan et al.,* 2014]. This finding challenges the current understanding of upper tropospheric sources of O_3, which is traditionally thought to come from thunderstorm outflows where lightning-generated nitrogen oxides facilitates O_3 formation. Since tropospheric O_3 is an important greenhouse gas and the frequency and strength of tropopause-penetrating storms may change in a changing climate [citations], it is important to understand the mechanisms driving this transport process so that it can be better represented in chemistry-climate models.

3.1 Possible Mechanisms for Anvil Wrapping

While our understanding of the anvil wrapping transport process based on previous work is limited, several effects based on our broader understanding of cross-tropopause transport in convection can be hypothesized to explain this transport process, including: i) MCS-scale vertical circulations induced by mass continuity, and ii) their corresponding horizontal branches, which are influenced by differential advection in layers with strong vertical shear occurring within and immediately beneath the MCS anvil outflow, and iii) dynamic and static instabilities (gravity wave breaking, shearing instabilities) driving small-scale vertical mixing.

Mass conservation has been hypothesized as a mechanism for downward transport of stratospheric air as a response to deep convection crossing the tropopause layer into the stratosphere [*Tang et al*., 2011]. Global chemical transport model simulations of stratosphere-troposphere exchange of O_3 showed that mid-latitude convection was capable of reaching stratospheric levels of O_3 (250 ppb), resulting in STT that enhanced

the O_3 flux by 19% of the northern hemisphere total [*Tang et al*., 2011]. However, the horizontal grid spacing was 1°x1° with a 1 km vertical resolution in the tropopause region in this modeling study. While the model results compared well with satellite and ozonesonde observations, the O_3 flux and responsible mechanisms for transport are likely influenced by the vertical and horizontal model resolution [*Homeyer*, 2015]. In particular, STT is found to be higher with smaller vertical grid spacings and larger horizontal grid spacings. Model simulations performed at smaller vertical and horizontal grid spacings are needed to understand if mass conservation still plays a role in STT of O_3 around convective systems.

Perturbation pressure circulations atop storms with overshooting tops could force subsidence near the anvil edge that is consistent with the wrapping process (see *Fujita*, 1974, Fig. 15). In the overshoot, the air is colder than its environment, creating a hydrostatic pressure that is higher than the surrounding air (a mesohigh aloft). *Fujita* [1974] proposed that the horizontal pressure gradient between the mesohigh and surrounding lower pressure aloft drives a divergent flow of air above the anvil top, which then descends around the MCS anvil. Such a circulation would explain how O_3-rich air from the lower stratosphere could descend along the anvil of an MCS and into the troposphere.

Strong vertical wind shear atop, within and beneath the MCS upper-level outflow can result in differential advection that is conducive to turbulence generation [*Trier and Sharman*, 2009]. In some cases the differential advection can lead to Kelvin-Helmholtz instability [e.g., *Trier et al*., 2012], whereas in others [e.g., *Trier et al*., 2010] it can promote mixed convective-dynamic instabilities such as thermal-shear instability that can lead to turbulence and enhanced vertical mixing. These instabilities along the edge of an MCS anvil may promote vertical mixing of O_3-rich air from the stratosphere to the troposphere.

Dynamical instabilities occur in deep convective clouds by generating gravity waves near the tropopause when air in the updraft rises above its level of neutral buoyancy, encounters increasingly stable air in the stratosphere, becomes negatively buoyant and accelerates downward, falls below its level of neutral buoyancy and becomes positively buoyant again and repeats this process several times over (i.e., a

mechanical oscillation) [*Fovell et al.,* 1992; *Lane et al*., 2001; *Lane*, 2008; *Ansong and Sutherland*, 2010]. These gravity waves can experience overturning and break if they encounter a critical layer—a layer where the horizontal phase speed of the vertically propagating gravity wave equals the horizontal speed of the background flow—which leads to wave amplification and breaking with enhanced vertical mixing in the UTLS. Several studies have demonstrated the important role that gravity wave breaking plays in stratosphere-troposphere exchange atop tropopause-overshooting convection. *Wang* [2003] showed that wave overturning and breaking can irreversibly transport water across isentropic surfaces and into the lower stratosphere. *Moustaouri et al.* [2004] demonstrated that interactions between gravity waves and a critical layer can cause wave overturning, vertically mixing O_3 and other atmospheric constituents. *Lane and Sharman* [2006] modeled gravity waves generated by deep convection with a three-dimensional cloud-resolving model and found that waves generated by convection propagate into the stratosphere and break, generating a secondary train of waves. This breakdown was shown to cause cross-isentropic mixing of water vapor, and could potentially mix other atmospheric constituents such as O_3. Since the breakdown of these waves can induce irreversible mixing, this could play a role in cross-tropopause transport of stratospheric air (high O_3) into the troposphere.

3.2 Case Description and Model Configuration

3.2.1 30 May 2012 Case Overview

The targeted MCS of the simulation was observed on 30-31 May 2012 as part of the DC3 field campaign and has been described in detail by *Pan et al.* [2014] and *Homeyer et al.* [2014]. Briefly, the observed MCS initiated between central and NW Kansas at about 2100 UTC on 30 May 2012 and moved southeastward across the state. By 0200 UTC on 31 May 2012, the MCS covered most of the state of Kansas and was positioned near the south-central border. The DC-8 aircraft observed the leading-line trailing-stratiform (LLTS) MCS [e.g., *Houze et al*., 1989] around 0200 UTC on 31 May 2012 while it was flying at an altitude of 12.5 km. At this time and location, the LRT altitude (as defined in *WMO* [1957]) was approximately 12 km. Along the aircraft's path (see *Pan et al*., 2014,

their Fig. 1), the DIAL lidar on board the DC-8 observed a two-dimensional curtain (distance along flight path x altitude) of O_3 showing the wrapping feature around the leading anvil. The O_3 concentration in this feature was in excess of 150 ppbv at altitudes as low as 8 km (~4 km below the local tropopause). In clear air away from the MCS, O_3 concentrations were much lower in the upper troposphere, ranging from 60 to 100 ppbv.

3.2.2 Simulation Design

Version 3.7.1 of the Weather Research and Forecasting model [*Skamarock et al.,* 2008] coupled with Chemistry [*Grell et al.,* 2005; *Fast el al.,* 2006] was used for this study. The model configuration is the same as described in Chapter 2, unless otherwise noted here. Since Chapter 2 [*Phoenix et al.,* 2017] determined that the BMP that best simulated convective transport was the NSSL 2-moment BMP, that scheme was chosen for the remaining simulations. Additionally, although there was little sensitivity to the chosen PBL scheme and chemical mechanism, the YSU PBL scheme and RACM-ESRL chemical mechanism (chem_opt=108), where used. For domains with horizontal grid spacing greater than 4 km, the Grell convective parameterization was used. Otherwise, convection was explicitly resolved. Simulations were run with one-way nesting from a parent domain with a horizontal grid spacing of 12.5 km to intermediate and final nested domains having 2.5-km and 500-m spacings, respectively (Figure 33). Since the MCS covered much of the state of Kansas when the anvil wrapping feature was observed, the innermost nested domain was centered on Kansas, with the eastern boundary extending into central Missouri to capture transport around the anvil cloud.

The vertical grid consists of 136 levels with a nominal grid spacing of ~250 m in the free troposphere and stratosphere and a model top of 10 hPa (~30 km). A 5-km deep damping layer was employed to prevent reflection of spurious waves off the model top. Meteorological initial and boundary conditions were provided every 6 hours from the ERA-Interim reanalysis, which are available with a horizontal resolution of ~80 km and a vertical resolution ranging from 650 – 1000 m in the extratropical UTLS [*Dee et al.,* 2011].

The parent domain (Dx = 12.5 km) was simulated with WRF-Chem but with no chemical trace gas and aerosol processes. Next, the simulated meteorological fields were

downscaled to the intermediate domain (Dx = 2.5 km) and run with full chemistry. Both parent and intermediate domains were initialized at 1200 UTC on 30 May 2012 and run for 24 hours, with output being retained every hour. Due to the resolution of the innermost domain (Dx=500 m) and the size of the grid (2019x786x136), the simulation on this domain was not run for the full 24-hour period. The simulation on the 500-m domain was initialized at 2000 UTC on 30 May 2012, one hour before the earliest convective initiation was observed on the intermediate domain, and run until 0600 UTC on 31 May 2012 to allow the MCS to mature to the stage that was observed by aircraft observations during DC3. Output was retained every 5 minutes to capture small-scale (spatial and temporal) features including possible circulations arising from static and dynamic instabilities that could be responsible for anvil wrapping.

For the innermost domain simulation, it was determined that O_3 and CO would not change appreciably due to chemistry during the 10-hour simulation, especially since the 2000 UTC to 0600 UTC time period was during night. Thus, the simulation for the innermost domain did not have full chemistry but instead included two passive tracers, one with O_3 and the other with CO initial mixing ratios obtained from the intermediate domain simulation.

One sensitivity test was performed to diagnose the importance of cloud-radiative feedbacks (namelist option icloud) on mixing. The purpose of this sensitivity test was to determine if mixing at cloud top driven by radiative cooling plays an important role in the transport and mixing of air between the stratosphere and troposphere. Simulations with this feedback disabled were compared with a full-physics run for the innermost domain only. Column-maximum reflectivity fields from the WRF simulation without cloud-radiative feedbacks were not significantly different from the simulation with cloud-radiative feedbacks and will not be discussed here.

A passive tracer was configured to track the transport of air in the MCS. One passive tracer was defined to specifically track convectively influenced air as follows. The tracer was set equal to 1 in grid boxes where the total condensed cloud mixing ratio exceeded 0.1 g/kg and the column-maximum vertical velocity exceeded 2 m/s. If the criteria were not met, the tracer was initially set to 0. The tracer was re-initialized within convection at every time step.

3.3 Comparison with Observations

WRF-simulated reflectivity fields were evaluated using the GridRad dataset [*Bowman and Homeyer*, 2017]. The GridRad dataset consists of radar information from the U.S. NEXRAD WSR-88D radars merged onto a regular latitude-longitude-altitude grid at hourly analysis intervals. Figure 34 shows the column maximum reflectivity of the observed MCS and WRF-simulated MCS at 2-hour increments from 2200 UTC 30 May to 0200 UTC 31 May 2012. While the general E-W orientation of the convective cells is not well reproduced, WRF simulates the scale, organization, and timing of the MCS initiation and growth fairly well. It has also been shown that WRF under predicts anvil regions as a result of assumptions in the WRF-simulated reflectivity field [e.g., *Homeyer*, 2015; Chapter 2; *Phoenix et al*., 2017].

Radar analysis of the observed MCS indicated that overshooting convection within the MCS reached altitudes of ~3 km above the local tropopause. Since the vertical extent of the MCS may play an important role in determining the amount of STT, histograms of simulated 10 dBZ echo tops and cloud tops were compared to the observed GridRad composite 10-dBZ echo tops (Figure 35). Cloud tops are determined in WRF simulations as the highest altitude in a column where the total condensed cloud mixing ratio was at least 0.1 g kg^{-1}, which is the typical threshold value used for the visible cloud boundary. Frequency distributions of WRF simulated cloud top altitudes are insensitive to this threshold concentration (not shown). Although the vertical sampling from GridRad is coarser than WRF (1 km in GridRad compared to 250 m in WRF), it has been previously noted that this does not result in a significant difference [Chapter 2; *Phoenix et al*., 2017].

In comparing the simulated and observed 10 dBZ echo tops from 2200 UTC 30 to 0300 UTC 31 May 2012 (Fig. 35), WRF tends to over-predict echo top frequencies at lower altitudes (7-9 km) while under-simulating echo tops in the altitude range of 10-12 km. Additionally, the primary mode and mean simulated echo top is 1 km and 0.5 km lower, respectively, in WRF than in GridRad. Simulated cloud tops are generally higher in WRF than the observed 10 dBZ echo tops, as is expected due to the minimum detectable precipitation particle size of the NEXRAD WSR-88D radars. Though the full

vertical scale is not shown, the primary mode of the WRF-simulated cloud top altitudes is 14 km, with a mean altitude of 14.8 km.

In comparing the simulations with and without cloud-radiative feedbacks, there are some notable differences in the simulated echo tops. With cloud-radiative feedbacks enabled, there are generally a greater frequency of echo tops at lower altitudes (7-8 km) and a lower frequency of echo tops in the upper troposphere (10-11 km). Above 11 km, the frequencies of simulated echo tops are fairly consistent between the two simulations. The frequency distribution of cloud tops is consistent as well in the altitude range of 10-15 km. In general, there were few differences for cloud top height between the simulations with and without cloud-radiative feedbacks indicating turbulence generated by cloud radiative cooling is negligible. It will be shown later that anvil wrapping is unaffected by the small-scale static instabilities. Therefore, all results presented are for the simulation with cloud-radiative feedbacks, unless otherwise noted.

3.4 Evaluation of Mechanisms Influencing Anvil Wrapping

3.4.1 Overview of Simulated Anvil Wrapping

To show the simulated wrapping of high O_3 air around the storm anvil, we utilize vertical cross sections of O_3 and potential temperature. Figure 33 shows cross section transect used for all vertical cross sections. All cross sections use this same transect for four different times, 2030 UTC, 0000 UTC, 0200 UTC, and 0330 UTC. Figure 36 shows vertical cross sections of O_3 at these four times. Thirty minutes after the initiation of the inner model domain (Fig. 36a), the environmental LRT is at ~11 km, coinciding with an O_3 mixing ratio of about 150 ppb. Towards the eastern edge of the cross section, convection over Missouri is occurring, transporting low O_3 into the stratosphere. By 0000 UTC on May 31 (Fig. 36b), the MCS cloud tops extend several kilometers above the environmental LRT, perturbing the LRT and isentropes upward within the MCS. At this time, air containing O_3 in excess of 200 ppb has been transported downward into the upper troposphere along the trailing (upstream and opposite of storm motion) edge of the MCS. Along the downwind (right) side of the anvil, air is being mixed downward into the anvil and the cloud-free air ahead of its leading (right) edge. As the MCS continues to

mature, the narrow filament of high O_3 air along the trailing (left) edge of the anvil slowly recedes upward towards the stratosphere while the air ahead of the leading edge folds under and is mixed into the advancing anvil, producing the 'rams horn' shape (Figs. 36c, d) documented for observations of this case in *Pan et al*. [2014]. The mixing and transport of UTLS air into and around the MCS appears to be characterized by two phases: between 2300 UTC on May 30 (when the MCS first reaches the tropopause) and 0100 UTC on May 31, and after 0100 UTC on May 31. During the first period (2300 UTC – 0100 UTC), UTLS air is frequently transported downward to ~ 10 km in the leading anvil of the MCS (~2 km below the LRT). UTLS cloud-free air ahead of the MCS is transported downward, but not wrapped under the anvil. After 0100 UTC, UTLS cloud-free air is wrapped under the anvil. Since the simulation ended during active convection, an assessment of the irreversibility of transport cannot be performed. However, since it appears that O_3 contours do cross the potential temperature contours, it seems likely that some air was irreversibly transported.

To evaluate the hypothesized mechanisms contributing to the downward transport and wrapping of stratospheric air around the MCS anvil and into the troposphere, cross sections of vertical velocity, the storm-relative horizontal wind, and the vertical gradient of potential temperature are discussed in the next few subsections.

3.4.2 Storm-Scale Vertical Displacements During the MCS Initiation Phase

Figures 37a and 37b show the vertical velocity for the first several hours of MCS evolution. Initially, the strong vertical motions displace air vertically, such that some stratospheric air is displaced downward along the flanks of the MCS updraft as a result of compensating subsidence. Through this process, stratospheric concentrations of O_3 are brought down into the upper troposphere especially in and outside of the trailing anvil edge. As the MCS continues to mature (Figure 37c,d), air along both the forward and trailing anvils continues to move down within regions of weak descent.

To quantify the prevalence of these vertical motions in the MCS, timeseries of the maximum and minimum vertical velocity (representing maximum updraft and downdraft

velocities, respectively) and the updraft and downdraft areas were calculated in a ~2.5 km layer extending 2.5 km below the LRT to the LRT for the entire inner domain (Figure 38). The updraft and downdraft areas represent the number of columns in the UT layer where the vertical velocity was either larger than 3 ms^{-1} (updraft) or smaller than -3 ms^{-1} (downdraft). 3 ms^{-1} was determined to be the threshold for a convective updraft or downdraft based previous work. While the updraft and downdraft velocities increase steadily from 2100 to 0100 UTC, the updraft and downdraft areas increase sharply between 2230 and 2300 UTC, during the period when UTLS air was rapidly transported downward to the troposphere. After 0100 UTC, the updraft and downdraft areas continue to increase steadily while the maximum and minimum vertical velocities remain fairly consistent. This suggests that vertical motions associated with the MCS help to drive compensating downward transport of stratospheric air outside of the MCS, especially during the earlier stages of the MCS's lifecycle. However, since most of the air is wrapped under the anvil after 0100 UTC, this does not fully explain how the anvil wrapping process occurs.

3.4.3 Effects of Mesoscale Differential Advection in the Anvil

Coinciding with the growth of the updraft region in the MCS and upper-tropospheric subsidence along its sides, a divergent horizontal outflow occurs in the MCS anvil. The MCS and its anvil are embedded within a vertically-sheared background flow that contribute to their horizontal motions. On the forward (i.e., downshear) side of the MCS, the MCS outflow jet near the top of the anvil typically superposes on the background flow resulting in an even stronger jet than would occur in the absence of background flow. Beneath the strong jet, vertical shear is enhanced resulting in differential horizontal advection of conserved quantities (such as O_3). If the MCS steering level is located within this vertical shear layer, the differential advection could contribute to horizontal transport of these quantities at different levels occurring in opposite directions relative to storm motion. This process would lead to the so-called "wrapping" on the forward (downshear) side of the anvil, with rearward (i.e., upshear) storm-relative motion at levels within the weaker flow beneath the anvil. Wrapping associated with differential advection is less likely on the rearward (upshear) side of the anvil because the vertical

shear beneath the divergent MCS outflow on this side of the storm is more likely to be opposed by the background vertical shear, resulting in weaker differential advection.

Figure 39 shows cross sections of the storm-relative horizontal wind, which was calculated as the difference between the approximate storm motion of 21 ms^{-1} and horizontal component of the 3D wind along the path of the cross section, which is aligned with the storm motion vector. At initiation, there is a jet of positive storm-relative wind that appears in the center of the transect. As the MCS matures (Figure 39c,d), jets develop in both the forward (right) and rearward (left) directions of the vertical cross section, and are associated with horizontal divergence of air within the MCS as it reaches the LRT. The outflow jet in the upshear (left) side of the MCS and environmental flow likely maintain the folded filament of lower stratospheric air beneath the trailing anvil. Shortly after 0100 UTC (Figure 39c), a jet accelerates in the leading (right) edge of the anvil, while the storm-relative airflow beneath the jet is in the opposite direction (towards the center of the MCS), which facilitates the wrapping of UTLS air under the advancing anvil.

3.4.4 The Role of Small-Scale Static and Dynamic Instabilities

To assess the role of static and dynamic instabilities (e.g., gravity wave breaking, shearing instabilities) on the downward transport and wrapping of high O_3 air, cross sections of the vertical gradient of potential temperature were analyzed (Figure 40). During the early stages of the MCS's evolution (30 May 2300 UTC), the air around the MCS remains fairly stable (red shades; Fig. 40a). By 31 May 0030 UTC, weak instabilities, marked by near-zero and negative gradients in potential temperature, develop within the updraft and within the trailing anvil (Fig. 40b). Along the trailing anvil, O_3-rich air has been mixed down in a region of generally stable air. After 0200 UTC, instabilities form along the anvil edge in the upper troposphere (teal circles, Figs. 40c-d). By this time, however, the filaments of high O_3 air have already been wrapped around and under the advancing anvil. It is possible that the static instabilities generated from gravity wave breaking contribute somewhat to the irreversible transport process along the cloud edge, though it is uncertain how important they are in driving the wrapping process. This is further supported by cross sections of O_3 and the two-

dimensional horizontal component of the wind at 0000 UTC and 0300 UTC on the 2.5-km intermediate domain (Figure 41). Comparisons with the O_3 evolution on the innermost domain reveal that similar transport occurs on the 2.5-km domain as well. *Lane and Knievel* [2005] showed that simulations at O(1km) horizontal grid resolution under-predict gravity wave and turbulence spectra generated by convection. Therefore, since the MCS-relative horizontal wind structure and O_3 wrapping feature is comparable on the 2.5-km and 500-m domains, it suggests that small-scale instabilities are of little significance to anvil wrapping and that differential advection of air inside and outside of the anvil is the main contributor to the process.

To understand the role of cloud-top radiative cooling and mixing and the role of the resulting instabilities, a sensitivity simulation was run with cloud-top radiative mixing disabled. Figure 42 shows the vertical gradient of potential temperature for the simulation without cloud-radiative mixing effects. Without cloud-radiative mixing, the area of static instability ($\partial\theta/\partial z < 0$) identified in Figure 40 is greatly reduced in Figure 42. However, despite the absence of these instabilities, there is comparable wrapping. This result further suggests that static instabilities are an insignificant contributor to the wrapping phenomenon.

3.4.5 Synthesis of Mechanisms Responsible for Anvil Wrapping

WRF-Chem simulations of transported air around an observed MCS suggest that air is transported from the UTLS down into the troposphere by two main processes: 1) compensating vertical motions driven by mass continuity that transport air downward surrounding intensifying deep convection and 2) differential advection of outflow air in the leading anvil that results in horizontal transport in opposite directions relative to storm motion, with air in the weaker flow under the anvil advancing toward the center of the MCS. In the remaining sections we determine the net effect that MCS-induced transport has on UT O_3 mass and investigate the depth of the transported air and where the transported air originated.

3.5 Magnitude and Depth of Transported Air

3.5.1 Net Effect of MCS Transport on UT O_3

A timeseries of O_3 mass in the upper troposphere was calculated to analyze the net effect that this MCS had on upper troposphere O_3 (Figure 43). Figure 43a shows the timeseries of the rate change of the mass of O_3 that is in a layer extending 2.5 km below the LRT to the LRT. The O_3 mass flux (i.e., that transported into/out of the domain along the grid boundaries) was subtracted from the rate change of O_3 to give the net mass change of O_3, which is expected to be largely controlled by convective transport during the relatively short simulation period. Using the convective tracer described in section 3.2.2, the layer was separated into populations of air processed through convection (i.e., air in $w > 2$ m/s updrafts in cloud at some point during the simulation) and air outside of convection. Since wrapping generally occurs around the cloud anvil in cloud-free air (i.e., outside of the MCS), an increase in the O_3 mass in the non-convective air would indicate downward transport of high-O_3 air into the upper troposphere. However, since transport in the convective updraft will bring boundary layer air with lower O_3 mixing ratios to the UT, it is of interest to compare the competing effects between upward transport of boundary layer O_3 to downward transport of UTLS O_3 around the anvil. The O_3 mass in the convective and non-convective air was normalized by the number of representing grid points of either convective or non-convective area to account for the size of the storm (and number of convective/non-convective points) in a limited domain volume. Otherwise, as the MCS continues to develop, the total O_3 mass in the convective air would dominate the non-convective O_3 mass simply due to the increasingly larger area being identified as convective.

Between 2200 UTC and 0100 UTC, the net rate change (total rate change – horizontal flux) is negative due to convective transport of low O_3 to the upper troposphere from the boundary layer. Beginning at 0100 UTC, the net rate change becomes positive and increases for the remainder of the simulation. This transition occurs around the same time that O_3-rich air was wrapped under the leading anvil, as shown in Figure 38. Not surprisingly, in the non-convective air, the O_3 mass increases throughout the period while the O_3 mass in the convective air decreases during the first half of the

period, but begins increasing around 0230 UTC. The total O_3 mass in the layer decreases, which is partially due to horizontal flux of lower O_3 air into the domain and/or O_3-rich air out of the domain, but also due to vertical flux of lower O_3 air from the surface. Overall, this suggests that while an MCS does transport O_3-rich air downward into the troposphere, the net change in O_3 in the upper troposphere in and around an MCS may still be negative due to the large amounts of O_3-poor air being transported upward from the surface.

Over the simulation period, the mean UT O_3 increases by about 15 ppb over the 7 hour period (~2.14 ppb/hour) in the non-convective air but decreases by approximately 12.5 ppb during the period (1.79 ppb/hour) in the convective air (Fig. 43b). Combining both convective and non-convective air masses, the mean UT O_3 mixing ratio decreases by about 9 ppb over the 7 hours (1.29 ppb/hour). O_3 production in MCS outflow has been estimated to be approximately 2 ppb/hour during periods of active photochemistry [*Pickering et al*., 1990; *Apel et al.*, 2015]. The change in O_3 mixing ratios from transport of high O_3 in non-convective air estimated here is a similar magnitude as the change in O_3 from in situ photochemistry.

3.5.2 Origins of Transported Air

3.5.2.1 Backward Trajectory Calculations

To better understand where the wrapped air originates, backward trajectories were initialized within wrapped air along the leading and trailing anvil and calculated using Read/Interpolate/Plot (RIP, accessed at: http://www2.mmm.ucar.edu/wrf/users/download/get_sources_pproc_util.html). RIP calculates trajectories by linearly interpolating the trajectory's position based on the u, v, and w wind components. Trajectory calculations were based on a model output frequency of 5 minutes and a trajectory interpolation interval of 30 seconds.

Backward trajectories were initialized in the tongue of air wrapped under both the leading and trailing anvils at 0245 UTC on 31 May 2012 and run backwards until 2215 UTC on 30 May 2012 (Figure 44). Timeseries of the trajectory altitude show that the air wrapped under both the leading and trailing anvils originates from higher altitudes,

typically ~1 km above the initial altitude at 0300 UTC, though some air parcels originate ~1.5 km above the initial altitude (Figure 45). As suggested by the cross sections, transport along the leading anvil occurs as a gradual process over several hours while transport along the trailing anvil occurs more rapidly. Maps of back trajectories (not shown) show that the air wrapped under the leading anvil is mostly advected ahead of the MCS (i.e., same direction of storm motion) and is slowly transported down, eventually being overtaken by the more rapidly advancing anvil outflow. This supports the hypothesis that the transport is driven by compensating subsidence near the outer anvil with differential advection in the vertically sheared horizontal flow. As the MCS pushes up against the tropopause, lower stratospheric air is displaced outward and downward towards the anvil edge, where it is further transported and mixed downward and below the advancing anvil due to differential advection (faster horizontal motion of anvil air than the air directly beneath it). Backward trajectories initiated in the trailing anvil exit through the northern domain boundary between 0015-0045 UTC. This air is drawn in towards the MCS rapidly and is quickly transported downward. It is likely that this transport is mainly due to obstacle-like flow [e.g., *Long*, 1970; *Brighton*, 1973] due to competition between the strong UT jet and opposing MCS outflow (Fig. 39). In this scenario, the MCS outflow and tropopause act as an obstacle and rigid upper boundary, respectively, to the environmental flow, forcing the air to descend. This air preferentially moves downward into the upper troposphere, where the stability is lower.

3.5.2.2 Forward Trajectory Calculations

To better understand the starting altitude of the transported air, RIP was also used to calculate forward trajectories. Figure 46 shows locations of several trajectories that were initialized in the same area but at varying altitudes between 10.5 km and 12 km (in the UTLS, as the LRT was approximately 11.25 km at this time). Forward trajectories were initialized ahead of the MCS during the early stages of convective initiation (2120 UTC) and run until sufficient wrapping had occurred (0300 UTC). For those trajectories initialized at 11.5 km and higher (e.g., T3 and T4 in Figure 46), the air parcels remain at approximately the same height for the duration of the trajectory's path. Those trajectories initialized at 11 km and lower (e.g., T1 and T2 in Figure 46) descended downward by

more than 2 km. Additionally, for those trajectories that descend into the troposphere, the highest initial O_3 mixing ratio among those trajectories is about 150 ppb. Therefore, while air is being wrapped around the thunderstorm's anvil, the high O_3 air transported downward in the WRF simulation is mainly upper tropospheric and tropopause transition layer air, with very little air from the stratosphere.

3.5.3 Discrepancies Between Modeled and Observed Ozone

Since *Pan et al*. [2014] observed O_3 mixing ratios in excess of 200 ppb within the wrapped air, it is useful to determine whether WRF-Chem is either not accurately representing the initial O_3 profile or not fully capturing the transport process. To evaluate the role of storm dynamics, the level of maximum detrainment (LMD; where the peak in MCS outflow is observed) associated with the MCS was calculated in WRF and from NEXRAD. Since the anvil wrapping transport process seems to be partially driven by differential advection related to outflow in the thunderstorm anvil, differences in the LMD relative to the LRT between that simulated and observed may explain the discrepancy in transported O_3. However, in both WRF and the observed MCS, the LMD was approximately 9 km, suggesting that storm dynamics were broadly well represented in WRF.

Since the tropopause transition layer is marked by sharp gradients in O_3, slight misrepresentations of the modeled background O_3 state could result in biases in the O_3 transport predicted by the model. As noted, the DIAL lidar on board the DC8 observed O_3 concentrations higher than 200 ppb while simulated O_3 transport was at most 150 ppb. Comparisons of modeled O_3 at 0200 UTC 31 May (Fig. 36) to Figure 2 of *Pan et al.* [2014], suggest that the simulated stratospheric O_3 in WRF was actually higher than observations in the upper troposphere and lower stratosphere (~9-15 km). Therefore, the lower O_3 in the wrapped air in WRF is likely due to an underrepresentation of the downward transport of stratospheric air.

Additionally, vertical resolution in the UTLS can be an important source of uncertainty in simulations of the depth and amount of cross-tropopause mass transport [*Homeyer*, 2015]. For a given horizontal resolution, the amount of mass transported downward from the stratosphere to the troposphere as well as the depth of transport

increases with increasing vertical resolution. While this does not explain why very little stratospheric air was transported into the troposphere, it does suggest that the vertical grid spacing may be partially responsible for the limited amount of cross-tropopause transport. Still, it is likely that there are some features of this transport mechanism, specifically one that drives abundant transport across the tropopause, that are not adequately simulated by the model. It is also possible that other elements of the model design (e.g., PBL parameterization or cloud physics), though modeled after successful tropopause-overshooting simulations, were not ideal for simulating the wrapping process. The sensitivity of simulated wrapping to physical and chemical parameterization is not entirely known.

3.6 Conclusions and Future Work

Previous modeling and observational studies have shown that convectively-driven STT of O_3 around the anvil of an MCS is possible. However, the mechanism(s) that drive this transport process are not well understood. Several mechanisms influencing this transport, including dynamic instabilities and MCS-induced mesoscale circulations, were evaluated here using high-resolution simulations from WRF-Chem. This work indicates that the main contributors to this process are i) the intense convective motions and mass conservation that drive the initial downwelling of air outside of the anvil, and ii) differential advection between outflow air and air outside of the cloud that create an eddy circulation near the anvil edge, leading to wrapping of air down and under the anvil cloud. Trajectory calculations indicate that the wrapped air in WRF simulations was mainly tropopause transition layer air, with air originating above the LRT remaining in the stratosphere. Simulated O_3 in the wrapping feature was lower than observations. Since the initial modeled O_3 was actually higher in the UTLS compared to observations, this suggests that the model did not fully simulate the transport process.

Since the model does not completely simulate STT, future model simulations should be performed to test the sensitivity of cross-tropopause transport to vertical resolution in the UTLS and other model design choices. STT simulated on the 2.5 km horizontal grid and 500 m horizontal grid was comparable, suggesting that this type of transport is not sensitive to horizontal resolution. However, as suggested by *Homeyer*

[2015], stratosphere-troposphere exchange may be more sensitive to the vertical resolution of the model. Due to computational limitations, the primary model simulation used in the analysis (i.e., the 500-m domain) was not run with full chemistry, but with passive tracers initialized to the O_3 and CO fields from the 2.5-km domain simulation. While the chemistry responsible for the production and loss of O_3 is expected to be minimal during the simulation period (2100 – 0600 UTC, mainly after sunset), a longer simulation with full chemistry could be used to evaluate the long-term impact of the MCS on the O_3 composition of the UTLS. Future work should aim to better understand how an MCS affects upper tropospheric O_3 several hours to days after an event, and attempt to address the irreversibility of this transport process. Additionally, future studies should address how often STT occurs on a seasonal scale and whether this process is unique to MCSs.

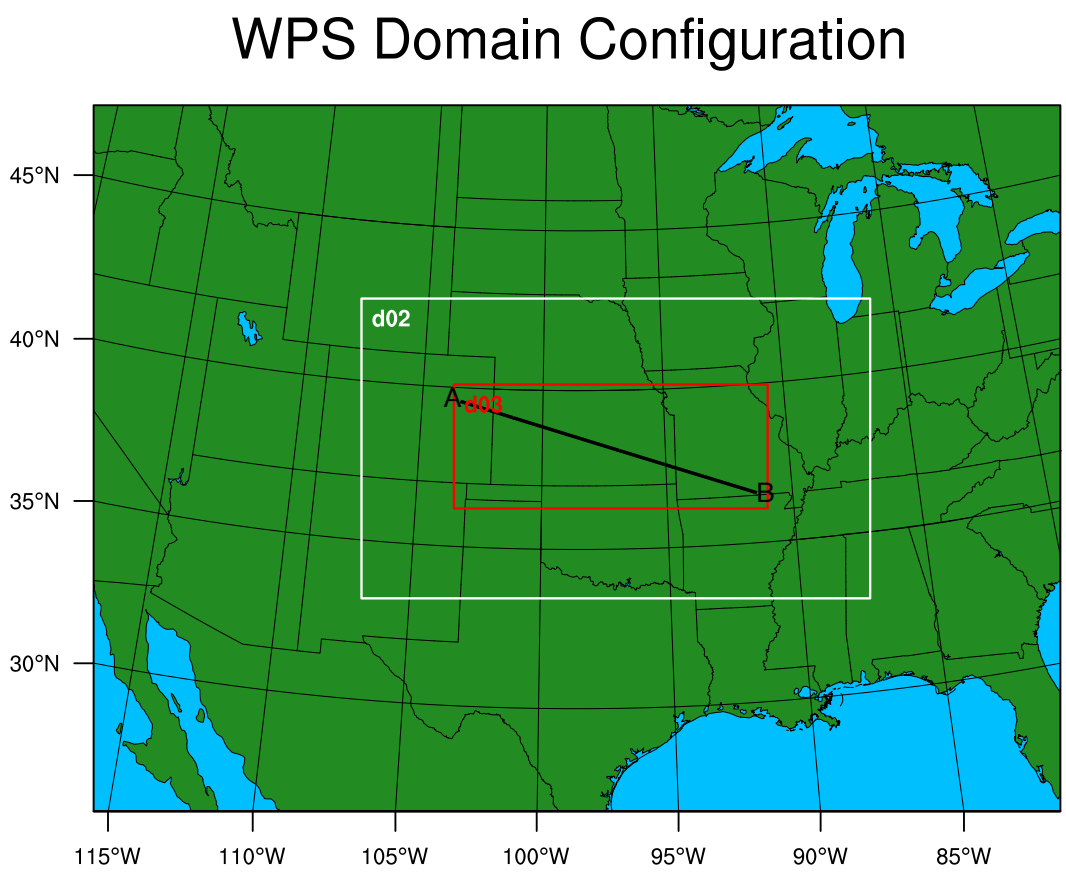

Figure 33. WRF model domain configuration. The transect line used in subsequent vertical cross sections is shown from point 'A' to point 'B.' Note that the transect is the same for all times.

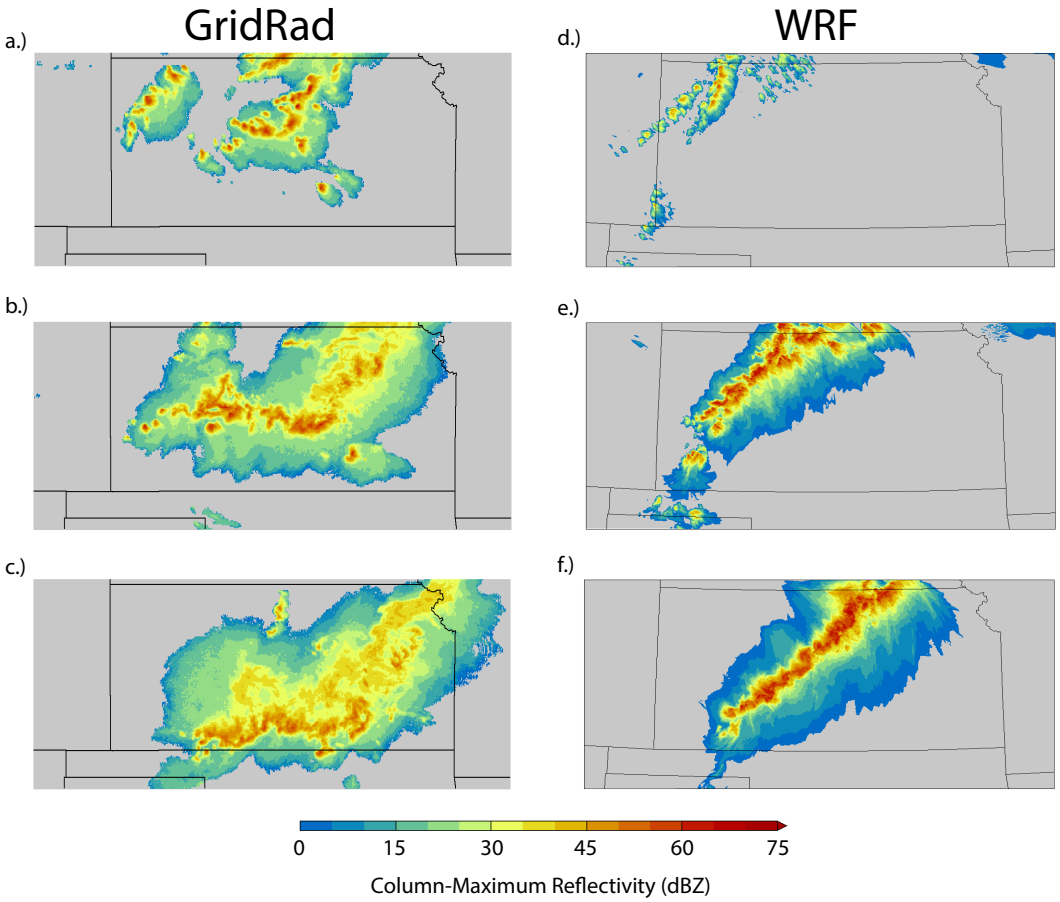

Figure 34. Comparison of column-maximum reflectivity in GridRad (left) and WRF (right) for three times: 2200 UTC (top), 0000 UTC (middle), and 0200 UTC (bottom).

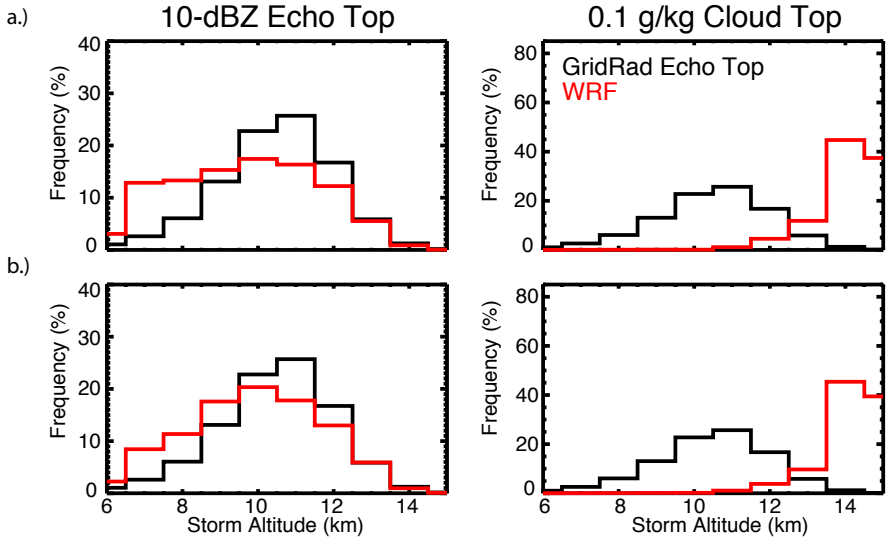

Figure 35. Histograms of WRF simulated 10 dBZ echo tops (left column, red line) and cloud tops (right column, red line) and GridRad 10 dBZ echo tops (black lines). WRF simulations with cloud-radiative feedbacks turned on are shown in a.).

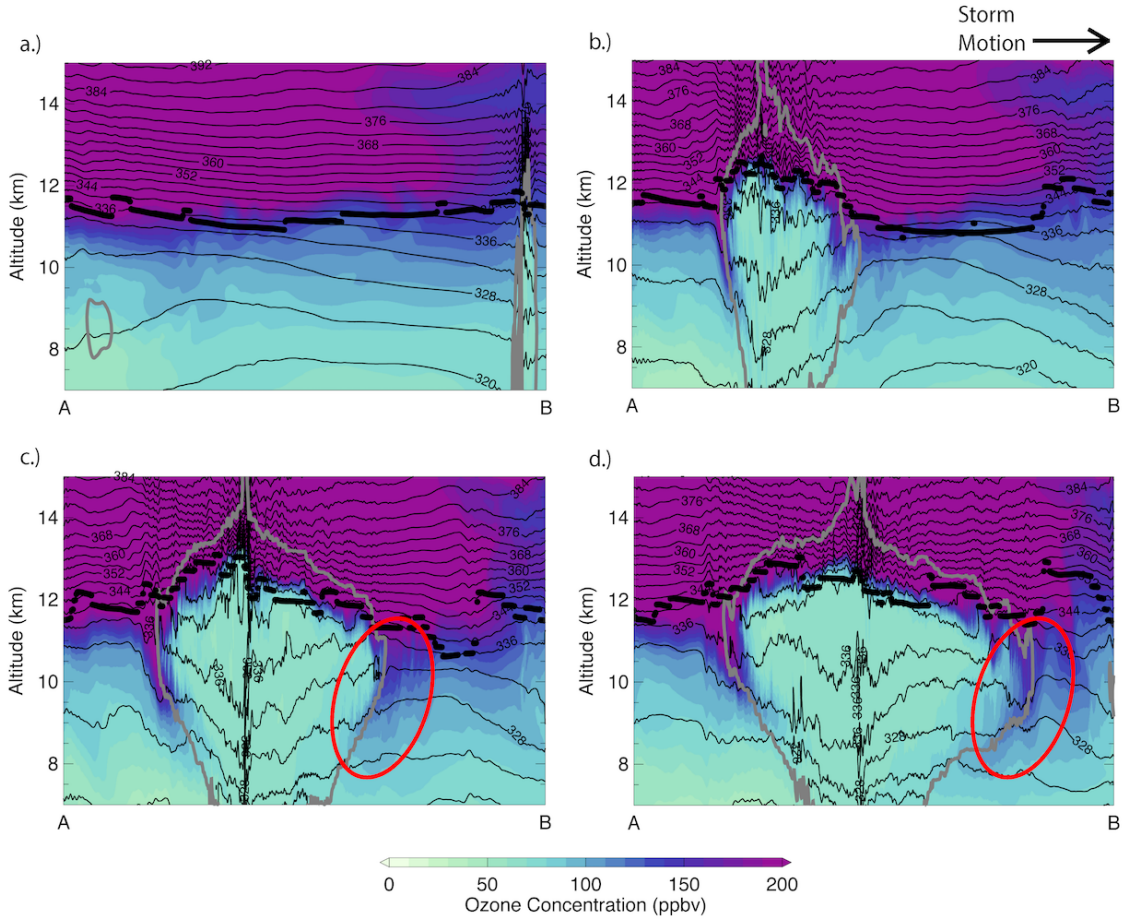

Figure 36. Vertical cross sections of simulated ozone (color fill) and potential temperature (thin black lines) at four times along the transect line shown in Figure 33: 2030 UTC (a), 0000 UTC (b), 0200 UTC (c), and 0330 UTC (d). The cloud boundary is shown in gray and the LRT is shown as the black dots. The red circle shows the location of the 'Ram's horn' feature described in *Pan et al.,* [2014].

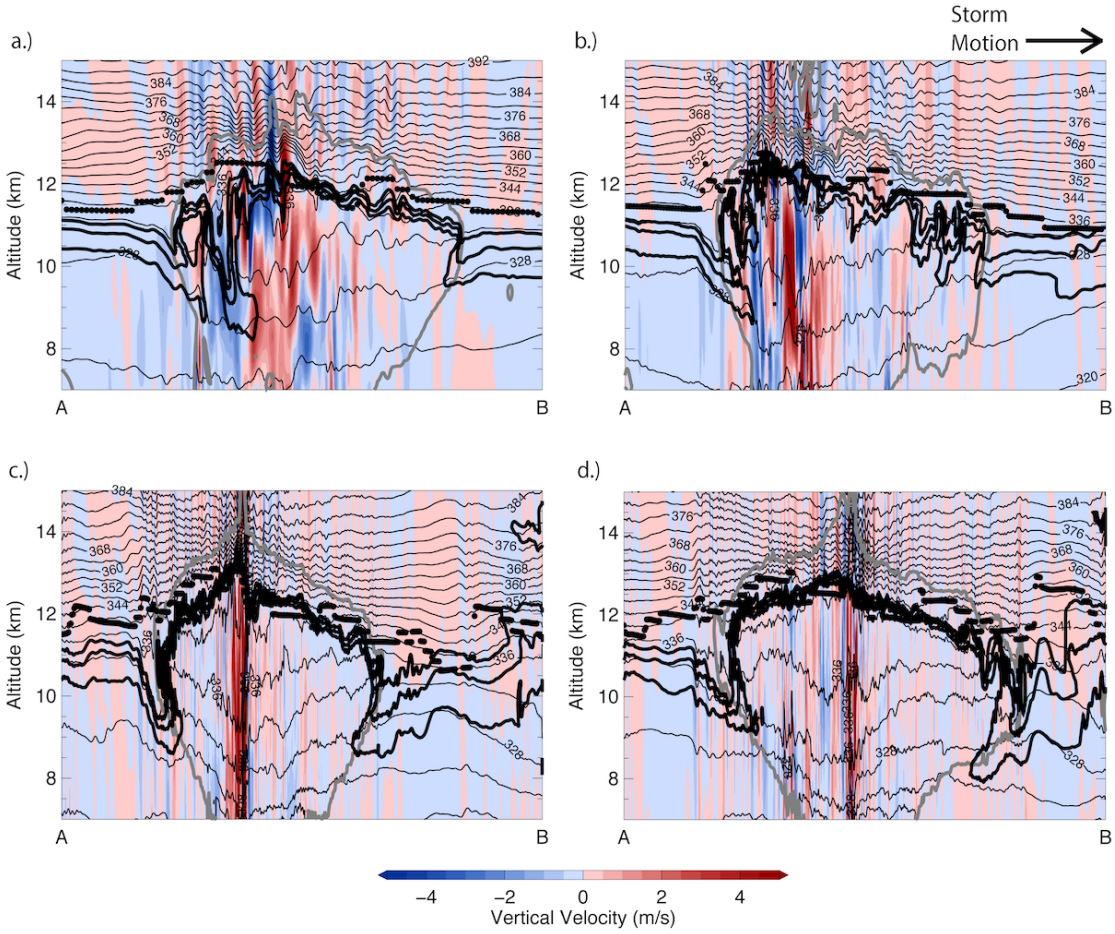

Figure 37. As in Figure 36, but with vertical velocity color filled and for times 2300 UTC (a), 2330 UTC (b), 0200 UTC (c), and 0330 UTC (d). Note that we have zoomed in on the storm for 2300 UTC and 2330 UTC to clearly show the vigorous vertical motions.

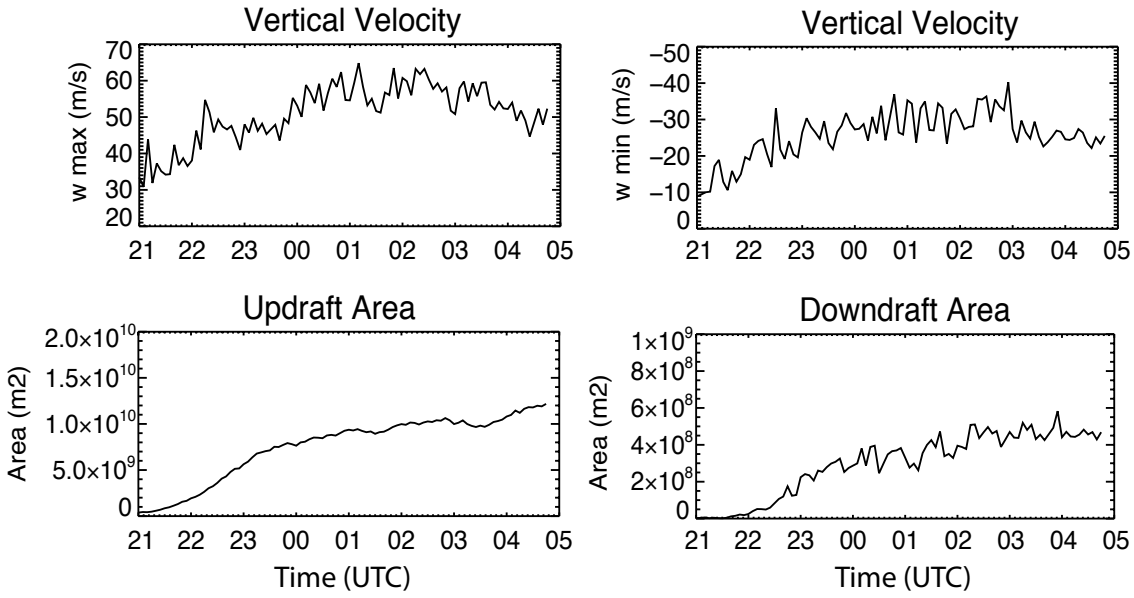

Figure 38. Timeseries of (a) maximum and (b) minimum vertical velocity (top) and (c) updraft and (d) downdraft prevalence (bottom). Updraft and downdraft prevalence is the area of points in the domain where the vertical velocity is greater than 3 m/s and less than -3 m/s, respectively.

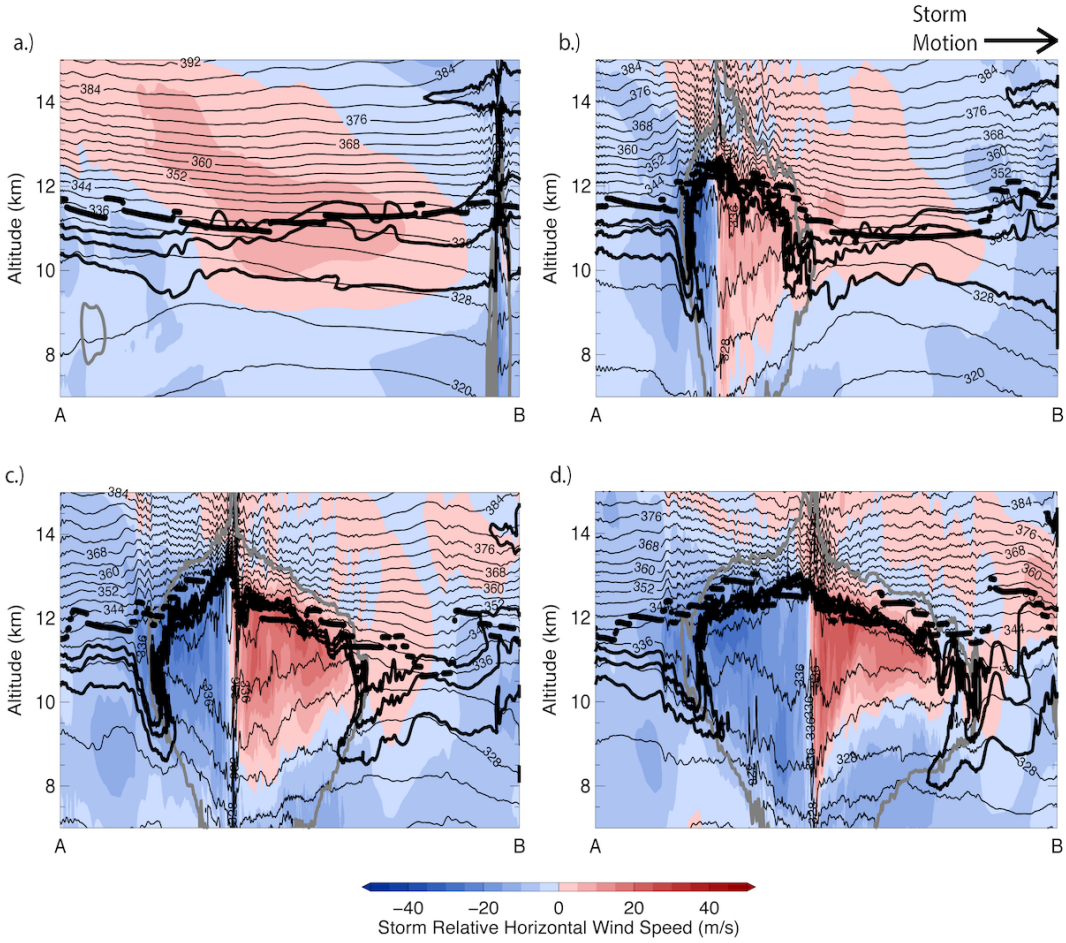

Figure 39. As in Fig. 36, but with the storm-relative horizontal wind speed color filled. The ozone concentrations at 100 ppb, 125 ppb, and 150 ppb is contoured with the solid black lines.

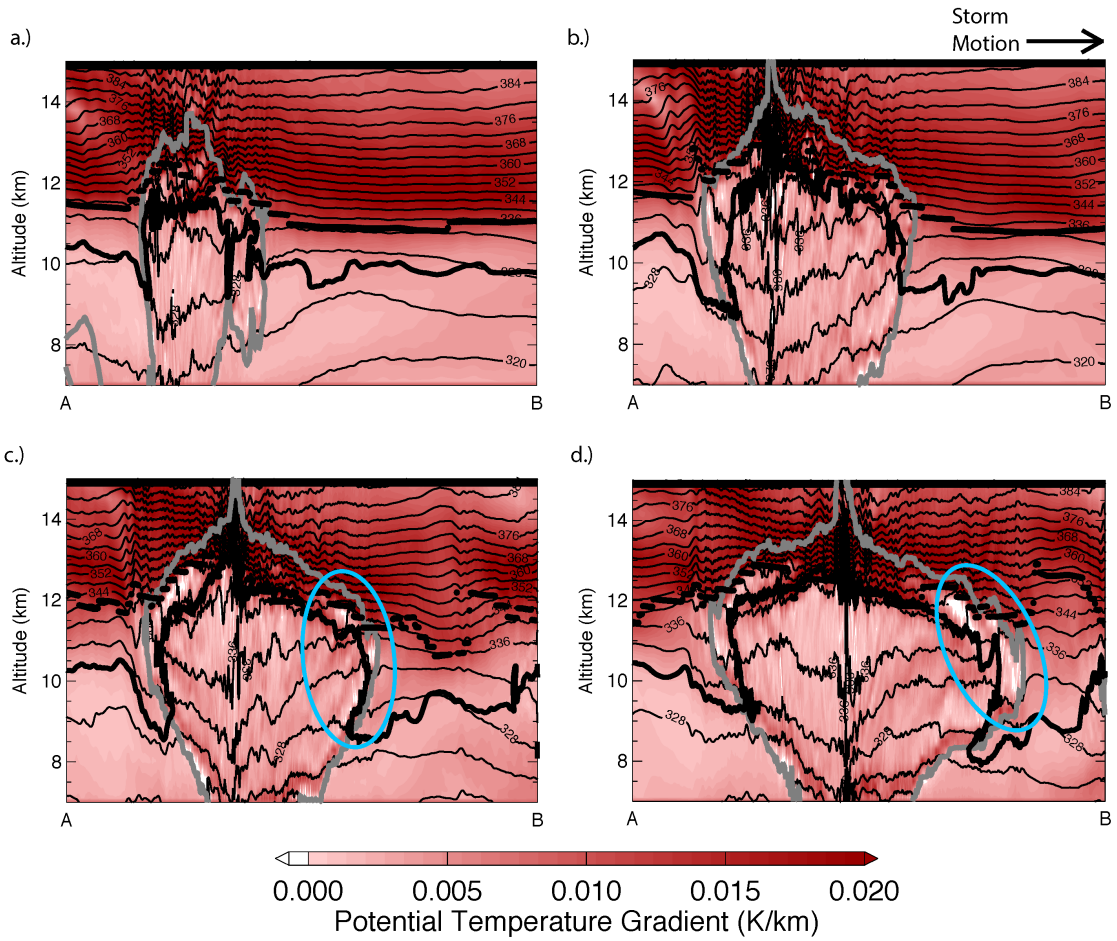

Figure 40. As in Figure 36, but with the vertical gradient of potential temperature color filled and for times 2300 UTC (a), 0030 UTC (b), 0200 UTC (c), and 0330 UTC (d). Note that the ozone concentration at only 100 ppb is contoured so that the instabilities arising near the cloud boundary (indicated by the light blue circles) are more easily distinguishable.

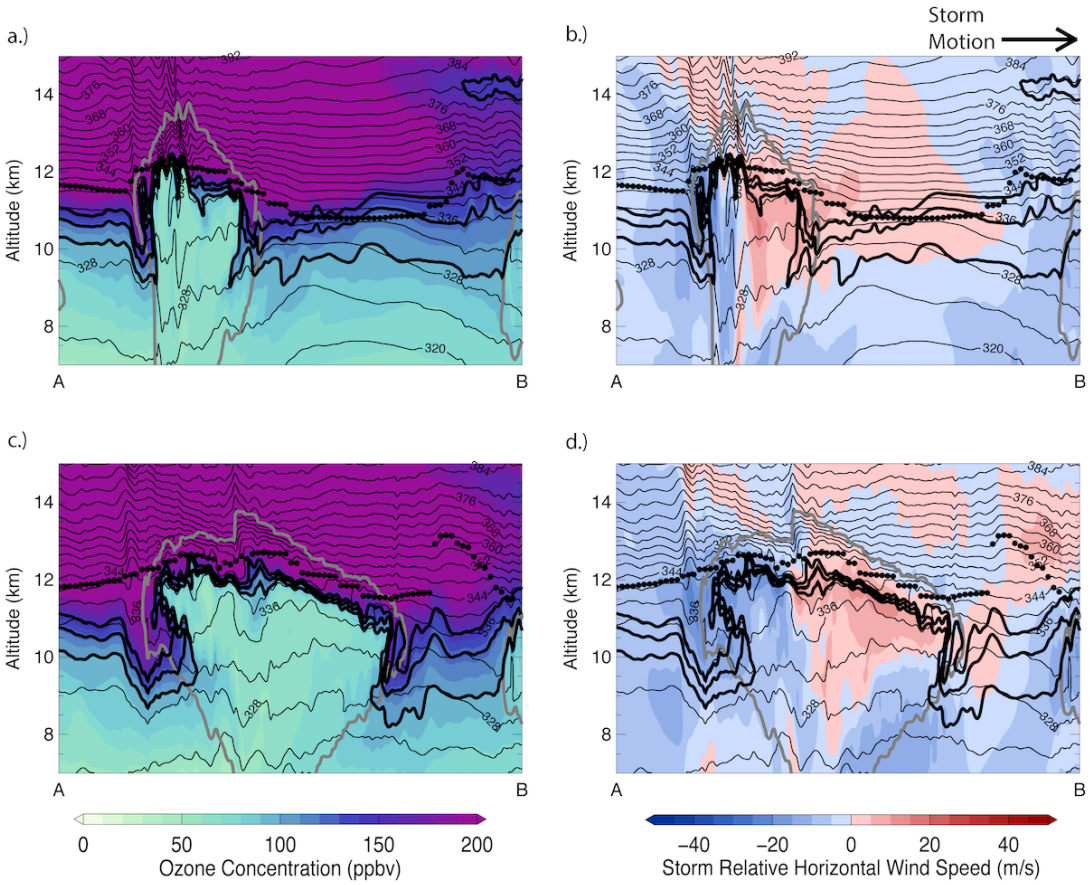

Figure 41. Vertical cross sections of ozone (color fill, left column) and the storm relative horizontal wind speed (color fill, right column) on the intermediate domain (2.5-km) for two times: 0000 UTC (top row) and 0300 UTC (bottom row). The potential temperature is contoured with thin black lines and the ozone concentration at 100 ppb, 125 ppb, and 150 ppb is contoured with solid black lines. The cloud boundary is shown with the gray solid line and the LRT is shown with the black dots. The transect of the vertical cross section is approximately the same as in Figure 33.

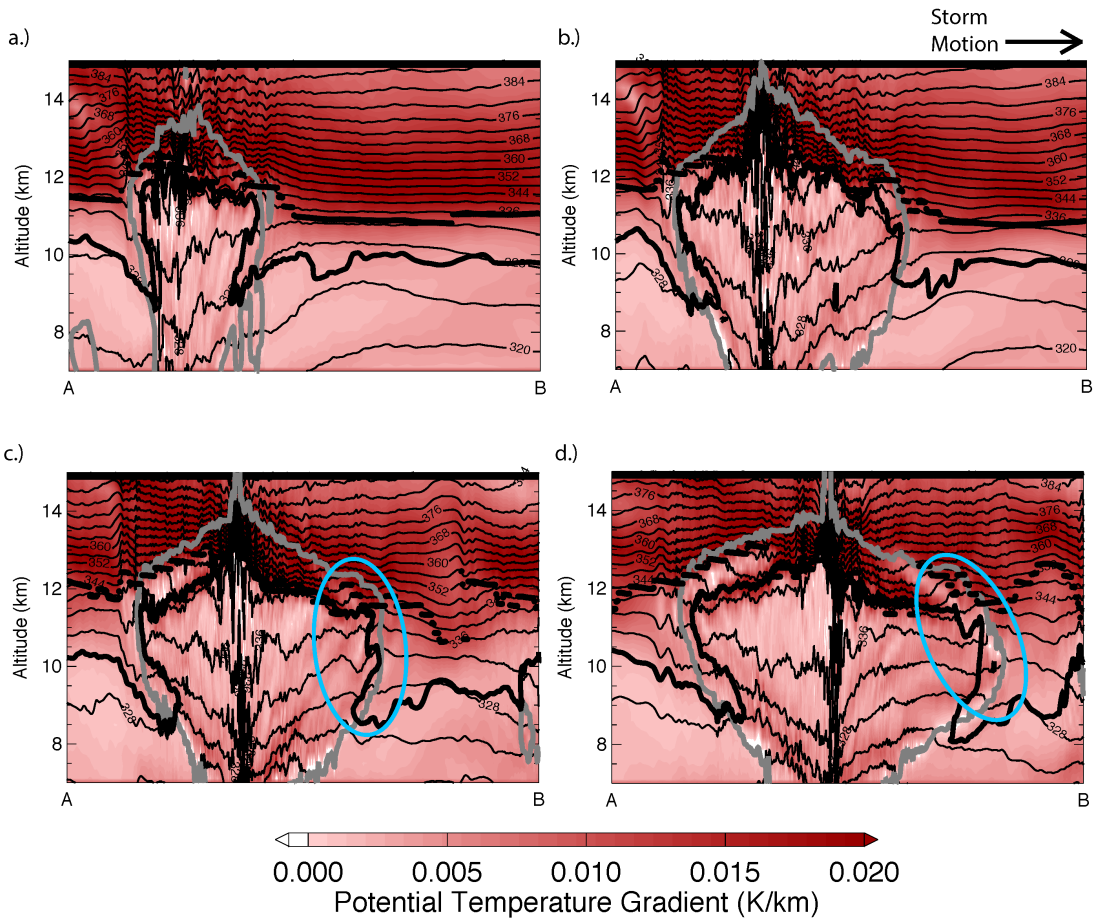

Figure 42. As in Figure 40, but for the simulation with cloud-radiative feedbacks turned off. The light blue circles highlight the differences in the prominence of instabilities between this simulation and the simulation with cloud-radiative feedbacks turned on.

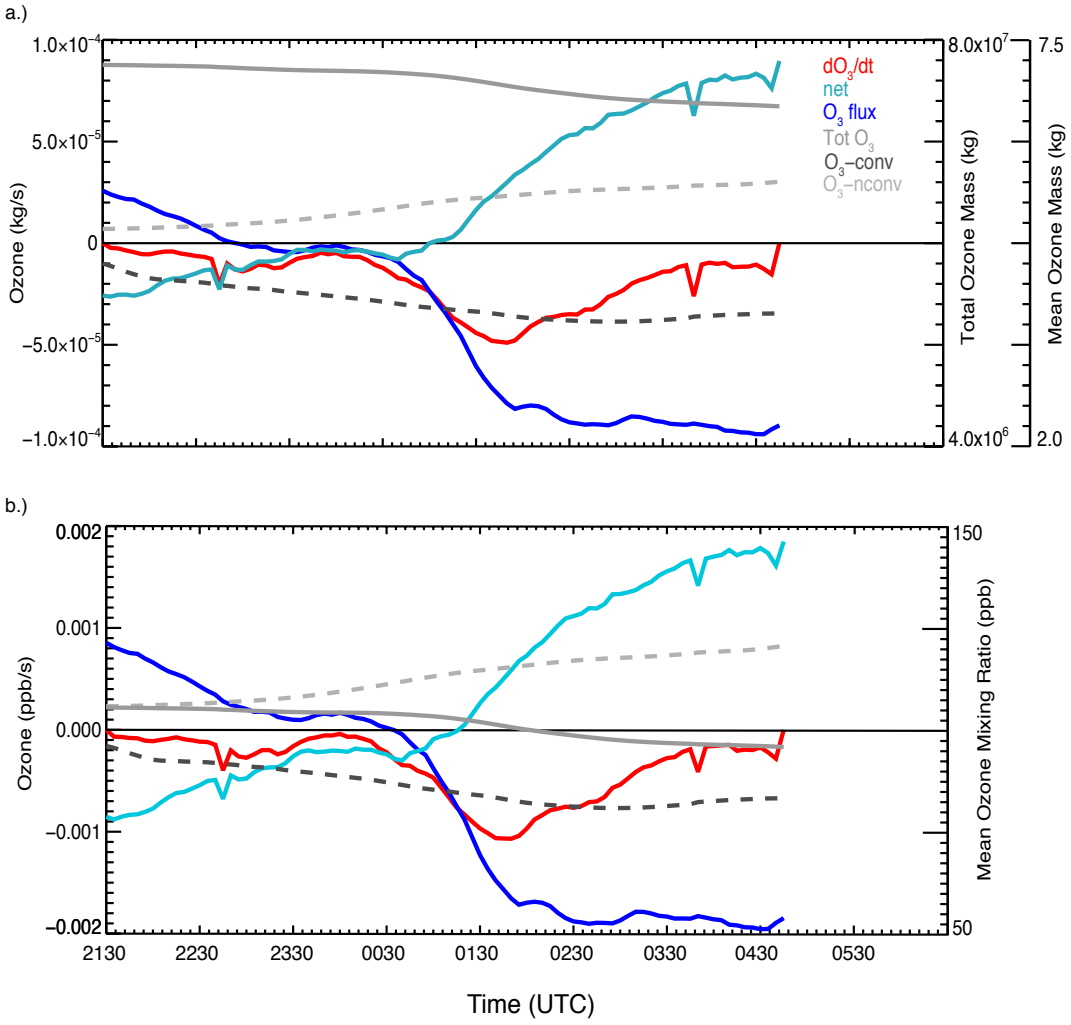

Figure 43. Timeseries of ozone mass (a) and ozone mixing ratio (b) in a 2.5 km layer in the upper troposphere (~8.5 km – 11 km). The instantaneous rate change of ozone mass/mixing ratio (red line, dO_3/dt), the horizontal flux of ozone mass/mixing ratio in and out of the domain (blue line, O_3 flux), and the difference between the rate change and horizontal flux (cyan line, net) are shown with the left vertical axis. The total change in ozone mass in the layer (Tot O_3, solid gray) is shown with the right vertical axis in a.) labeled "Total Ozone Mass (kg)." The ozone mass within convective air (O_3-conv, dashed dark gray) and the ozone mass within non-convective air (O_3-nconv, dashed light gray) are shown with the right vertical axis in a.) labeled "Mean Ozone Mass (kg)." The layer mean, convective, and non-convective ozone mixing ratios are shown on the right vertical axis in b.) in the solid gray, dashed dark gray, and dashed light gray lines, respectively.

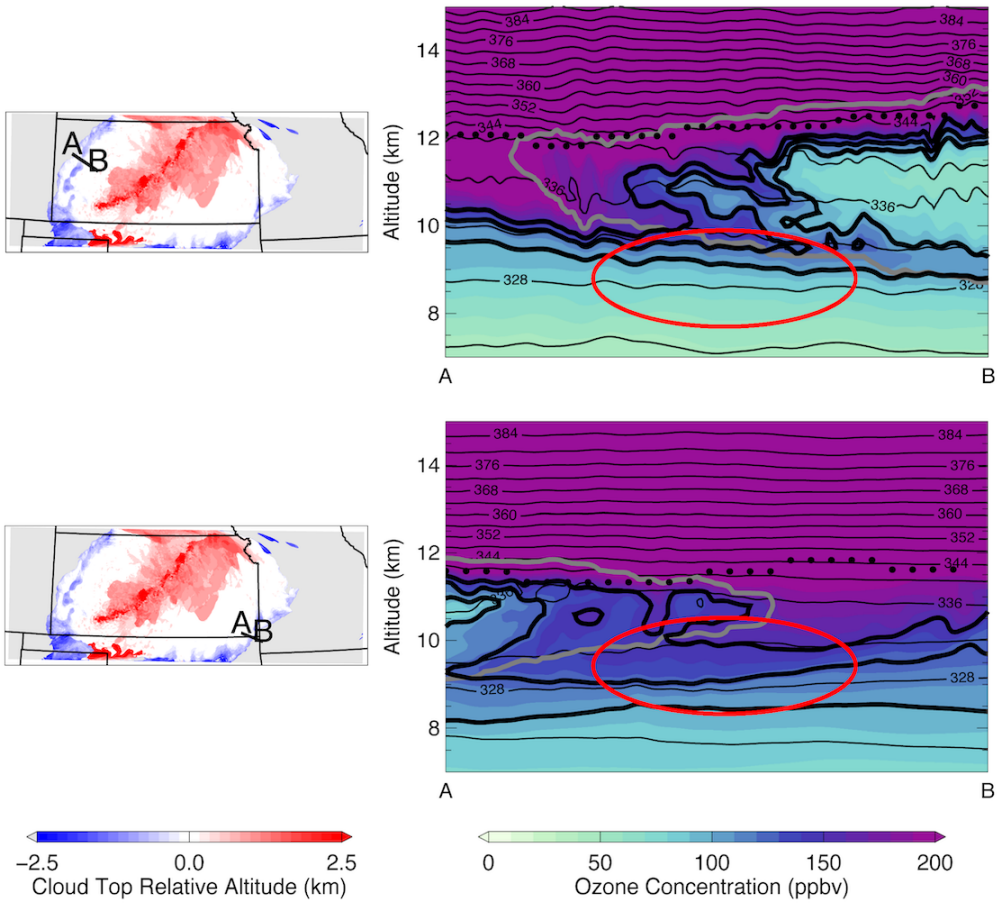

Figure 44. Vertical cross sections of ozone (color filled), potential temperature (thin black lines), cloud boundary (solid gray line), the tropopause (black dots) showing locations of initialized backward trajectories in the trailing (top) and leading (bottom) anvils (red circles). The start and end points of the vertical cross section are shown on the map of cloud-top relative altitude (left column).

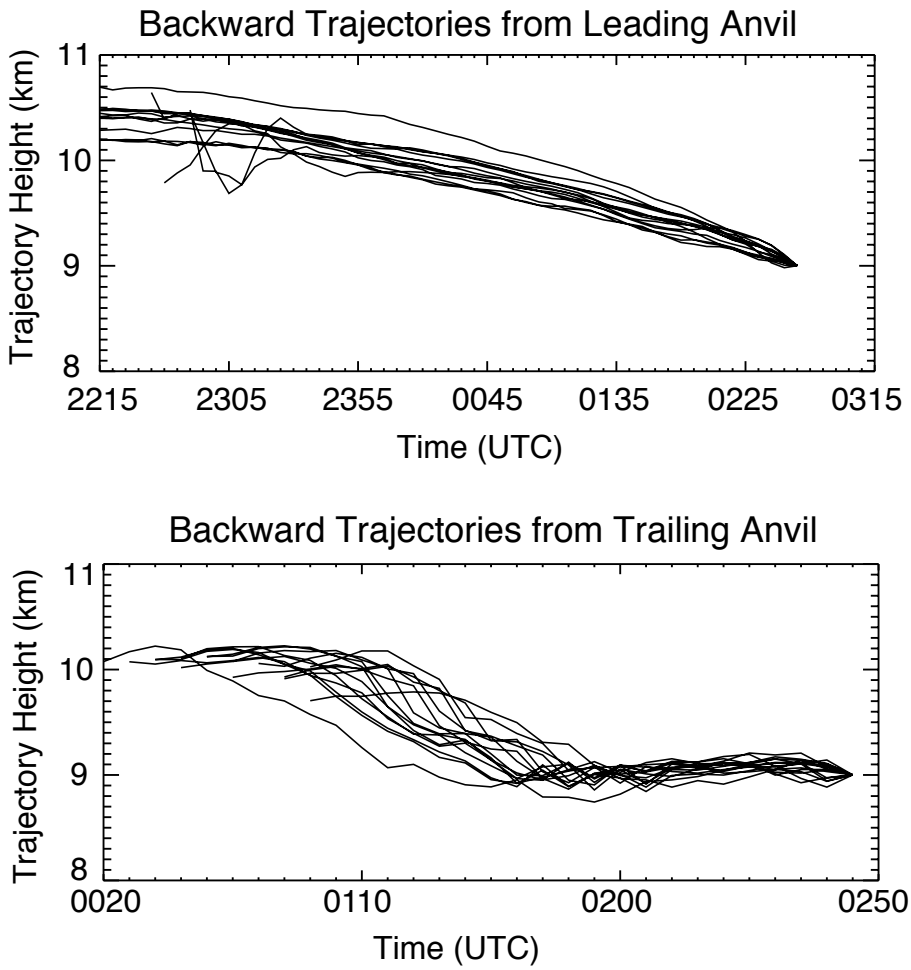

Figure 45. Timeseries of the height of backward trajectories initialized in wrapped air along the leading (top) and trailing (bottom) anvils.

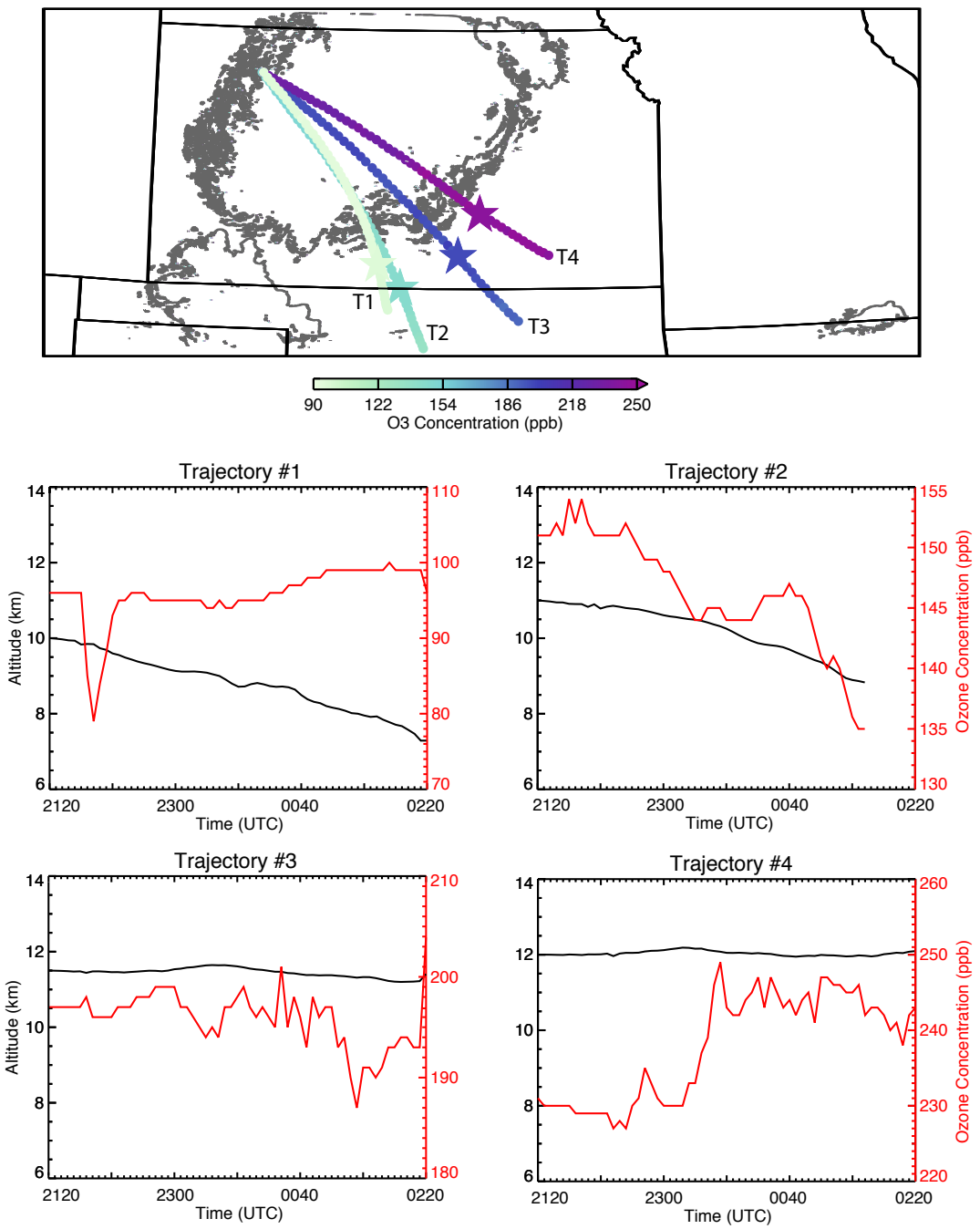

Figure 46. Map of forward trajectory locations initialized in clear air ahead of the MCS at 2120 UTC. Trajectories are colored by their corresponding ozone concentration. A timeseries of each trajectory's height and ozone concentration are shown below.

Chapter 4

Broad Impacts of Convection on the Upper Troposphere and Lower Stratosphere in Two 10-Day Simulations

Studies of convection-driven STE have only recently become the topic of observational and modeling studies, our current understanding of the impacts of overshooting convection on UTLS composition is limited. While it is currently well known that TST and STT are both possible, it is not entirely known how often STE occurs, the depth and magnitude of chemical impact, the mechanisms responsible for irreversible transport, and the response of overshooting convection to a changing climate. Since satellite and aircraft observations can be limited in space and time and in situ chemical observations are rare, numerical model simulations are needed to better understand the effects of extratropical convection. In this study, a set of two 10-day model simulations are analyzed to understand the effect of extratropical convection on the chemical composition of the UTLS over the United States. Two main compositional changes of interest are: upward transport and injection of H_2O into the lower stratosphere and downward transport of O_3 into the upper troposphere. This chapter will address several research questions to improve our understanding, including:

- What is the impact of convection on UTLS composition?
- How does it vary depending on storm and environment characteristics?
- How does the impact vary depending on season?

4.1 Model Setup and Design

Version 3.7.1 of the Weather Research and Forecasting model [*Skamarock et al.,* 2008] coupled with Chemistry [*Grell et al.,* 2005; *Fast el al.,* 2006] was used for this study. The model configuration is the same as that described in Chapters 2 and 3 unless otherwise noted here. Simulations were first performed for the parent domain (Dx = 15 km) and

then downscaled to the nested domain (Dx = 3 km) (Figure 47). Both parent and nested domains were initialized at 1200 UTC on 18 May 2011 and 05 August 2013 and run for 240 hours, with output being retained every hour. While longer simulation periods were desired, computational limitations restricted then length of the simulated periods. A passive tracer package was configured to track the transport of air in and around convection. One passive tracer was defined to specifically track convectively influenced air as follows. The tracer was set equal to 1 in grid boxes where the total condensed cloud mixing ratio exceeded 0.1 g kg^{-1} and the column-maximum vertical velocity exceeded 2 m s^{-1}. If the criteria were not met, the tracer was initially set to 0. The tracer was re-initialized within convection at every timestep. Since convection is active throughout the simulation period, the first 12 hours were discarded from the analysis to allow for model spinup.

4.2 Model Evaluation

Two periods were selected to evaluate the impact that convection has UTLS composition: 18-27 May 2011 and 5-15 August 2013. These periods were selected because they were identified as periods with a high frequency of overshooting convection [*Cooney et al*., 2018] and to contrast the effects of springtime and summertime convection. Both environments have discrete, multi-cellular, and supercell convection. The May 2011 period appears to have more MCSs while August 2013 has more discrete convection, especially in the SE US. Another key difference between the two periods is the height of the tropopause. In May, the tropopause is generally lower (11-13 km) while in August, the tropopause break shifts north such that much of the domain is south of the break (i.e., the tropopause is ~15 km for much of the domain).

WRF-simulated reflectivity fields were evaluated using the GridRad dataset [*Bowman and Homeyer*, 2017]. The GridRad dataset consists of radar information from the U.S. NEXRAD WSR-88D radars merged onto a regular latitude-longitude-altitude grid at hourly analysis intervals. Figure 48 compares counts of overshooting convection in each gridbox from 0000 UTC on 19 May 2011 and 1200 UTC on 27 May 2011 in WRF and GridRad. An overshoot is defined as the maximum altitude of the 10-dBZ echo top altitude at least 500-m above the LRT in GridRad. As noted in Chapter 2, WRF echo

top altitudes are typically underestimated, therefore the altitude criterion was relaxed to 500-m below the tropopause for WRF. During this period, there were many storms that overshot the tropopause in Oklahoma, Kansas, Missouri, and Arkansas. Additionally, there were several storms in the Midwest and along the east coast that overshot the tropopause. WRF generally matches the area of the highest frequency of overshooting convection during this period. However, WRF does not have many storms in western Oklahoma or central Kansas that overshoot the tropopause. Some storm locations in WRF appear to be displaced to a neighboring state; for example, the stimulated storms in Iowa appear to correspond with the storms in Kansas and the simulated storms in Illinois appear to correspond to the storms in Indiana. WRF also has fewer occurrences of overshooting convection in the southeastern United States and along the east coast, especially in Pennsylvania and North Carolina. Overall, WRF adequately simulates overshooting convection during this period. Figure 49 compares column-maximum reflectivity between GridRad and WRF for three times. In general, WRF is accurate in simulating the orientation and organization of convection, as well as the timing and location.

In August, the majority of overshooting storms during the 0000 UTC 6 August 2013 – 1200 UTC 15 August 2013 period were in Kansas and Oklahoma, with a secondary peak in the southeastern United States (Figure 50). However, WRF has difficulties in simulating the observed organization, timing, and location of these storms. In general, the simulated storms are more spread out across the eastern half of the United States. The model simulates few overshooting storms in Kansas and Oklahoma and a relatively large number of storms in the Midwest, where in reality there were no overshooting storms. Investigation into the individual cases reveals that storms were typically stronger than in reality in WRF in some cases, or simulates convection that was not observed in other cases (Figure 51). Large scale analysis suggests that many of the storms in August were weakly forced (not shown), which proved difficult to accurately simulate in the model. Other studies have noted difficulties in simulating summertime convection [e.g., *Sun et al.,* 2016]. Additionally, the strongest tropopause-penetrating storms occurred at night, which has been a challenge for numerical weather prediction models to adequately simulate [e.g., *Geerts et al.,* 2017].

To gain an understanding of how the timing of these convective systems compared, timeseries of overshooting fractions were calculated for GridRad and WRF (Figure 52). The overshooting fraction was defined to be the fractional area of the WRF domain that had reflectivity of at least 5 dBZ at or above the LRT. To compare with observations, GridRad reflectivity fields were first interpolated to the nested WRF domain and then the convective fraction was calculated.

For May, the timing of the convective pulses are generally in good agreement between WRF and GridRad. Although the convective fractions are typically higher in GridRad, the main focus of this analysis is to determine if the timing of the storms is in agreement. Only a few events appear to be 'missed' by the WRF simulation and there is very good agreement for the big convective events during the second half of the WRF simulation period. For August, there are a comparable number of convective events throughout the simulation period, but as determined by the overshoot maps, the storms were not accurately simulated. Still, this indicates that while the locations may not be comparable, there were still a similar number of storms reaching the tropopause.

4.2.1 Tropopause Height and UTLS O_3 Evaluation

Ozonesondes from the SouthEast American Consortium for Intensive Ozonesonde Network Study (SEACIONS; *Thompson et al.*, 2016) were used to evaluate the model representation of the LRT and O_3 field. SEACIONS ozonesondes are available for the summer of 2013 from several locations: Boulder, CO, St. Louis, MO, Huntsville, AL, Idabel, OK, Soccoro, NM, and Tallahassee, FL. Ozonesondes were not available to evaluate the model performance for the May 2011 period, but since the convective systems quickly move out of the domain in May, the chemistry resulting from convective outflow is less likely to play a role in the UTLS composition within the model domain. During August 2013, the North American Monsoon is centered in the southeastern United States and will trap and circulate convective outflow for several days, increasing the likelihood that the UTLS composition will be affected by convection.

Figure 53 shows the WRF simulated LRT and O_3 model bias for several available times. In general, the WRF simulated LRT at each location is within ~1 km of the observed LRT, and often within 300 m, which is close to the vertical grid spacing of the

model (~250 m). For Boulder, CO, the WRF simulated LRT was several kilometers above the observed LRT. WRF simulated O_3 mixing ratios are generally lower than observed throughout the troposphere by ~20-40 ppb. This could suggest that the O_3 chemistry resulting from convective transport and outflow might be underrepresenting O_3. Above the LRT, WRF simulated O_3 concentrations differ from observations by several hundred ppb. For the purposes of assessing STT of O_3, these discrepancies between the model and observed O_3 state can suggest that simulated transport of O_3 may be underrepresented. Over the simulation period (5 August – 15 August), there appears to be no discernable trend in WRF simulated LRT and O_3 bias, demonstrating that the model temperature and chemical state does not drift over time.

4.3 Results

4.3.1 Relationship Between Convection and UTLS Composition

To understand how convection changes the chemical composition of the UTLS, timeseries of LS H_2O and UT O_3 were calculated for the two simulation periods. Specifically, several questions were assessed:

1) What is the net effect of convection on LS H_2O and UT O_3 over the simulation period?
2) How quickly does the chemical composition change in response to convection?
3) How long does the composition change last?
4) Is the composition change related to storm size, strength (updraft velocity), or a particular convective organization?

Total changes in the percentage of H_2O and O_3 mass (relative to total air mass) as well as the percentage of H_2O and O_3 mass in convective and non-convective air masses were calculated to understand the overall changes in the chemical composition in these layers. To link changes in H_2O and O_3 mass with convection, the fractional amount of cloud—defined as being a minimum concentration of at least 0.1 g/kg—in the LS layer was calculated ("convective fraction"). Lastly, to highlight the differences between tropical

and mid-latitude environments, locations with tropopause altitudes above 14 km in the May period and below 14 km in the August period were filtered out. Therefore, the May period should be representative of the effects of mid-latitude storms on UTLS composition while the August period represents tropical storms.

The UTLS layers analyzed in the time series were defined using two approaches: altitude relative to the LRT and potential temperature. The purpose of using a tropopause-relative altitude layer is to ensure that the mass budget calculations are for air either above or below the LRT. The depth of these layers was 2.5 km, such that, for example, the LS layer starts at the LRT and ends 2.5 km above the LRT. However, since the LRT can become ill-defined in the vicinity of active convection, the layers were also defined using potential temperature surfaces to both examine sensitivity to layer definition and avoid intermittent biases in the identified tropopause altitude. The potential temperature endpoints were selected based on frequency distributions of the potential temperature at the LRT from each simulation (Figure 54) to ensure that the layer limits were representative of either the upper troposphere or lower stratosphere. For the LS, the potential temperature surface representing the bottom of the layer was selected such that approximately two-thirds of the LRT potential temperatures were below that threshold (350 K for May and 370 K for August). The potential temperature depth of the LS layer was 30 K. For the UT, the potential temperature surface representing the top of the layer was chosen such that two-thirds of the LRT potential temperatures were above that surface (335 K for May and 360 K for August). The depth of the UT layer was 15 K, since the potential temperature gradient is weaker in the troposphere. However, since the LRT varies over the domains (especially in May), it is likely that there are some areas where the potential temperature endpoints are not representative of the intended layer of the atmosphere (e.g., the 350 K-380 K layer meant to represent the LS might actually contain parts of the UT in some parts of the domain).

4.3.1.1 May LS H_2O Mass

4.3.1.1.1 Tropopause-Relative Altitude Layer

The timeseries of LS H_2O mass in May suggests that the overall H_2O mass decreases over the duration of the simulation (Figure 55a). However, the decrease is largely due to the high H_2O mass that was present at the beginning of the simulation. Inspection of maps of stratospheric H_2O mass and cross sections of reflectivity and H_2O reveal that the high H_2O mass at the beginning of the period is associated with some weak convection along the domain boundary and a mid-latitude cyclone in Pennsylvania that lowered the LRT, thus increasing H_2O mass in the layer-defined LS. Therefore, the net decrease in H_2O mass over the simulation period should not be interpreted as a convective dehydration of the lower stratosphere.

Additionally, since convection occurs throughout the period, including first and last hours, it is difficult to assess the long-term effect that convection has on H_2O or O_3 mass. A strong convective event at the beginning or end of the period that yields large changes in H_2O or O_3 can provide a misleading interpretation. Thus, it is not appropriate to make conclusions about the net effect of convection on UTLS composition purely based on the difference in the H_2O or O_3 mass at the start and end of the period. Instead, we focus more on the time-evolving effects of convective events. To adequately assess the long-term impact of convection on UTLS composition over the United States, a 30-day simulation could be designed such that over the first and final 10-days of the period, convection would be disallowed in the model. During the middle 10-day period, the model would be allowed to simulate convection. The first 10-days would establish a good background chemical state while the final 10-days would show the long-term impacts of convection. Comparing the two non-convective environments would be a more appropriate way to determine what effects convection has on UTLS composition and what the long-term impact is.

There are six major convective events (identified as peaks in the convective fraction) that were simulated during the May 2011 simulation period: May 20 at 1200 UTC, May 21 at 0200 UTC, May 23 at 0300 UTC, May 24 at 0100 UTC, May 25 at 0700 UTC and May 26 at 0300 UTC. Figure 56 shows maps of the column-maximum

reflectivity for the six events. On May 20, a SW-NE oriented squall line initiated on 0600 UTC over the Great Plains and by 2000 UTC had merged to form an MCS over Missouri and Iowa. During the beginning of this period, the total LS H_2O mass increased by about 4.7%, but began to decrease after a few hours while the smaller convective storms merged. Around the time the MCS formed (~May 20 at 2100 UTC), another squall line formed in central Texas and Oklahoma and later new cells initiated in eastern Kansas, which resulted in a 15% increase in total LS H_2O mass.

On May 23, a squall line initiated in Missouri and Illinois at 0000 UTC while several discrete storms initiated in Texas. Although the storms in Texas were filtered out of the timeseries analysis because the tropopause was ~14.5 km, it is interesting to note that despite equal overshooting depths, the MCS in Illinois had a much larger effect on LS H_2O mass, likely due to the difference in the height of the tropopause between Illinois and Texas (12.5 km and 14.5 km, respectively). Overall, this event yielded a 14.2% increase in total LS H_2O mass. On May 24 at 0000 UTC, an MCS in the Great Plains and the Midwest initiated. Several hours later (0400 UTC), another MCS initiated in Missouri. Each MCS resulted in a substantial increase in LS H_2O mass (14.7%).

On May 25 at 0000 UTC, several discrete storms initiated along a N-S frontal boundary extending from central Nebraska to Texas in association with an mid-latitude cyclone in Nebraska. Similar to the convective events on May 23, the storms in Kansas and Nebraska had a much larger effect on LS H_2O mass than those in Texas and Oklahoma (the LRT was ~11.5 km in Nebraska and ~15.5 km in Texas). Furthermore, the tropopause over Texas and Oklahoma exceeded 14 km and as such the effects of those storms, though small, are not included in the calculation of H_2O mass. Interestingly, the total H_2O mass begins to increase a few hours before the convective fraction increases, and it is not clear at this time what is responsible. This event also had the largest impact on LS H_2O mass, increasing it by 16.1%. On May 25 at 2200 UTC, a line of storms initiated along the same frontal boundary from earlier that day that was now extending from Louisiana to Indiana. While many of the storms in Indiana, Kentucky, and Tennessee increased H_2O mass, the areas of impact were relatively small, resulting in a ~5.3% increase in LS H_2O mass.

Overall the storms that had the largest impact were the storms on May 23 (MCS in Missouri and Illinois), May 24 (MCS in Illinois, Missouri, and Kansas/Oklahoma) and May 25 (convection initiated off cold front and MCS in Nebraska). Theses events had the largest impact on stratospheric H_2O mass because of the location of the storms (northern latitudes, lower tropopause altitudes) and their size (multi-state events). In general, the total LS H_2O mass appears to respond to fairly quickly to convective activity. The H_2O mass in the non-convective air does not change significantly, although small increases in the non-convective mass are evident for several of the events discussed above. Overall, the convective H_2O mass is 93%-306% larger than the non-convective H_2O mass over the simulation period.

4.3.1.1.2 Potential Temperature Layer

When using potential temperature surfaces to define the lower stratosphere, the total H_2O mass generally increases throughout the period (Fig. 55b). The six periods identified in section 4.1.1.1 are still apparent, however, the first and last major events of the simulation now have a lower convective fraction relative to the other events. The events on May 21, 23, 24, and 25 are clearly the most impactful in terms of changes in total LS H_2O mass, increasing mass by 22.4%, 20.0%, 24.1%, and 34.7%, respectively. The event on May 26 increases total LS H_2O mass by 9.8% even though the change in the convective fraction is relatively small.

Using this layer definition, the total LS H_2O mass generally begins to increase as the convective fraction increases in the layer. Following the peak in convective fraction, the total LS H_2O mass remains elevated near peak level for 1-2 hours and generally takes ~24 hours to return to its pre-convective mass, which is consistent with the tropopause-relative altitude layer. Physically, this suggests that the removal of H_2O mass generally occurs through mixing with dry air in the stratosphere and generally takes several hours. Additionally, since the total LS H_2O mass increases as soon as the convective fraction increases, lower stratospheric hydration seems to begin as soon as the storm penetrates the tropopause. Overall, the convective H_2O mass is 155%-491% larger than the non-convective H_2O mass over the simulation period in the potential temperature layer diagnosis.

4.3.1.2 August LS H_2O Mass

4.3.1.2.1 Tropopause-Relative Altitude Layer

In August, the convective fraction oscillates between ~9-10% for the entire simulation period (Figure 57a). Over this period, the total and convective H_2O mass remains fairly constant with the exception of one large increase at the beginning of the simulation and some smaller changes towards the end. The non-convective H_2O mass slightly decreases throughout the period. The two periods in which there is a notable change in H_2O mass are August 7 at 1200 UTC and August 14 at 1200 UTC. Between August 7 and August 8, a large MCS moved ESE from Iowa to Virginia. The tropopause height was 14.5 km (Fig. 58), resulting in modest H_2O increases (11.1% increase). In general, since the height (and thus temperature) of the tropopause controls the ability of a convective storm to influence the LS H_2O mass, the lower the tropopause, the larger the change in LS H_2O. Thus, since regions with tropopause heights below 14 km were filtered out, the storms that are in environments with tropopause heights closest (but still greater than) 14 km will likely result in the largest changes in H_2O, regardless of size, organization, or strength. Throughout this simulation period, there are many examples of storms with cloud top altitudes of more than 1 km above the tropopause, however, many of them are in environments with high tropopauses (greater than 15 km) and thus have little impact on the LS H_2O mass.

On August 14, two MCSs (one in Oklahoma and one in Alabama) reached the LRT, resulting in modest changes in LS H_2O mass (7.1% increase). The tropopause was ~15 km for both of these storms, though both MCSs actually lowered the tropopause by nearly 1 km, effectively displacing the LRT-relative layer locally, resulting in larger H_2O mass. The maximum cloud-top relative altitude was less than 1 km for both storms throughout their lifecycle. A supercell in Mexico was also present, with overshooting depths of 2 km (LRT was ~16 km). While the supercell was able to locally modify the LS H_2O mass by a nearly equal magnitude as the MCSs, since the supercell covered a smaller area, the net impact was smaller.

Two other events, one on August 9 around 1800 UTC and another on August 11 around 0000 UTC also result in changes in LS H_2O mass (1.4% and 2.6%, respectively),

albeit smaller changes than the events on August 8 and 14. On August 9, an MCS moved towards the NE from Indiana towards Pennsylvania. Similar to the event on August 8, the tropopause was ~14.5 km, and maximum cloud top relative altitudes were less than 1 km. However, since the tropopause was relatively low, the temperature was warm enough to sufficiently hydrate the lower stratosphere. On August 12, the largest change in LS H_2O mass is not a direct result of convection, rather an increase in UTLS H_2O over Indiana from convection over the central Great Plains that hydrated the UT the day before that advected to the Midwestern states. It is also noteworthy that in some situations, convection lowers the LRT such that it becomes lower than 14 km and is filtered out, which is responsible for some rapid fluctuations in H_2O mass in this layer. Locally, convection increases H_2O mass by 41.0%-91.8% relative to the background H_2O mass.

4.3.1.2.2 Potential Temperature Layer

Using potential temperature surfaces to define the layer in the August 2013 simulation, there is generally the same trend in total H_2O mass, with the addition of one other event on August 13 at 0000 UTC. The increase in LS H_2O mass on August 13 appears to be similar to that of August 11 in that there is no active convection in the area of high H_2O mass and that the H_2O gradient appears to be higher in altitude. However, the shift in the H_2O gradient could be due to the single cell convection that occurred in the area 12 hours prior, though, it is unclear to the extent that convection is responsible. Otherwise, the differences in the two layers are not significant. The change in H_2O mass in this layer for the two main events (August 7-8 and August 14) increase LS H_2O mass by 4.3% and 4.0%, respectively. Locally, convection increases H_2O mass by 27.9%-58.9% relative to the background H_2O mass.

4.3.1.3 Seasonal H_2O Comparison

Overall, convection has a larger effect on LS H_2O mass in May than in August. H_2O mass changes by larger magnitudes in May and is also on average about one order of magnitude larger than in August. In May, there are at least 4 convective events that result in large changes in H_2O mass. In August, while there were more frequent convective

events, the change in the convective fraction was lower, and changes in H_2O mass only occurred with sufficiently large convective systems in environments with low tropopause altitudes. Therefore, we can conclude that the key factors in inducing measurable regional changes in LS H_2O mass from convection are storm size and the height of the tropopause. For the individual cases examined, the height of the tropopause was more important than the cloud-top relative altitude (or overshooting depth), suggesting that the depth of the overshoot alone is not enough to induce substantial changes in LS H_2O mass. The lower tropopause heights in spring will be warmer than the higher tropopause heights in summer. The ice crystals that mix with the warmer stratospheric temperatures in springtime will be able to hydrate the air due to the higher saturation mixing ratios.

4.3.1.4 May UT O_3 Mass

Since changes in UT O_3 concentrations have the largest effect on the radiation budget, the timeseries analysis for O_3 was done in an UT layer. Like with the LS layer, tropopause-relative altitude layer is also 2.5 km deep, but has the tropopause as the upper limit. The layer defined by potential temperature coordinates is 320 K – 335 K for May and 345 K – 360 K for August.

4.3.1.4.1 Tropopause-Relative Altitude Layer

To examine the net effects of convective transport of O_3, timeseries of O_3 mass were calculated for a layer in the upper troposphere, the layer of the atmosphere where convection has the largest effect on this trace gas (Figure 59a). Unlike water vapor, in which changes in LS H_2O mass are driven by ice crystal sublimation, the O_3 budget is dominated by air mass transport. Furthermore, using the convective and non-convective budget calculations, we can gain a deeper understanding of the primary direction of transport (TST vs STT) within convection. While the UTLS composition of CO is also of interest, since it is also primarily controlled by air mass transport, only O_3 will be discussed here.

For the first six days of substantial convective activity in the May 2011 simulation, the total O_3 mass in the UT is fairly constant, with only one period (May 21,

0000 UTC – May 22, 0000 UTC) where the percentage of UT O_3 mass increases (Fig. 59a). Between May 25 and May 27, the total UT O_3 mass increases by the largest percentage in the period (~19% over the 2 day period). Throughout the simulation period, the percentage of UT O_3 mass in the non-convective air is higher than in the convective air, which is expected considering the convective air originates in the boundary layer and lower troposphere, which generally has lower O_3 concentrations than upper tropospheric air in the midlatitudes. The percentage of UT O_3 mass from convection generally increases throughout the period, which could be due to the mixing of O_3-rich air via strong turbulent vertical motions in and around the updraft as shown in Chapter 3 (*Phoenix et al.,* [2019]). The non-convective O_3 mass generally follows the total UT O_3 mass although there are larger responses to the increases in the convective fraction during the three main events between May 23 and May 26. Furthermore, since the largest changes in O_3 mass are in the non-convective air, it suggests that the primary effect of convective transport is that of increasing O_3 mass in the UT via downward transport.

In assessing the individual events discussed in section 4.1.1.1, the events on May 23, 24, and 25-26 have the largest impact on UT O_3 mass. The O_3 mass is relatively constant for the convective events on May 20-21, during which time a large squall line covered much of the Great Plains. For the convective events on May 23, 24, and 25-26, the total UT O_3 mass and non-convective O_3 mass increase over the 4-day period, notably during the May 25-26 event. It is, however, difficult to assess the relative contribution of individual events to UT O_3 mass using the tropopause-relative altitude layer. In general, the UT O_3 mass steadily increases without a clear relationship to changes in the convective fraction.

One complication is that the top of the UT layer in a pre-storm environment is likely collocated with the sharp tropopause layer O_3 gradient. Changes in O_3 mass within the layer could represent a shifting of the top of the layer towards higher O_3 concentrations as the storm perturbs the tropopause rather than vertical transport of air into the layer. A large MCS such as the one on May 25-26 could vertically perturb the local tropopause, effectively shifting the layer into a higher O_3 environment. Thus, this aspect of the tropopause-relative altitude layer analysis makes it difficult to attribute diagnosed changes in UT O_3 mass to convective events.

4.3.1.4.2 Potential Temperature Layer

Compared to the layer defined by tropopause-relative altitude coordinates, there are much larger fluctuations in the total, convective, and non-convective UT O_3 mass, such that we can attempt to attribute changes in O_3 mass to individual events (Fig. 59b). For the three main events (May 23, 24, and 25-26), there is generally a 12-hour lag between the peak in the convective fraction and the peak in the non-convective and total UT O_3 mass. The convective O_3 mass also increases following a large convective event.

Overall, the largest changes in total UT O_3 mass follow the convective events on May 23, 24, and 25-26 (18.3%, 8.2%, and 14.9%, respectively), with the largest increase in O_3 mass following the event on May 23. Each of these events typically had a large MCS span several states in the northern half of the domain, which likely forced subsidence via a mass conservation circulation in the low tropopause environment. The events on May 20-21 likely did not result in large changes in UT O_3 because they were smaller squall lines or supercells in environments with higher tropopauses (thus the mass conservation circulation is not as effective). However, the large increase in O_3 mass around May 27, 0000 UTC was associated with downward transport from a squall line in the SE US spanning the Gulf of Mexico to Ohio that also mixed a lot of high O_3 air into the storm (rather than around the anvil), which resulted in an increase in the convective O_3 mass. However, the tropopause height was several kilometers lower than the squall line on May 20 and 21.

4.3.1.5 August UT O_3 Mass

4.3.1.5.1 Tropopause-Relative Altitude Layer

During the August period, total UT O_3 mass slightly decreases throughout the period (Figure 60a). Convective and non-convective O_3 mass remain fairly constant throughout the period and the non-convective O_3 mass is generally about 20% higher than the convective O_3 mass. There are few variations in the total UT O_3 mass, with the exception of the last two days of the simulation (August 14-15). The lack of an effect on the UT composition is not surprising here since mass continuity is likely the key driver of downward transport. With higher tropopause heights, the storms reach the tropopause

with less momentum and surface area to drive large quantities of stratospheric (or tropopause layer) air downward. On August 14-15 there were several convective systems, notably an MCS in Oklahoma and Alabama. However, the increase in UT O_3 mass during this period was likely caused by an intrusion of stratospheric air near the subtropical jet. Therefore, it does not appear that convection has a large impact on UT composition during this period.

4.3.1.5.2 Potential Temperature Layer

The greater impact on UT ozone can be diagnosed in potential temperature coordinates (Fig. 60b). In particular, there are about four events between August 6 and August 10. As with the UT layer defined in tropopause-relative altitude coordinates, there is a decrease in total O_3 throughout the period, but with this layer there are larger variations in the convective and non-convective mass. The UT O_3 mass also increases at the end of the period (August 14-15), but this appears to be caused by large-scale mixing processes and not convection. The non-convective O_3 mass decreases through much of the period, only increasing on August 14 when stratospheric air was mixed into the UT above the subtropical jet. The convective O_3 mass fluctuates with changes in the convective fraction between August 6-10, but generally decreases throughout the period as well.

The changes in total UT O_3 mass do not appear to be a result of the anvil wrapping process during the August 2013 simulation, but rather a drawing down of air above the convective system, thus increasing the UT O_3 mass in the convectively identified air. This could be caused by a collapsing overshoot drawing down stratospheric air from aloft. It is not clear how this process happens and should be the subject of future work. However, it should also be noted that these changes in O_3 mass mainly occur close to the domain boundaries and are not always associated with convection, suggesting that there may be some issues with the chemical gradients near the domain boundaries. In cases where there is convection in the vicinity of these high O_3 features, it is not clear to the extent that convection is responsible. Within the interior of the domain, there are no notable occurrences of downward transport in convection. Therefore, it does not appear that convection plays a large role in affecting the chemical composition of the upper troposphere.

4.3.1.6 Seasonal O_3 Comparison

Comparing the budget calculations for the two seasons, springtime convection has a larger impact on variations in UT O_3 mass. While the total layer percentage of UT O_3 mass in the layer is consistent between May and August, the variations in O_3 mass in response to a convective event were much larger during springtime convection. Convection typically increased UT O_3 mass in May, especially during periods when there were large convective systems (May 23-26). In August, however, there is an overall decrease in UT O_3 mass and the few variations in O_3 mass appear to be mostly due to issues in the chemical gradients along the border of the domain and not directly caused by convection. In general, this difference makes sense considering the mass conservation hypothesis for driving downward transport around a MCS. Storms in higher tropopause environments—such as those in August—will not reach the tropopause with sufficient force to efficiently subside O_3-rich stratospheric air. The events that resulted in the largest changes in UT O_3 mass in May were large convective systems, typically spanning multiple states and in lower tropopause environments.

4.3.1.7 Advantages and Disadvantages of Each Layer Definition

Compared to the budget calculations for the layer with tropopause-relative altitude limits, the potential temperature layer presents a clearer relationship between convective activity and changes in UTLS composition. The advantage of using potential temperature surfaces is that transport across isentropes is mostly irreversible. The LRT, however, often becomes ill-defined in the vicinity of active convection and as such may not accurately represent cross-tropopause transport. Additionally, the LRT is routinely perturbed—shifted vertically—by convection, and as such the layer limits will be shifted by unequal depths above the updraft and anvil. Therefore, within the area encompassing a convective storm, the tropopause-relative layer limits may differ by several kilometers. Furthermore, there are situations in which the LRT is not well-aligned with the chemical gradient, muddying the interpretation of convective transport and its impact on UTLS composition. However, it is useful to note that while the LRT does not always center on the chemical transition between the troposphere and stratosphere, other definitions, such

as the dynamic tropopause, would also suffer from convective perturbations and would require a subjective threshold to be determined which would not be feasible given the large range in tropopause heights across the domain.

A disadvantage of using a layer defined by potential temperature is that in some situations, the potential temperature surface used to define the endpoints of the layer may result in a layer spanning both the UT and LS, instead of only one of these layers. For example, the bottom of the May LS layer, which was defined as being the 350 K surface, may be below the LRT in some regions and thus include tropospheric air. Likewise, at other locations the 350 K surface may be above the LRT, thus excluding some LS air. In the LS in August, there were relatively few substantial changes in H_2O mass. In this environment, when the tropopause is high and cold, slight shifts in the layer can result in large changes in H_2O mass since the water vapor concentration is near saturation. Furthermore, since the tropopause is much higher and convection will have a lesser impact on perturbing the LRT, the tropopause-relative altitude coordinate may be a better approach in such environments. The disparities between the layer types are likely exacerbated by strong convective systems that perturb the LRT tropopause.

4.3.2 Impact of Convection on UTLS Composition

4.3.2.1 Tropopause-Relative Impacts

To understand the overall impact that convection has on the chemical composition of the UTLS, profiles of H_2O, O_3, and CO were binned in tropopause-relative space and by tropopause altitude (Figure 61). Profiles of convective and non-convective air were calculated using the passive tracer with a threshold of 10% to distinguish between convective and non-convective environments. Profiles were calculated in a tropopause-relative framework because the LRT often corresponds with the sharp chemical transition of H_2O, O_3, and CO and changes in concentrations of these trace gases (and H_2O) are easily shown in this framework [*Pan et al.,* 2004]. For each tropopause altitude and tropopause-relative bin space, the mean H_2O, O_3, and CO mixing ratio is calculated. Profiles were also sorted and binned by the tropopause altitude because environments with different tropopause heights also have different chemical and thermodynamic

characteristics. For example, higher tropopause altitudes are typically colder than lower tropopause altitudes. As shown in section 4.3.1, since the temperature of the tropopause controls the amount of water vapor that enters the stratosphere, it would be expected that there be a larger LS H_2O enhancement in environments with a lower tropopause, as has been confirmed with cross sections of many different cases with a wide range of tropopause heights (not shown). Therefore, important details are hidden without this distinction.

Overall, convection has the largest effect in environments with lower tropopause altitudes and during springtime (May), since the tropopause was generally lower during this period. For tropopause heights between 11-13 km, convection increases H_2O by up to 300% in the lower stratosphere (up to 2 km above the LRT, Fig. 61). The O_3 and CO changes are largest in the UT for tropopause heights between 11-13 km. In general, UT CO concentrations increase by 50% and UT O_3 concentrations decrease by 50% in convective air relative to non-convective air, which suggests that the dominant transport direction is upward transport of boundary layer and lower tropospheric air. However, since downward transport of stratospheric air would likely be identified as non-convective, this difference could also suggest that high O_3 and low CO are transported downward in the non-convective air. Further inspection of the non-convective profiles reveals that O_3 (CO) concentrations are relatively higher (lower) in the UT for the 11-12 km tropopause altitude range to relative similar tropopause-relative altitudes for other tropopause heights (e.g., 10 km, 13 km). Differences in LS changes in H_2O, O_3, and CO suggest that H_2O changes are due to more than just air mass transport (which primarily controls changes in O_3 and CO). However, additional analyses are needed to confirm this supposition.

For higher tropopause altitudes (14-16 km) that were more characteristic of summertime (August) environments, the effects of convection on the lower stratosphere are reduced (Figure 62). Changes in LS H_2O are small (less than 25%) and the maximum changes in H_2O are 2 km below the LRT. The largest changes in O_3 and CO are also in the UT, but the effects of convection are lower (25% reduction in O_3 and 25% increase in CO). Given the large difference in H_2O changes between high tropopause environments and low tropopause environments and low difference between changes in CO and O_3, this

suggests that the thermodynamic controls on H_2O transport play a large role in determining the changes in LS H_2O due to convection. Additionally, UT H_2O changes are actually larger in environments with higher tropopauses than with lower tropopauses. Since these analyses are conducted in a tropopause-relative framework, the absolute altitude of these H_2O changes is similar (maximum change around 12-13 km) which suggests a threshold constrained by thermodynamic factors (e.g., temperature).

4.3.2.2 Chemical Mixing Signatures

To further examine the chemical impact of tropopause-penetrating convection on the UTLS layer, tracer-tracer diagrams were analyzed to identify unique mixing signatures. Figure 63 shows H_2O-O_3 correlations for convective and non-convective air masses, and the difference between the two for May and August. Counts of coincident O_3 and H_2O concentrations are binned in the tracer-tracer space and shaded by their frequency by altitude. In May, the most frequent tracer-tracer space in non-convective air masses aligns with the "L" shape expected in air masses with little to no mixing. There are moderate (7-8%) frequencies of high H_2O (10-40 ppm) in areas of high O_3 (200-500 ppb) in the non-convective air mass, which could be due to the initial and boundary conditions containing some convective air. In the convective air mass, the stratospheric branch is moistened considerably, with H_2O up to 200 ppm where O_3 is 300 ppb. The location of maximum frequency increases from ~3-4 ppm to 30-40 ppm of H_2O in the O_3 layer of 200-400 ppb. There is also evidence of enhanced O_3 within the tropospheric branch, which could suggest downward transport and mixing of air with higher O_3 concentrations, or in situ chemical production. In August, the primary frequency pattern for both convective and non-convective air masses resembles the "L" shape. There is a slight moistening in the stratospheric branch of the convective air mass, but the impact is much lower compared to May.

Figure 64 shows CO-O_3 diagrams for May and August. For May, both convective and non-convective air masses occupy a similar tracer-tracer space. However, the most frequent tracer-tracer space shifts towards high O_3, high CO mixing in the convective air, which represents enhanced mixing between more polluted (lower altitude) troposphere air and LS air. In August, there is less discernable difference between the convective and

non-convective air (especially at the scales shown), but convection still leads to higher O_3, higher CO mixing. Overall, convection leads to both a broader region of mixing between the troposphere and stratosphere air as well as a deep layer of enhanced stratospheric hydration. Summertime convection potentially decreases LS H_2O.

4.3.3 Storm Characteristics Conducive to High H_2O Changes

One major finding thus far is that tropopause-penetrating convection in environments with lower tropopauses (11-13 km) has a larger effect on the chemical composition of the UTLS than convection in high tropopause (14-16 km) environments. A goal of this study is to establish if characteristics of the storms and their environments affect the magnitude and depth of the chemical change. To address this, relationships between changes in trace gases and several storm/environmental characteristics were analyzed. Storm and chemical characteristics were analyzed in cylinders centered on the location of overshooting tops. The center of the cylinder was marked by the highest altitude where the cloud (total precipitable water) concentration exceeded 0.1 g kg^{-1} above the LRT. An overshooting dome is at least 20 km in diameter. Cross section analysis indicates that convection can increase stratospheric H_2O mixing ratios up to 4 km above the LRT and can extend 50-100 of kilometers away from the overshooting dome. As such, the cylinders are 130 km in diameter and 4 km deep with the lowest point being the LRT to contain the region of convective influence. If multiple overshooting tops existed within this area, they were grouped together and the centermost overshoot was chosen as the storm's center. Several characteristics of the storm were considered, including overshooting depth, updraft strength (area of 5 dBZ echo at tropopause multiplied by the updraft speed at the tropopause), ice mass mixing ratio, relative humidity with respect to ice, and number of unstable layers. Since the impact of convection depends on the height of the tropopause (see sections 4.3.1 and 4.3.2.1), the tropopause altitude was held constant for these relationships.

Figures 65 and 66 show the mean H_2O mixing ratio outside of cloud in the cylinder and several storm characteristics for May and August, respectively. Since the H_2O within cloud may return to the troposphere, only points outside of cloud were considered under the assumption that this air includes convectively lofted mass that has

been irreversibly mixed into the stratosphere. As in Figure 65a, higher mean H_2O concentrations tend to correspond with higher mean tropopause temperatures, however, this is not a direct relationship. The overshooting depth, or maximum cloud-top height above the LRT, is slightly related to mean water vapor concentrations (Fig. 65a). Tropopause temperatures cooler than 210 K are typically associated with low H_2O concentrations (less than 10 ppmv). Locally, high H_2O concentrations are located where tropopause temperatures range from 210-213 K while low H_2O concentrations are located with slightly warmer tropopause temperatures (215 – 220 K). While the tropopause temperature likely plays a large role, other characteristics of the storm's environment also contribute.

For a given tropopause temperature, the mean H_2O concentration tends to increase with increasing overshooting depth, but not always. While overshooting depth may result in higher mean H_2O concentrations as suggested in [*Dauhut et al*., 2018], it is not the only factor. The strength and area of the updraft—calculated as the area of the 5 dBZ echo at the tropopause multiplied by the vertical velocity at the tropopause—does not show a strong relationship to the mean H_2O concentration (Fig. 65d).

The mean ice mass mixing ratio shows a clearer relationship with H_2O mixing ratios than overshooting depth, with high H_2O mixing ratios located in areas with high ice mass mixing ratios, and warmer tropopause temperatures (Fig 65c). Still, while the highest H_2O mixing ratios tend to be located in areas with ice mass mixing ratios in the range of 10-20x10^{-5} kg kg^{-1}, several low H_2O observations are located in areas with ice mass mixing ratios in the 30-40x10^{-5} kg kg^{-1} range and for tropopause temperatures of 210-225 K. The mean relative humidity with respect to ice (RHi) shows an interesting relationship to the mean H_2O concentration (Fig 65b), with the highest H_2O concentrations located with RHi values in the 2-3% range and for cooler tropopause temperatures (210-215 K). Similarly to the ice mass mixing ratio relationships, when considering all observations (in cloud + out of cloud), there is a more direct relationship of H_2O concentrations increasing with increasing RHi and tropopause temperature. However, for RHi values less than 2% and tropopause temperatures colder than 210 K, the average H_2O concentration is less than 10 ppmv.

Since it seems likely that some other aspect of the storm's environment seem responsible for the 'anomalously' high H_2O mixing ratios, several other characteristics were analyzed. To investigate the role of gravity wave breaking, which has been shown to play a leading role in irreversible transport of H_2O in convection [*Lee*, 2003], relationships between the number of unstable layers—locations where the potential temperature lapse rate is less than 0 K km^{-1}—were analyzed (not shown). Despite the established link between wave breaking and irreversible transport, there is no relationship between these two variables here. This is not too surprising, given the disparity between the temporal frequency of model output analyzed here (hourly) and the timescale at which gravity wave breaking takes place (seconds). It is possible that the extent of gravity wave breaking can be related to some of the observed variability in LS H_2O, but a relationship was not clear using only the times that output files were written.

For summertime convection, the same relationships exist, but there is a clearer separation between environments with cold tropopauses (less than 205 K) and warmer tropopauses (greater than 205 K). The highest H_2O concentrations are located where the warmest tropopause temperatures, highest ice mass mixing ratios (Fig. 66c), and greatest overshooting depths are (Fig. 66a). Additionally, H_2O concentrations typically increase with increasing RHi, which shows a clearer relationship than with springtime convection (Fig. 66b). There is still no clear relationship between H_2O concentrations and updraft strength (Fig. 66d) or with the number of unstable layers (not shown). Based on this, there is not a large difference between the storm characteristics driving LS high H_2O concentration in springtime and summertime convection, suggesting that the main difference between these two seasons is the height (and temperature) of the tropopause. The main change in H_2O concentrations is located at lower/warmer tropopause heights/temperatures. For tropical environments, where the tropopause is greater than 15 km, there does not appear to be a measurable change in H_2O concentrations, assuming the background H_2O concentration is 5-10 ppmv. Therefore, these results suggest that convection mainly increases LS H_2O in the mid-latitudes and has a smaller effect in tropical environments, consistent with the main findings in section 4.3.2.1.

It is possible that the lack of any relationships in the overshoot analysis here is due to the coarse temporal resolution of the model output used. The data analyzed

represents the instantaneous conditions at each hour, but does not provide any information about the history of the analyzed air masses within each storm at intermediate times. The time scales of key features—such as the maximum overshooting depth and gravity wave breaking events—occur on the timescale of minutes. It is possible that multiple gravity wave breaking events could occur in the time in between output periods. Additionally, the maximum overshooting depth in the analyzed data might not be representative of the true maximum overshooting depth of that storm. Ultimately, it is not logical to compare the instantaneous overshooting depth to the instantaneous H_2O concentration. It would be best to track the evolution of an individual storm and compare its maximum overshooting depth (or other variable) to the water vapor concentration. However, tracking storms is not possible with hourly output.

4.3.3.1 Case study: 30-31 May 2012

Relationships between H_2O and several storm characteristics were analyzed for an MCS simulated with high spatial resolution and high temporal output (5 min). The case and simulation has been described in Chapter 3 (*Phoenix et al.* [2019]). The output frequency allows for an examination of these features and the resulting H_2O concentration as the storm evolves.

Figure 67 shows scatterplots between the H_2O mixing ratio and the overshooting depth and ice mass mixing ratio during two periods: early in the MCS lifecycle (2250-0040 UTC) and late in the MCS lifecycle (0205-0350 UTC). During the early stage, there are a high collection of points with warmer temperatures and high overshooting depths. However, the H_2O mixing ratio at this time was relatively low (~10 ppm). Later, the temperature is colder, suggesting that the LRT was shifted upward by the MCS. Additionally, the mean H_2O mixing ratio is generally higher (upwards of ~60 ppm), especially for temperatures ~220 K and where overshooting depths ranged from 2-3 K. The relationship between ice mass mixing ratio and H_2O mixing ratio is similar. Despite higher ice mass mixing ratios during the early period, the highest H_2O mixing ratio are found later, with lower ice mass mixing ratios.

When combining these time periods, the resulting scatterplot exhibits no relationship between the variables. This case study suggests that modifications to the

environment by the storm, such as perturbing the tropopause, play a role in the resulting H_2O mixing ratio and interpretation of the composition-storm relationships. Additionally, the analysis is limited by its ability to track storms. Since it takes time to sublimate ice crystals, it is not likely that high H_2O concentrations would be collocated with high ice mass mixing ratios or overshooting depths. Therefore, without the ability to accurately track storms (which requires temporal output ~5 min), it is not possible to answer the proposed questions in section 4.3.3.

4.3.4 Objective Methods to Identify STT ("Anvil Wrapping")

Recently, anvil wrapping of stratospheric O_3 (>150 ppb) was observed around a deep convective cloud [*Pan et al.,* 2014]. However, little is known about how often this occurs and if/how anvil wrapping varies with storm environment, type, or intensity. This observation is important for several reasons: 1) it provides a for the tropospheric O_3 budget, 2) it challenges the current understanding of how much UT O_3 is produced by LNOx, and 3) it introduces the need to understand the frequency of this transport process, as it is not resolved in current climate models. A summertime maximum in UT O_3 is typically observed in the southern US associated with the UT anticyclone of the North American Monsoon. Traditionally, this O_3 maximum has been attributed to in-situ production via LNOx. However, given the potential for these thunderstorms to transport stratospheric air into the troposphere, it is worth investigating how frequently anvil wrapping occurs in the southern US and if this is a contributor to the increased UT O_3. Additionally, since O_3 is a greenhouse gas in the UT, understanding how the frequency of these storms may change in a changing climate is important to determining the role of anvil wrapping (and thus increased transport of ozone from the stratosphere to troposphere) in the future.

Recent studies have estimated stratosphere-troposphere flux from deep convection on a global scale [*Tang et al.*, 2011] from a model with parameterized convection. *Frey et al.* [2015] looked at the vertical transport between the stratosphere and troposphere from deep convection in a tropical environment. However, no convection-allowing modeling studies have investigated the downward transport of O_3, specifically from anvil wrapping, in the extratropical US, where tropopause-penetrating convection frequently occurs.

Here, we present an estimate of the frequency of anvil wrapping during different periods when there was a high frequency of tropopause-penetrating convection in the United States. We assess the frequency of anvil wrapping, and investigate its dependency on storm type and intensity using numerical simulations with WRF-Chem.

4.3.4.1 Description of the Objective Algorithm

The distinguishing feature of anvil wrapping is the thin tongue of O_3-rich air extending down into the UT along the periphery of a convective anvil. Therefore, the algorithm described below aims to isolate certain criteria that are indicative of this feature, such as the cloud concentration, cloud fraction, local O_3 concentration and mean O_3 concentration at that altitude. Since anvil wrapping has a spatial dependency on multiple variables, the criteria were assessed within a 90 km^2 box bounding each grid point. Within each 90 km^2 box, the specific criteria to determine wrapping are as follows:

1. A total-condensed cloud mixing ratio of at least 0.1 g kg^{-1} must cover at least 10% and no more than 66% of the box. This is to determine that there is some cloud material within (anvil wrapping occurs around the cloud) but not so much that the box is contained entirely within cloud (e.g., an overshooting dome or tropopause-reaching anvil). This also eliminates "false-positives" where the LRT was vertically displaced such that the chemical transition occurred in the UT. The cloud criterion is also one of several attempts to eliminate the possibility of erroneously identifying large-scale transport as anvil wrapping.
2. The air that may be flagged as anvil wrapping must be associated with a non-convective air mass (passive convective tracer must be less than 0.1, or less than 10% convective air).
3. The ozone concentration in the candidate air must be greater than 150 ppb (consistent with that of typical stratospheric or transition layer air).
4. The grid volume will only be flagged if these criteria are met AND the volume resides at an altitude at least 250 m below the LRT.
5. The total anvil wrapping depth is estimated by summing the depths of flagged volumes in a column.

These criteria were evaluated for all grid volumes in the troposphere and for all times that model output was available.

4.3.4.2 Evaluation of the Algorithm

For the two periods, the anvil wrapping algorithm identifies several times of STT around active convection in May, but very few times in August (Figures 68-69). Figure 70 shows vertical sections through several storms that had been flagged as having anvil wrapping. Several storms appear to exhibit downward transport of air around the anvil cloud. In some situations, there is downward transport of air, such that the ozone contours cross the potential temperature surfaces in the UT, likely leading to irreversible transport (Figure 70c,d). However, in most situations, despite an indication of downward transport of relatively high-O_3 air, the origin of the air is not stratospheric, but rather comes from higher altitudes within the troposphere. Pairing vertical sections of O_3 with a passive tropospheric tracer reveals that much of the identified examples of anvil wrapping do not contain stratospheric air (Figure 71). This lack of transport was further discussed in Chapter 3 (*Phoenix et al.,* [2019]).

A few other examples appear to give the illusion of transport (Figure 70b), however, further inspection of the UT O_3 concentration in the unperturbed air ahead of the storms suggests that there is actually very little downward transport around the anvil. Instead, low O_3 air from the boundary layer is injected into the UT via the updraft and anvil outflow, becoming injected in between the ~200 ppbv O_3 air that was in the UT prior to convection. In this situation, we conclude that this is a false positive. In general, this situation is present with several other storms throughout the period.

In August, there are very few examples of anvil wrapping (Figure 69). This is consistent with the conclusion presented in Chapter 3 (*Phoenix et al.,* [2019]), which stated that the main driver of anvil wrapping is mass conservation from a large MCS impinging on the tropopause layer, forcing air aloft down and eventually around the anvil. Since the tropopause is much higher, the storms do not have sufficient force when reaching the tropopause to force this subsidence (Figure 72). Therefore, anvil wrapping—while perhaps not adequately simulated in these 10-day simulations—seems to more readily occur with springtime convection where the tropopause is lower and large MCSs

meet the tropopause with sufficient force and area to drive UTLS air outward and along/below the cloud boundary and anvil.

In the UT over the SE US, a reoccurring summertime maximum in O_3 has been observed in several studies [*Cooper et al., 2006; Cooper et al., 2007; Barth et al.*, 2012]. This maximum in UT O_3 is generally thought to be caused by the recirculation of air in the North American monsoon anticyclone, which regionally confines the convective outflow and air rich in LNO_X in the UT for long periods of time over the SE US. Abundant solar radiation, high temperatures, and moisture create an environment conducive to O_3 formation. However, given the recent discovery of downward transport of O_3-rich air around MCSs, it was hypothesized that this transport pathway could also contribute to the UT O_3 enhancement. However, given the conclusions from section 4.2.5 and those presented in this section, transport of stratospheric air into the UT is likely a small contribution to the SE US upper troposphere as a result of convection during the summer.

4.4 Conclusions and Future Work

Two 10-day WRF-Chem simulations were performed to assess the effect of tropopause-overshooting convection on the chemical composition of the UTLS. One period representative of springtime convection (May 18-27, 2011) and one period representative of summertime convection (August 5-15, 2013) were chosen to examine the differences in convective transport between the two seasons.

Overall, springtime convection has a net effect of increasing LS H_2O (within 2 km of the LRT) by ~300% locally (e.g., H_2O mixing ratios in convective air are 300% higher than non-convective environments). Large convective events (e.g., MCSs spanning multiple states) routinely increase H_2O mass by 20% over the entire lower stratospheric layer. The effects of convection on LS H_2O are greatest in regions with lower tropopause altitudes, due to the warmer temperatures at the tropopause, at which the air is highly subsaturated with respect to ice. While summertime convection does modify the LS locally, the overall changes are much smaller than those in springtime convection.

Changes in O_3 and CO are also larger with springtime convection, but the changes are largest in the upper troposphere. O_3 and CO mixing ratios are ~50% lower and higher,

respectively in convective air masses relative to the background (non-convective) environment. Timeseries analysis suggests that while convection does transport boundary layer air into the UT, the primary impact comes from downward transport around the convective air (e.g., the thunderstorm cloud boundary), such that O_3 and CO mixing ratios increase and decrease, respectively in the non-convective air.

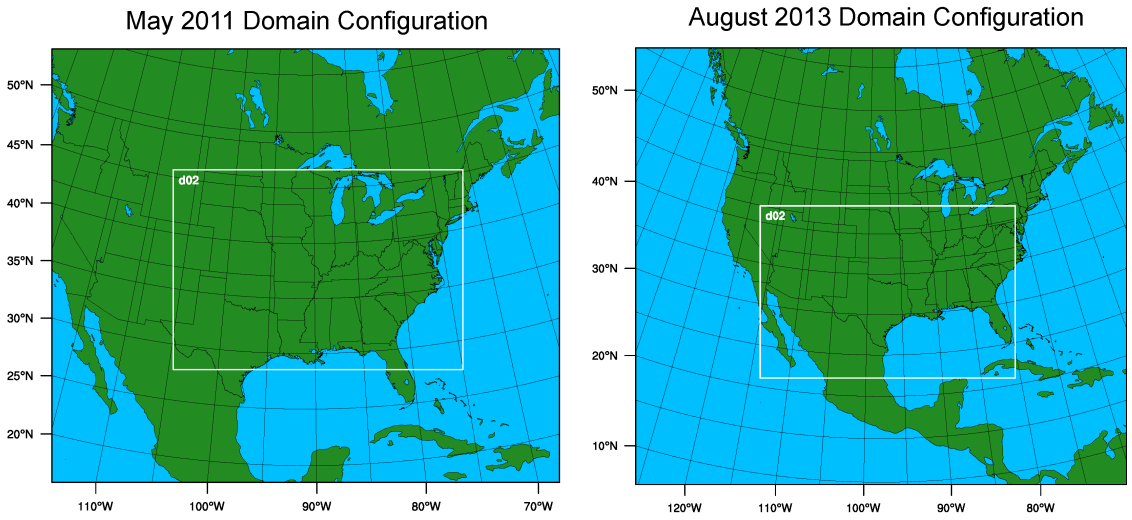

Figure 47. Parent (15-km horizontal resolution) and nested (3-km horizontal resolution) domains for May 2011 (left) and August 2013 (right) periods.

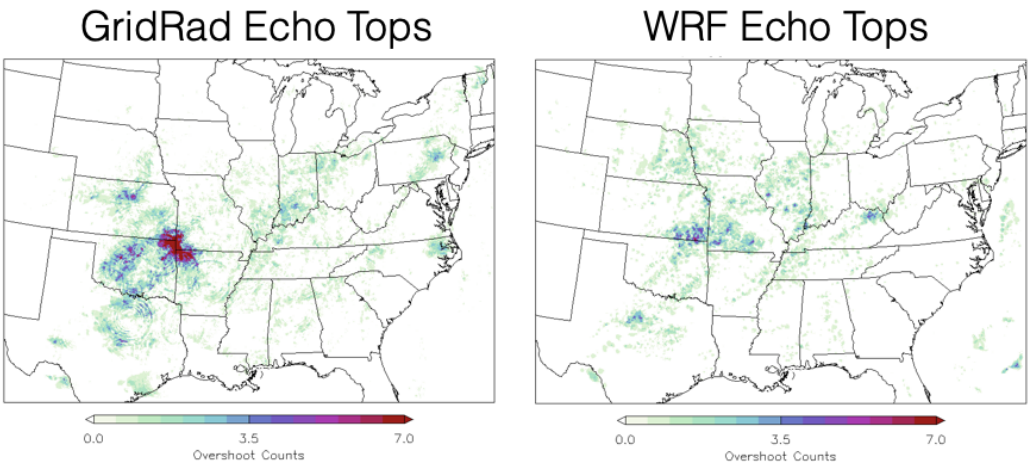

Figure 48. Cumulative counts of grid cells where the 10-dBZ echo top is 500-m above the LRT and higher (GridRad, left) or 500-m below the LRT and higher (WRF, right) for May 19-27, 2011.

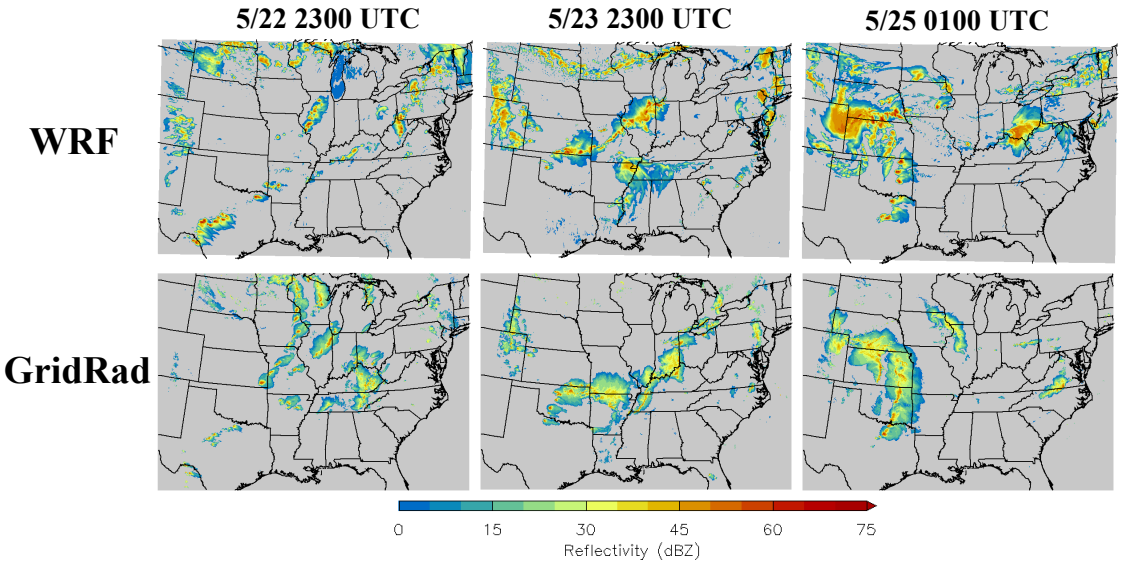

Figure 49. Comparisons of column-maximum reflectivity between the WRF simulation (top) and observations (GridRad, bottom) for three times: May 22, 2100 UTC, May 23, 2300 UTC, and May 25, 0100 UTC.

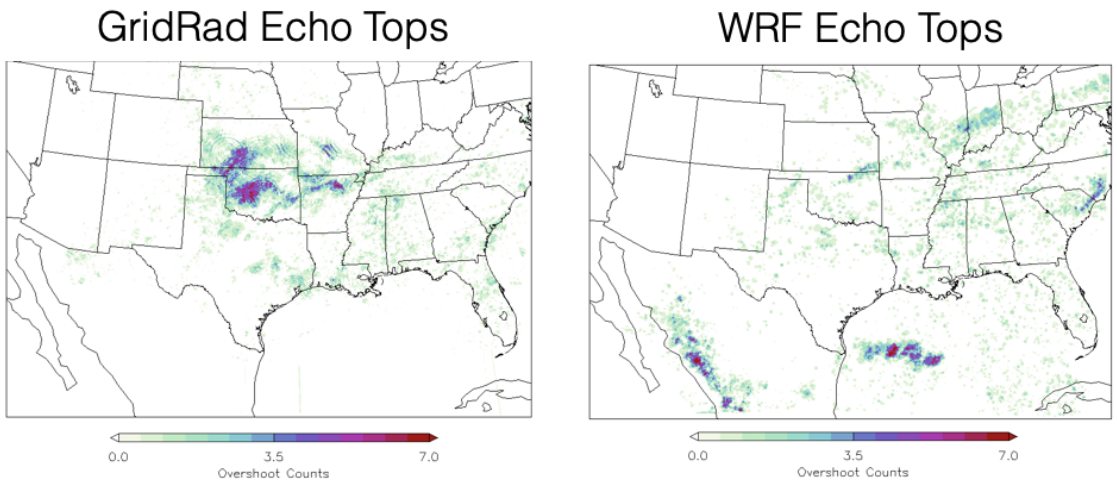

Figure 50. As in Figure 48, but for August 2013.

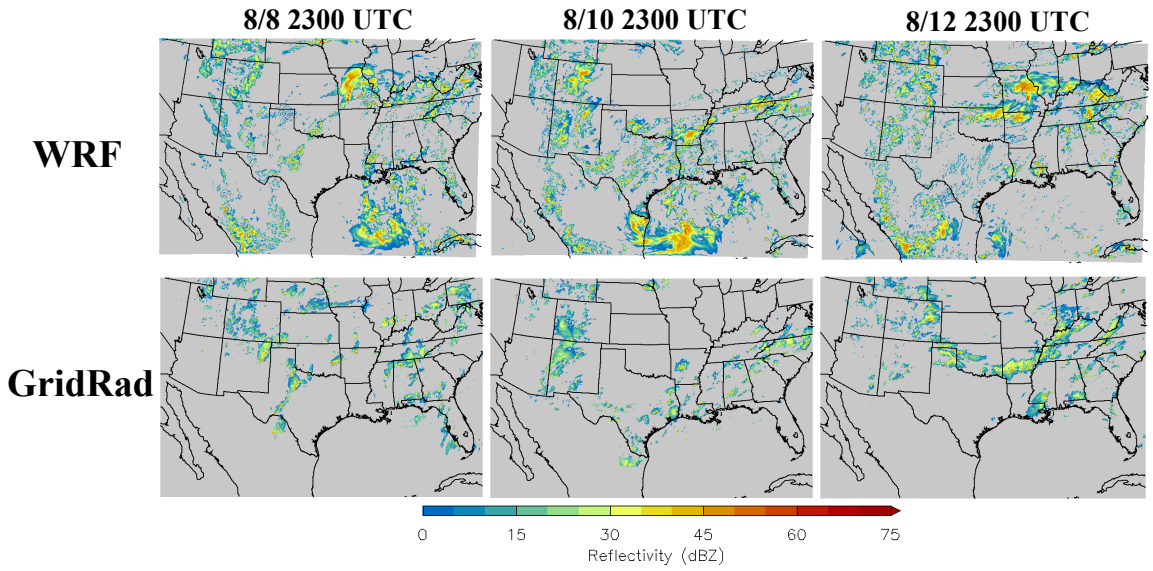

Figure 51. As in Figure 49, but for August 2013. The three times shown are August 8, 2300 UTC, August 10, 2300 UTC, and August 12, 2300 UTC.

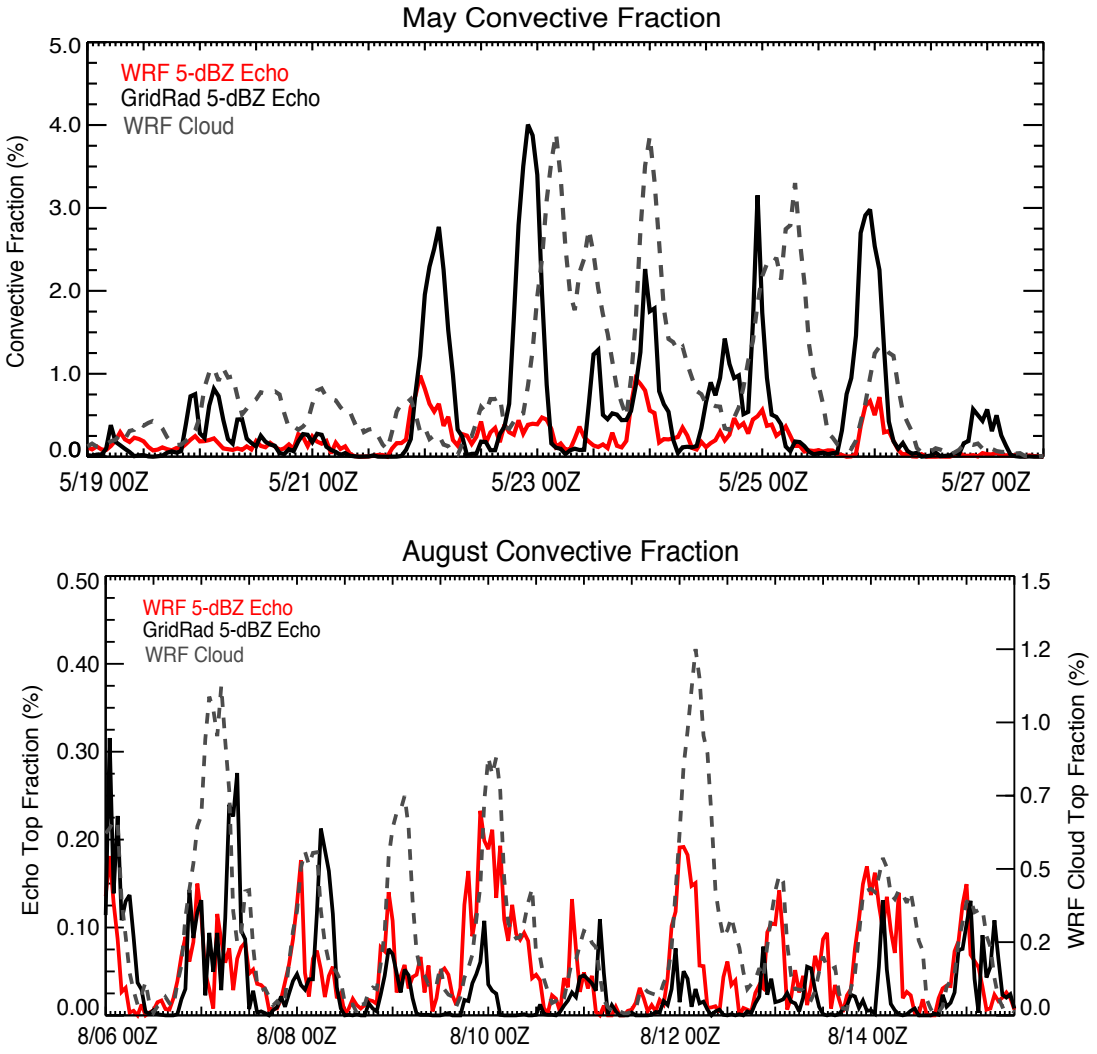

Figure 52. Timeseries of the fractional volume of the stratosphere covered by the 5 dBZ echo top (convective fraction, black line (GridRad), gray line (WRF)) and fractional volume of the stratosphere where the cloud concentration is at least 0.1 g/kg (red line). May 2011 is on the top and August 2013 is on the bottom

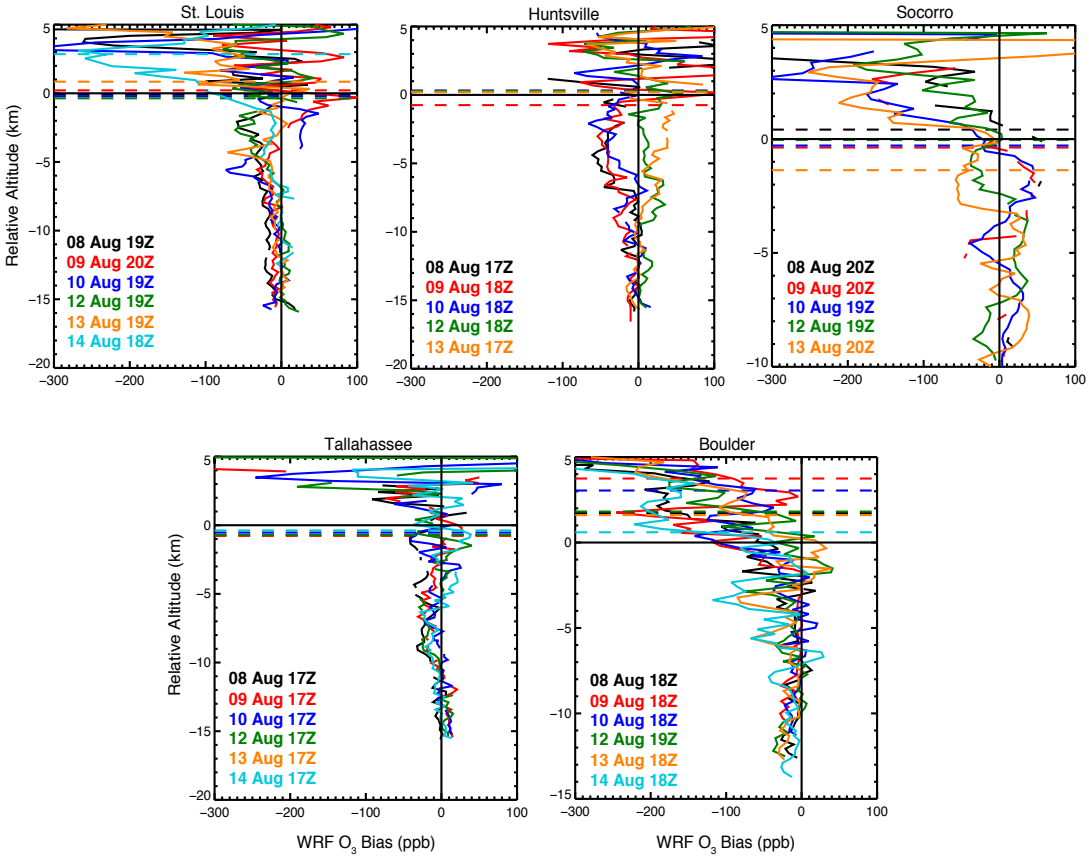

Figure 53. Difference between the WRF-simulated LRT (dashed lines) and O_3 mixing ratios (solid lines) and observations from ozonesondes for several times during the August 2013 period. Locations were evaluated for several locations with available ozonesondes: St. Louis, MO, Huntsville, AL, Socorro, NM, Tallahassee, FL, and Boulder, CO.

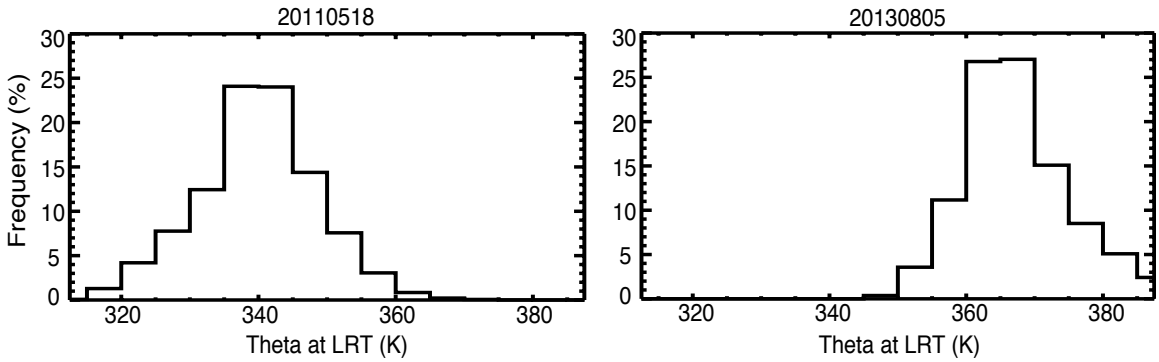

Figure 54. Frequency distributions of potential temperature at the LRT for May 2011 (left) and August 2013 (right).

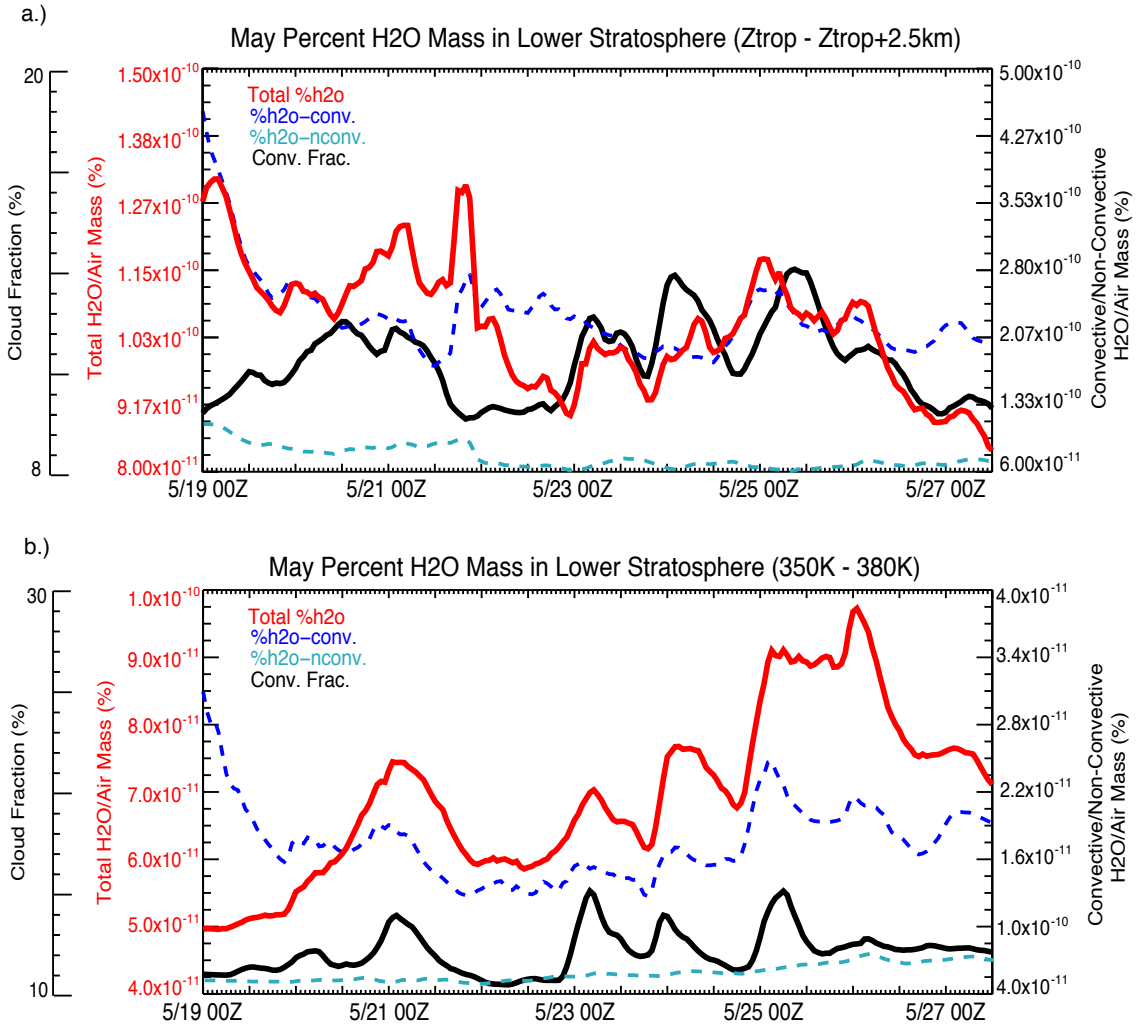

Figure 55. H_2O mass budget calculation in the lower stratosphere for May 2011. The lower stratosphere is defined in two ways: altitude relative to the tropopause, evaluated at each grid point (a) and as a fixed layer defined by potential temperature surfaces (b). The total H_2O mass in the convective and non-convective air are shown as the dashed blue and cyan lines, respectively, and the total H_2O mass in the layer is shown in the solid red line. The fractional amount of the layer containing a cloud concentration of at least 0.1 g/kg is shown in black (convective fraction, %).

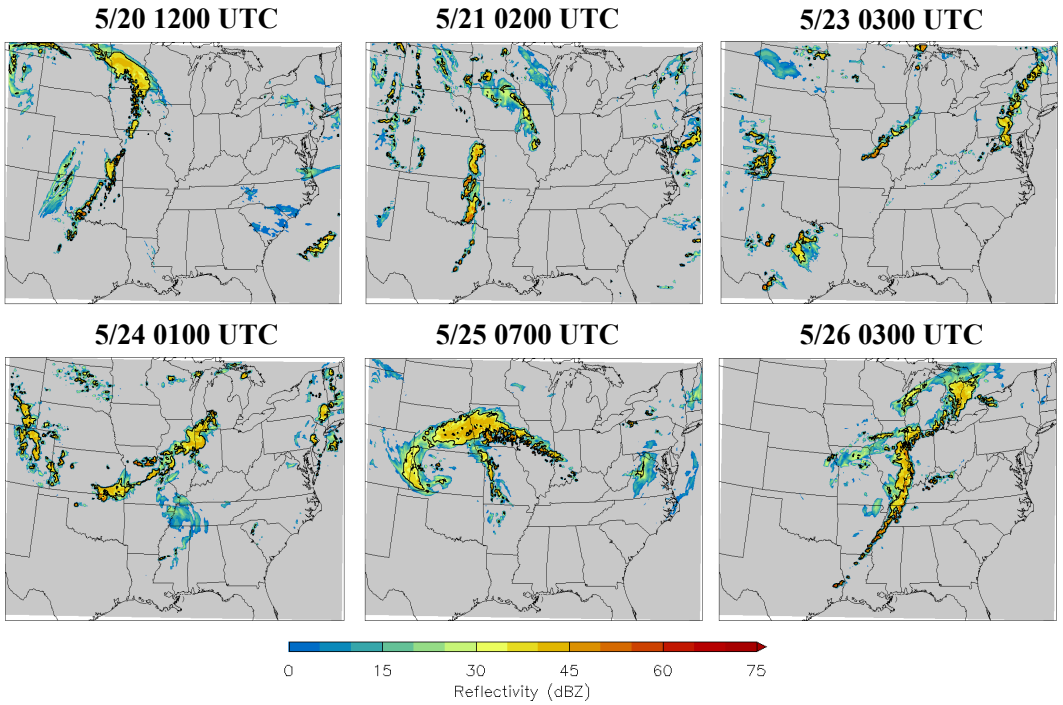

Figure 56. Reflectivity fields at a constant altitude of 5 km for the six main convective events of the May 2011 period. The black line shows the 30 dBZ reflectivity contour.

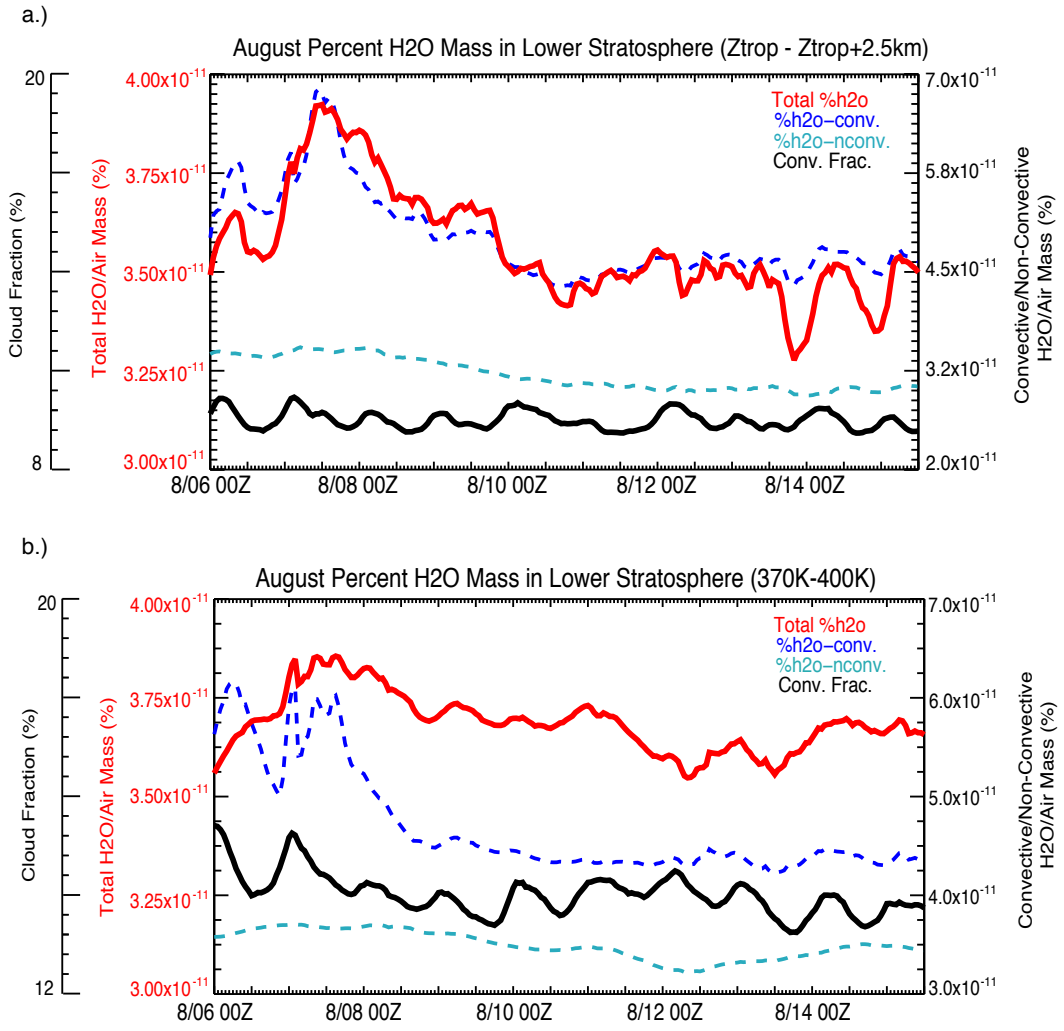

Figure 57. As in Figure 55, but for August 2013. Note that the potential temperature layer is defined as being between 370 K and 400K.

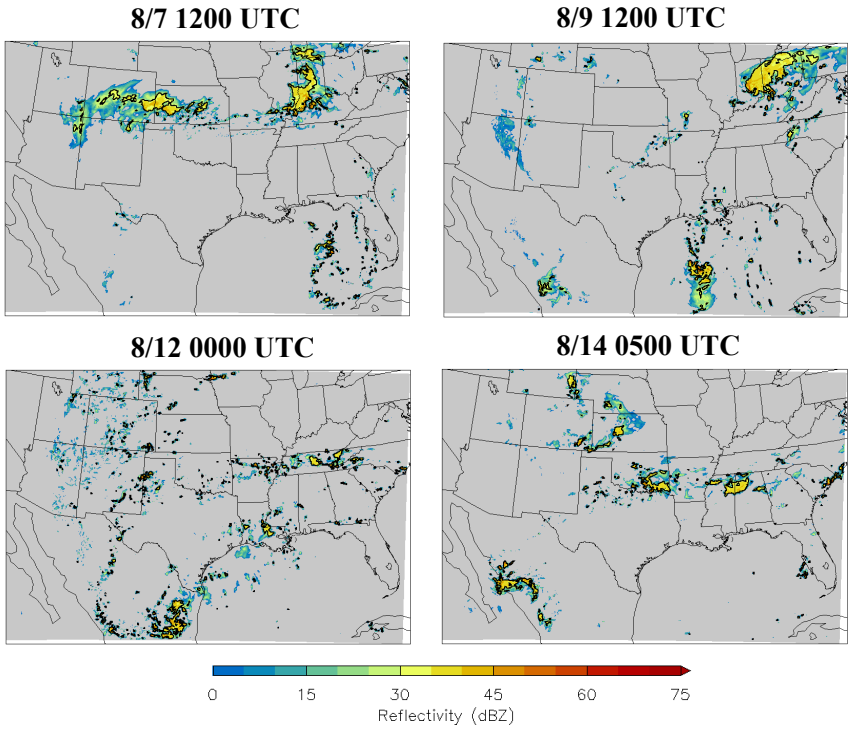

Figure 58. As in Figure 56, but for four selected times during the August 2013 simulation period.

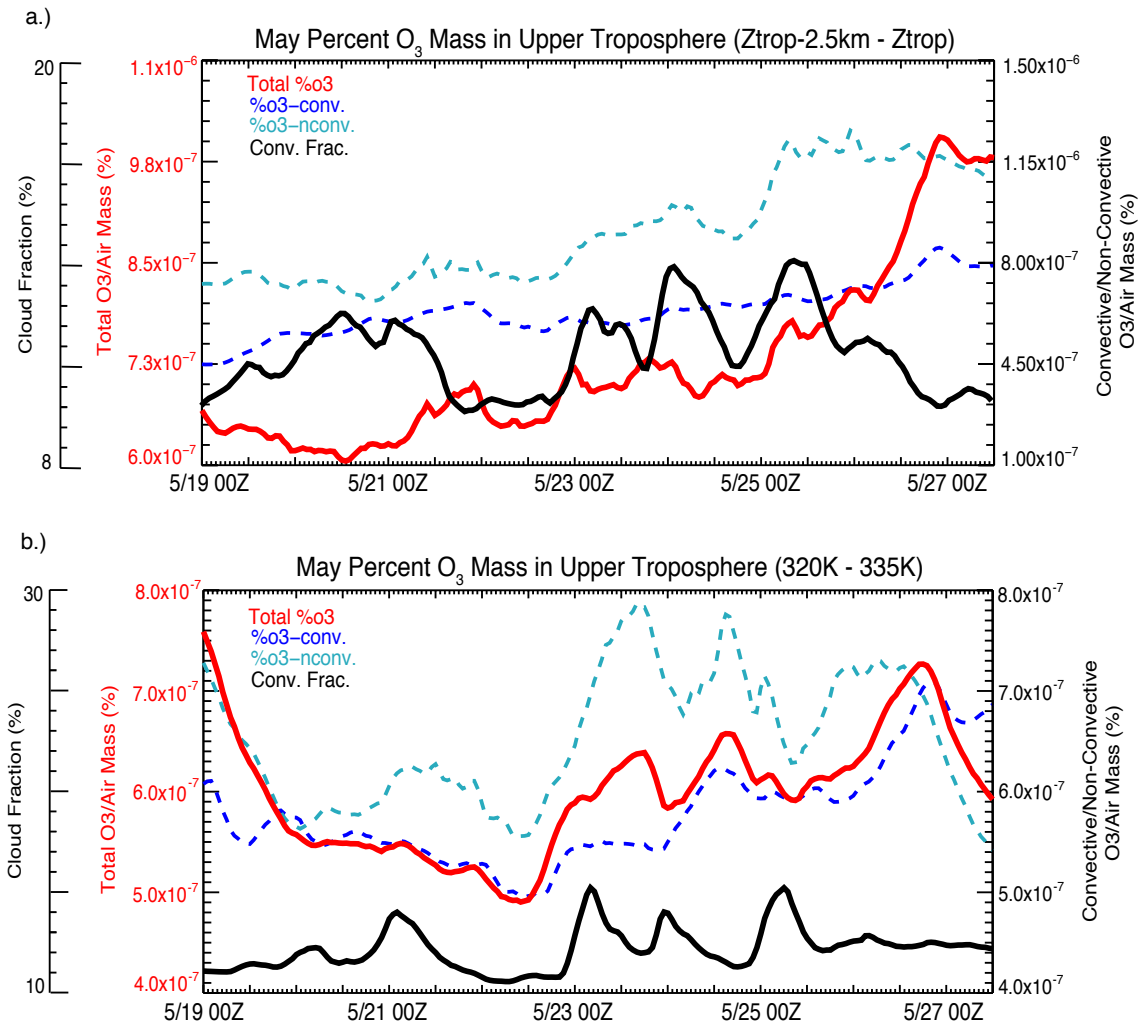

Figure 59. As in Figure 55, but for O_3 in the upper troposphere. The upper troposphere layer is defined in tropopause relative altitude coordinates as the layer between the tropopause and 2.5 km below the tropopause. The potential temperature limits are 320 K – 335 K.

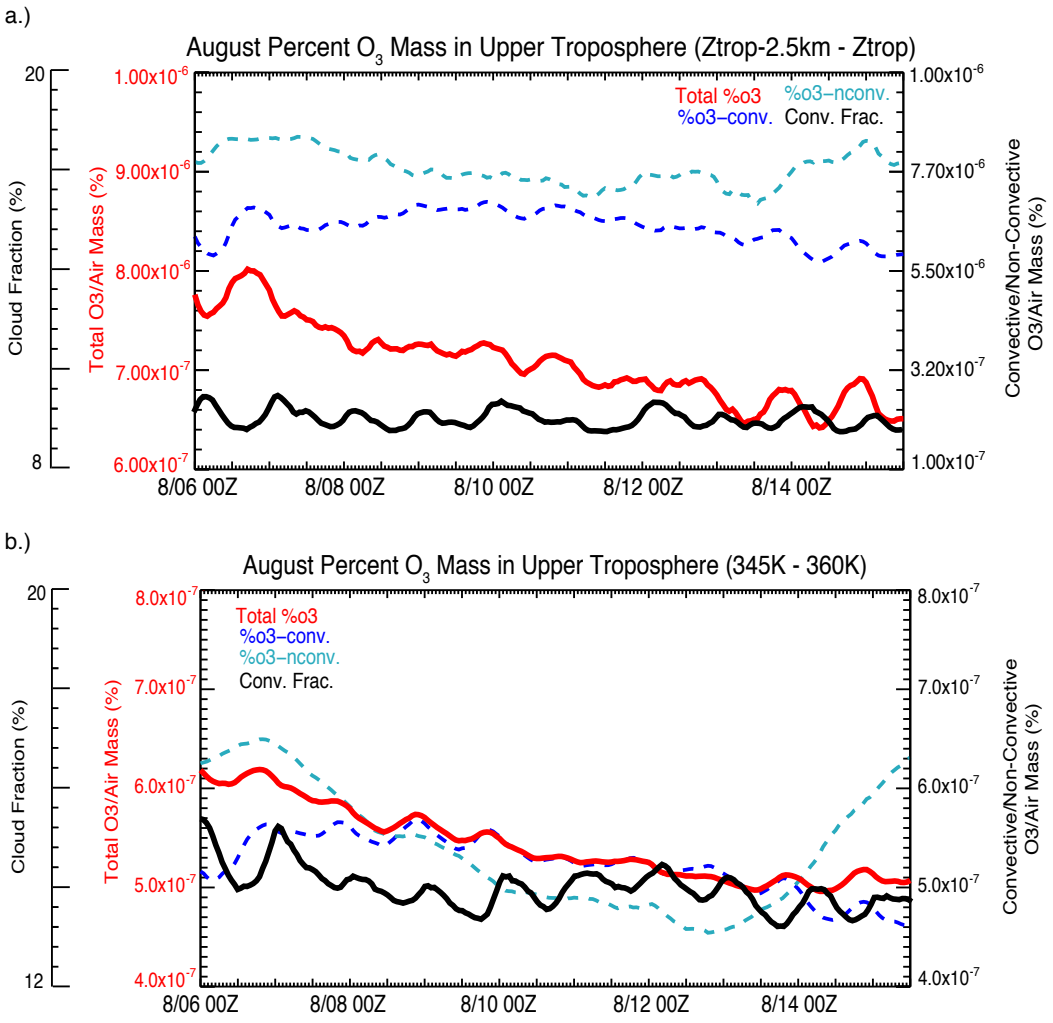

Figure 60. As in Figure 59, but for August 2013. Note that the potential temperature layer is defined as being between 345K and 360K.

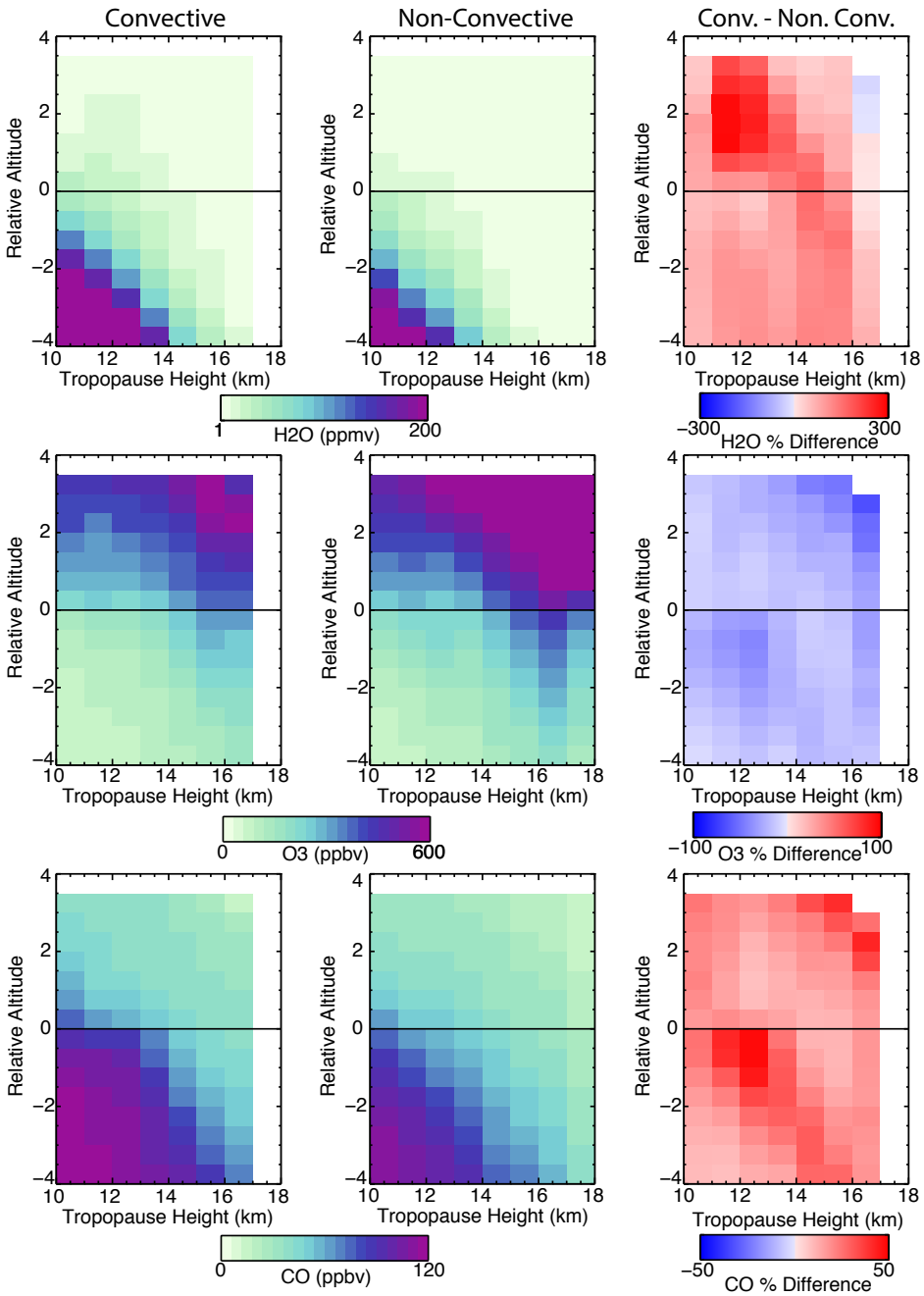

Figure 61. Binned profiles of H_2O (top), O_3 (middle), and CO (bottom) for convective (left) and non-convective (middle), and the percent difference (right) for May 2011.

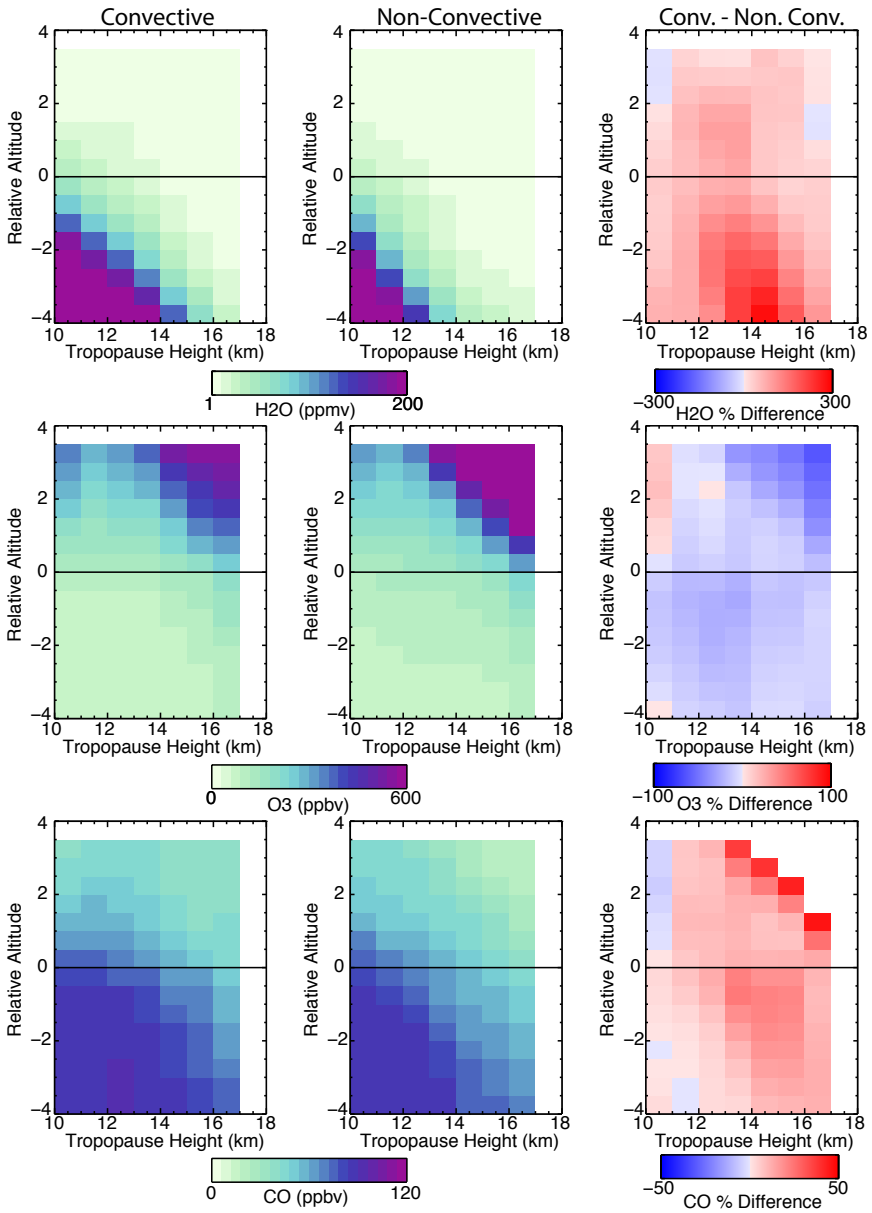

Figure 62. As in Figure 61, but for August 2013.

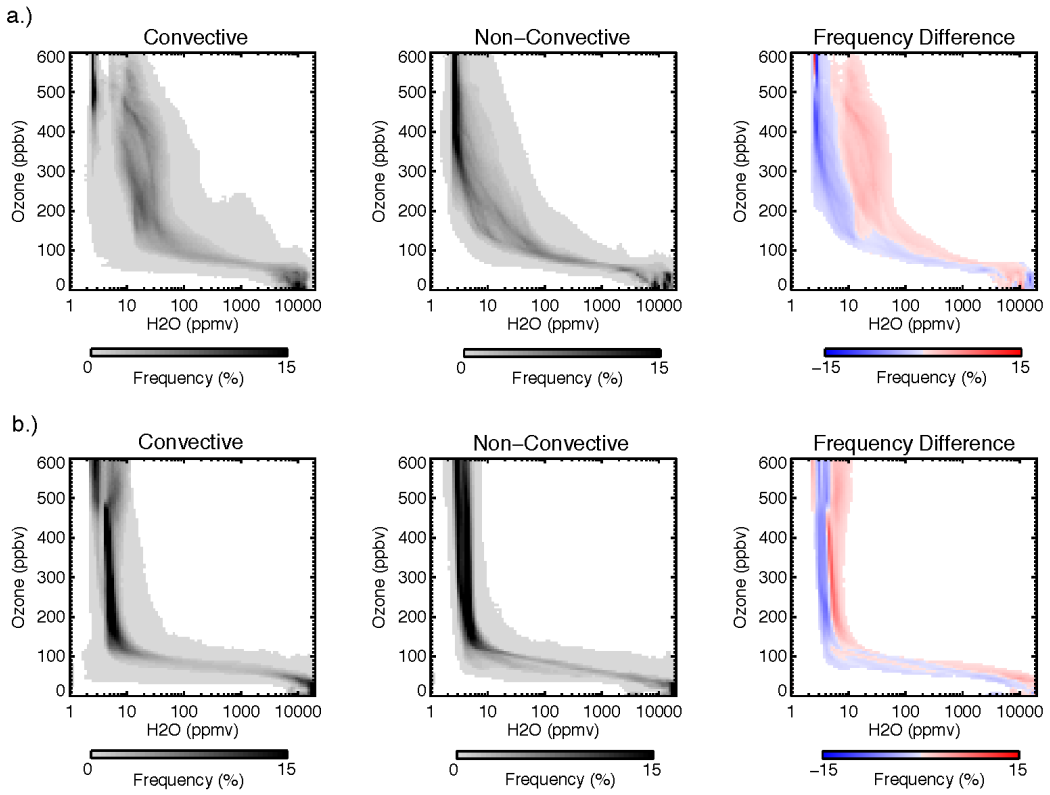

Figure 63. H_2O – O_3 tracer correlations for May (a) and August (b). Tracer-tracer correlations are shown for convective (left) and non-convective (middle) air and the difference (right). The correlations are binned and shaded by the frequency of observations in each bin.

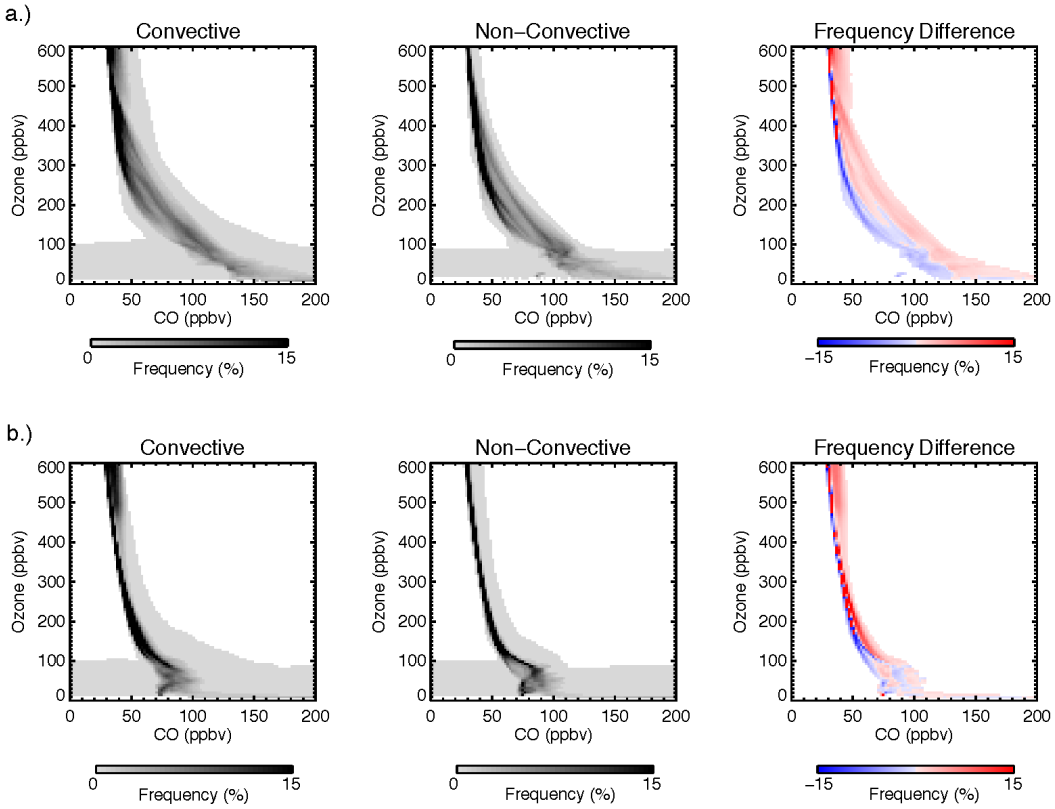

Figure 64. As in Figure 63, but for CO-O_3 tracer correlations.

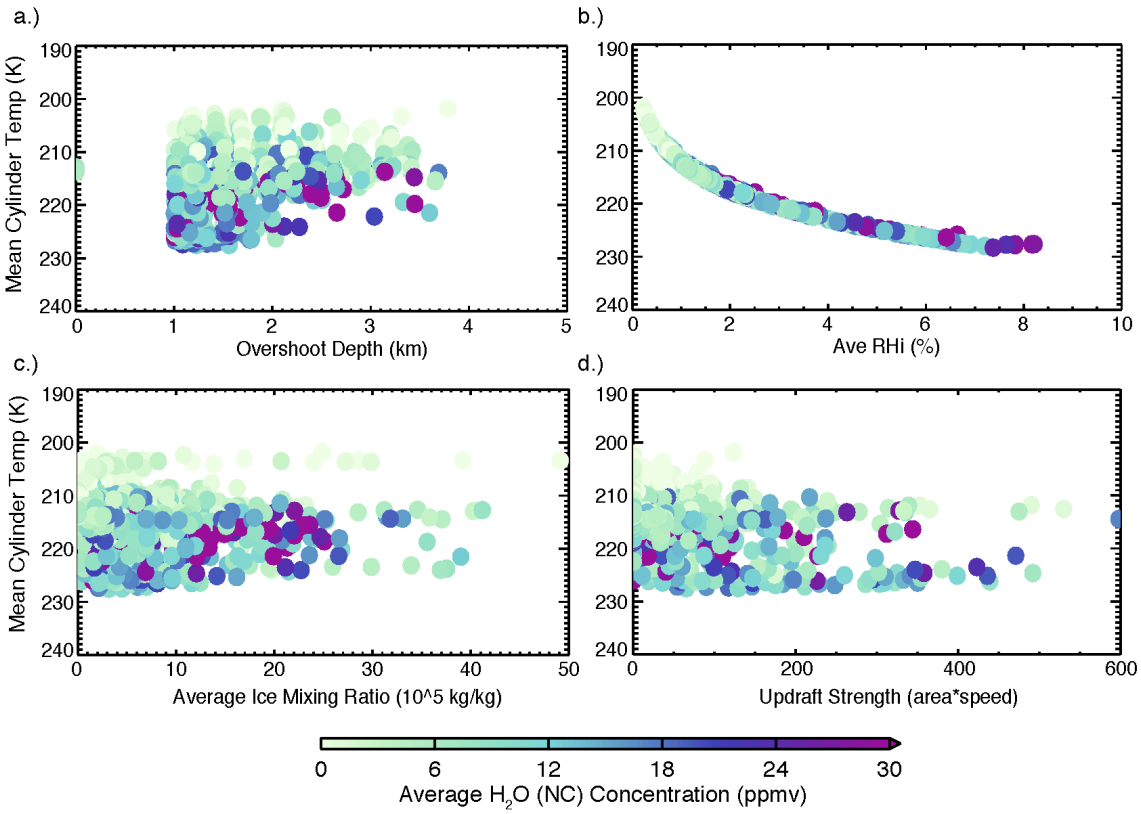

Figure 65. Scatterplots of the mean temperature in the cylinder, mean H_2O concentration (color fill), and overshooting depth (a), RHi (b), ice mass mixing ratio (c), and updraft strength (d) for storms during the May 2011 period.

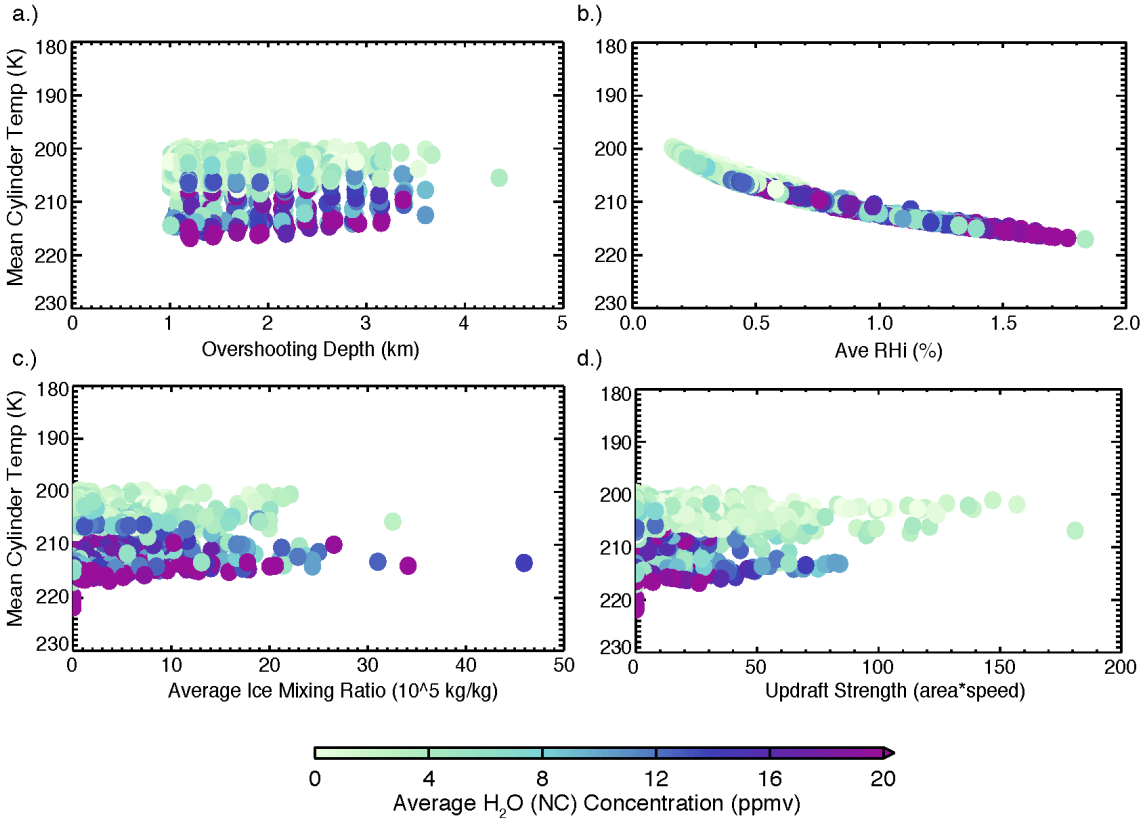

Figure 66. As in Figure 65, but for August 2013.

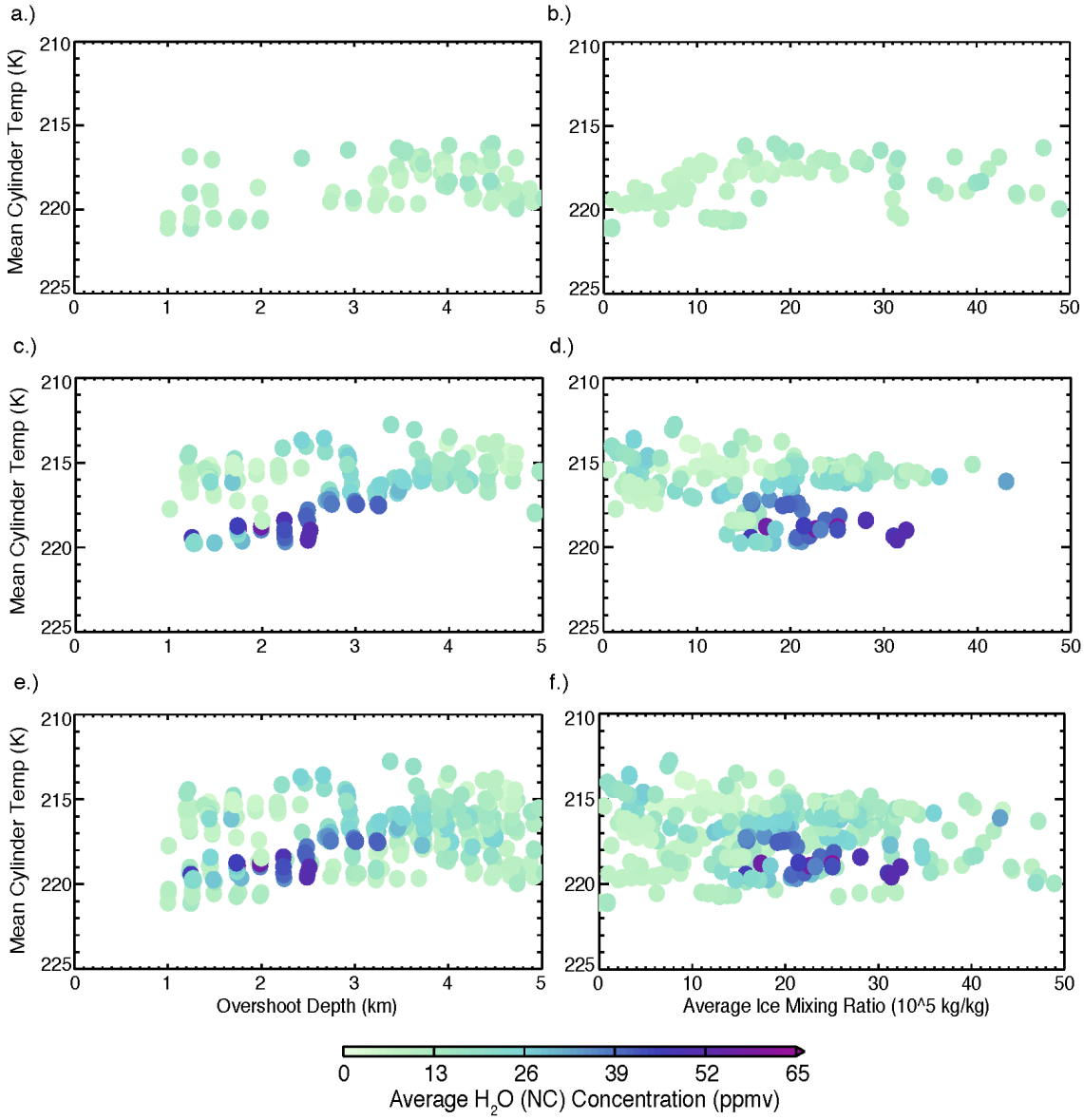

Figure 67. Scatterplots of mean temperature in the cylinder, mean H_2O concentration (color fill), and overshooting depth (a, c, e) and ice mass mixing ratio (b, d, f) for three time periods: 2250-0040 UTC, representing an earlier stage in the MCS's evolution (a, b), 0205-0350 UTC, representing a later stage in the MCS's evolution (c, d), and the 2250-0350 UTC period (e, f).

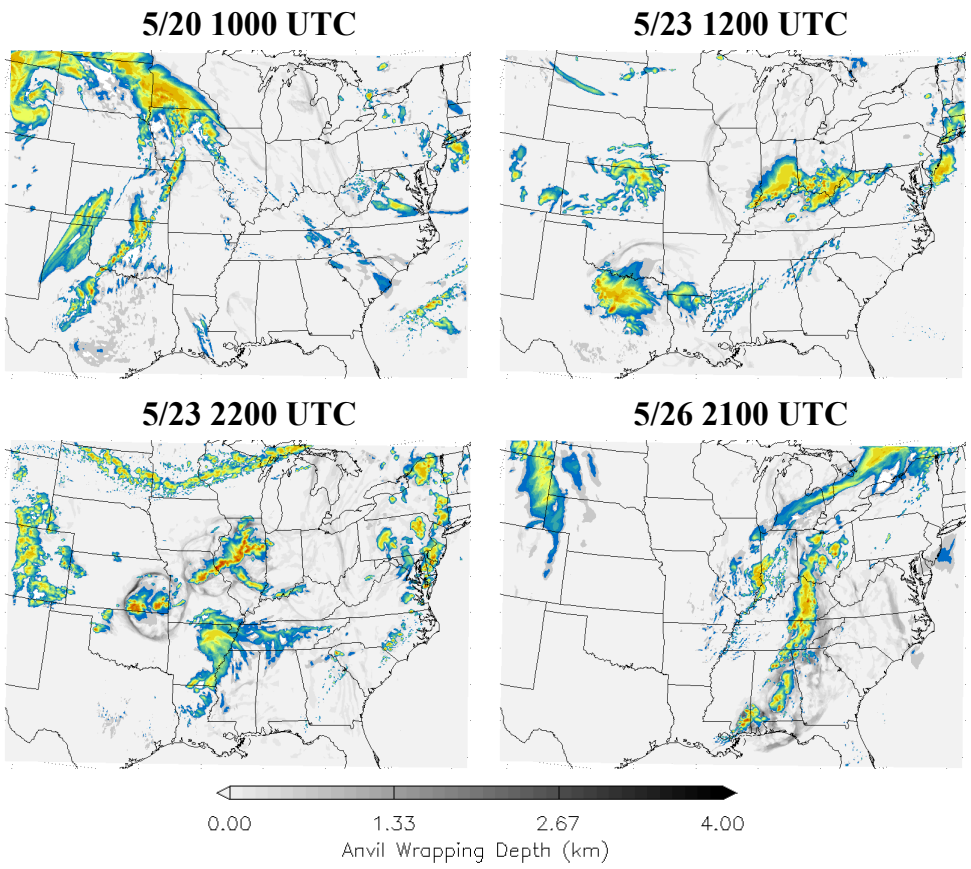

Figure 68. 5 km constant altitude reflectivity fields for several times during the May 2011 period. The grayscale shows regions that have been flagged for anvil wrapping and the estimated depth of transport.

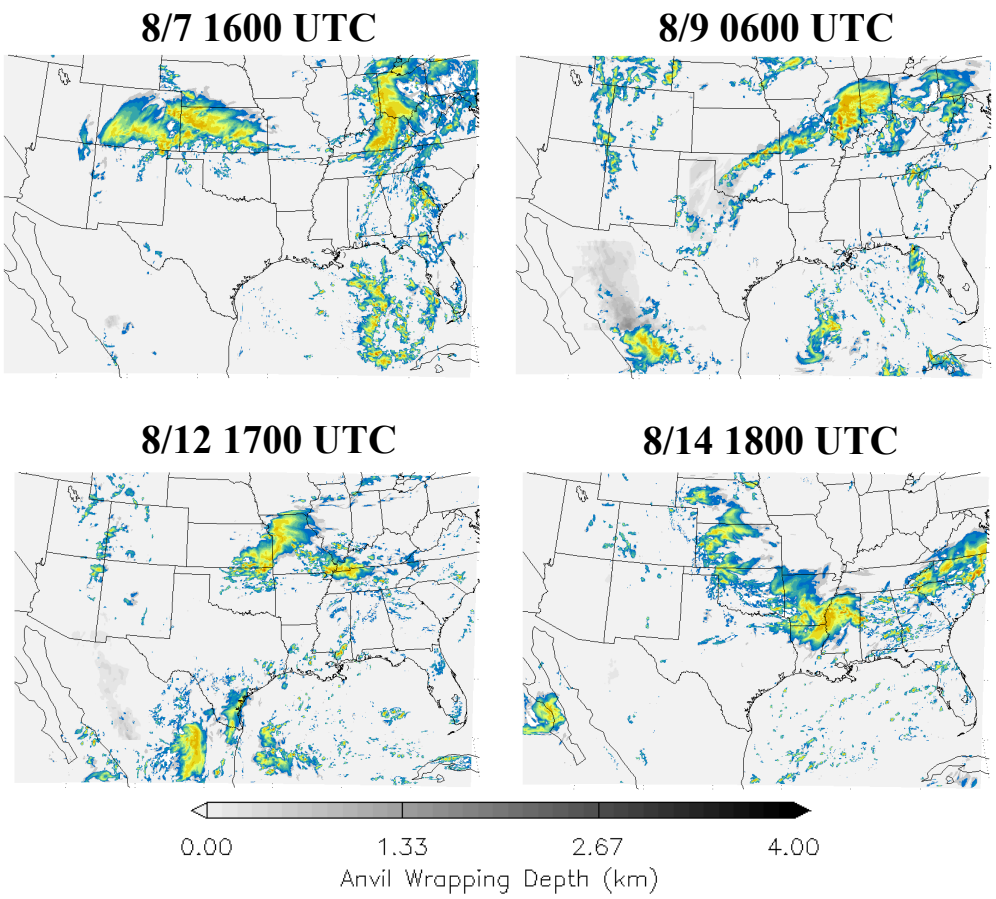

Figure 69. As in Figure 68, but for August 2013.

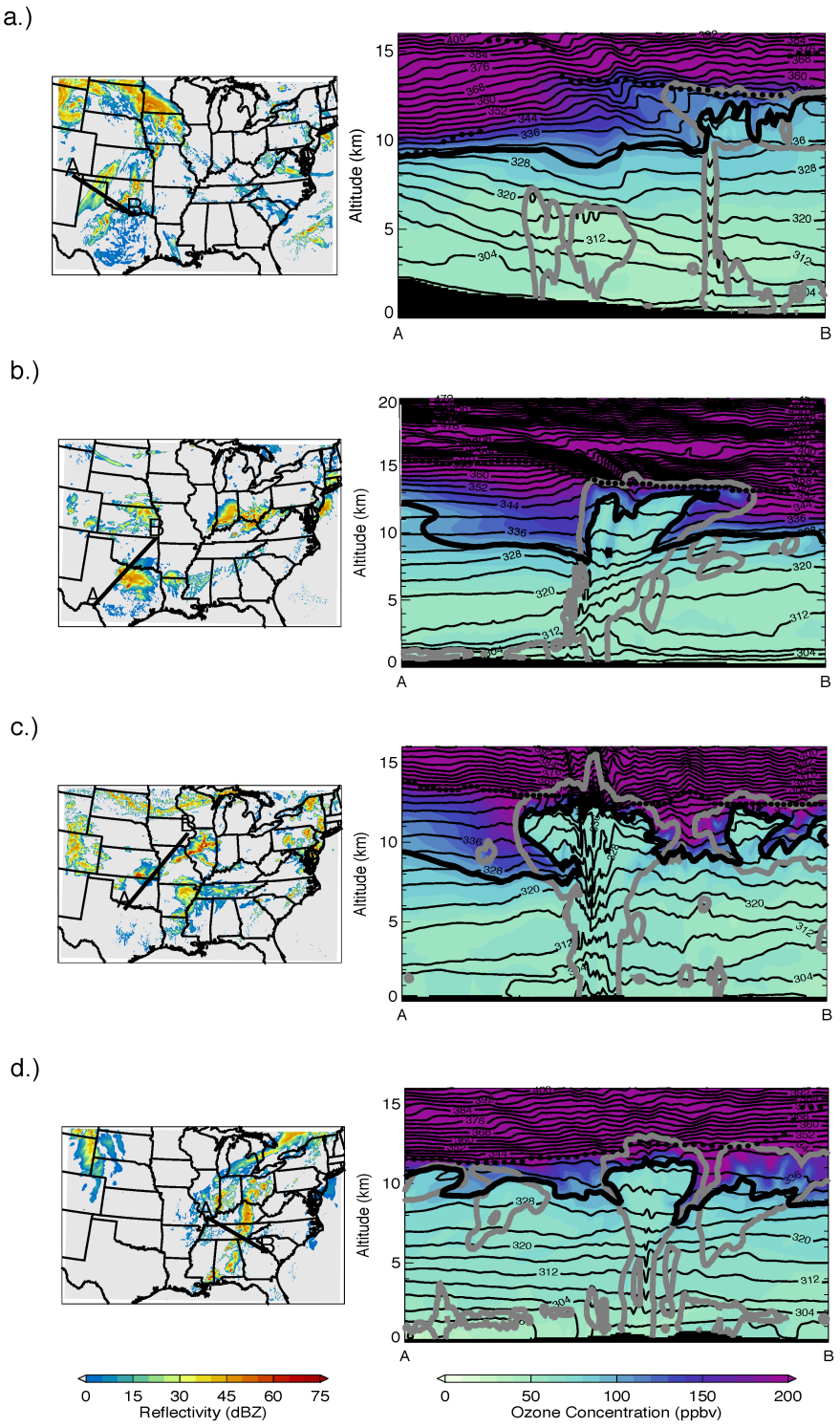

Figure 70. Vertical cross sections of O_3 (color fill) and potential temperature (thin black lines) for several times where anvil wrapping was identified for the May 2011 period: 20 May 1000 UTC (a), 23 May 1200 UTC (b), 23 May 2200 UTC (c), and 26 May 2100 UTC (d). The black dots show the location of the LRT and the gray line shows the cloud boundary. The thick black line shows O_3 contours at 100 ppb, 125 ppb and 150 ppb.

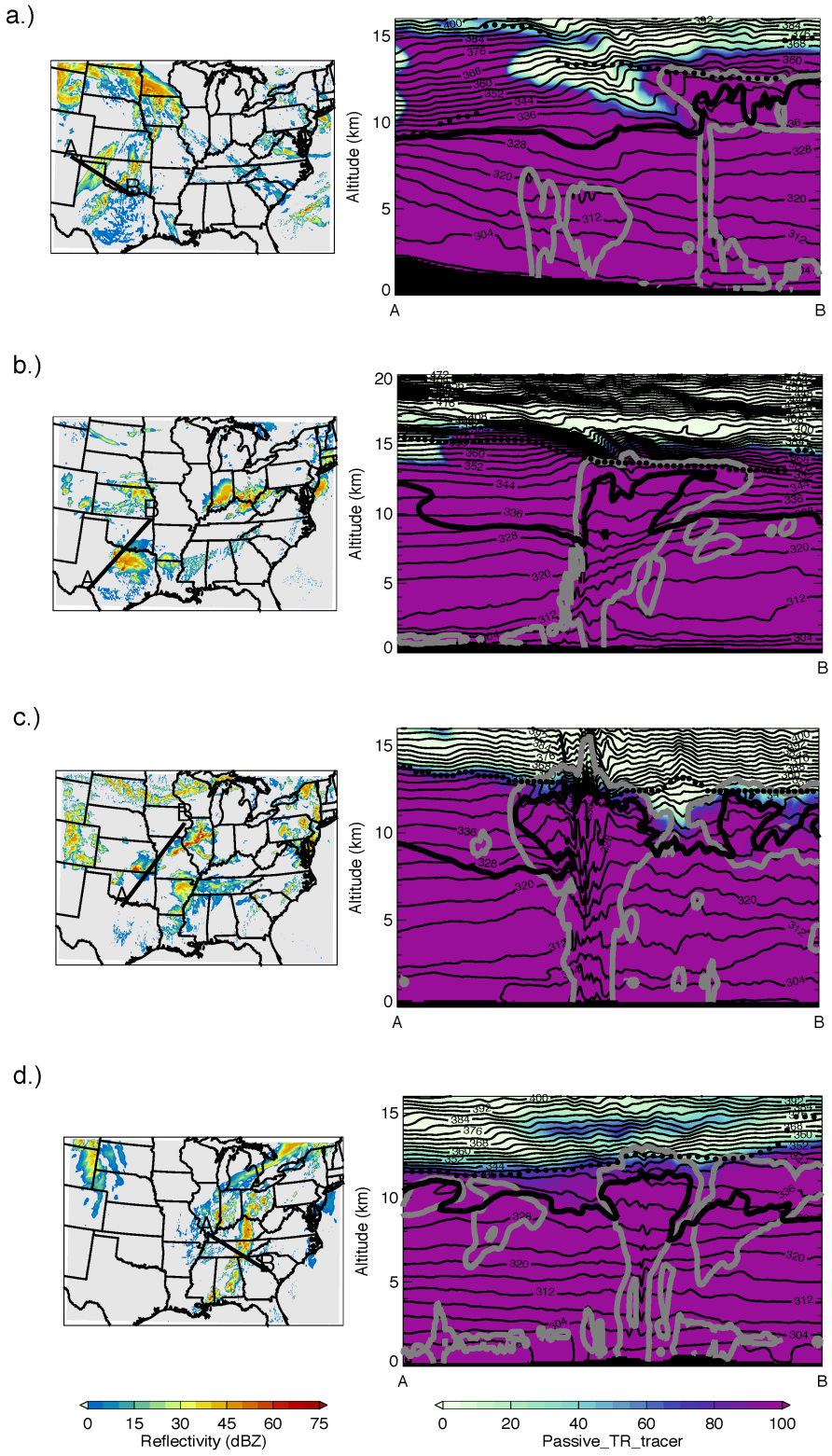

Figure 71. As in Figure 70, but for vertical cross sections of a passive troposphere tracer.

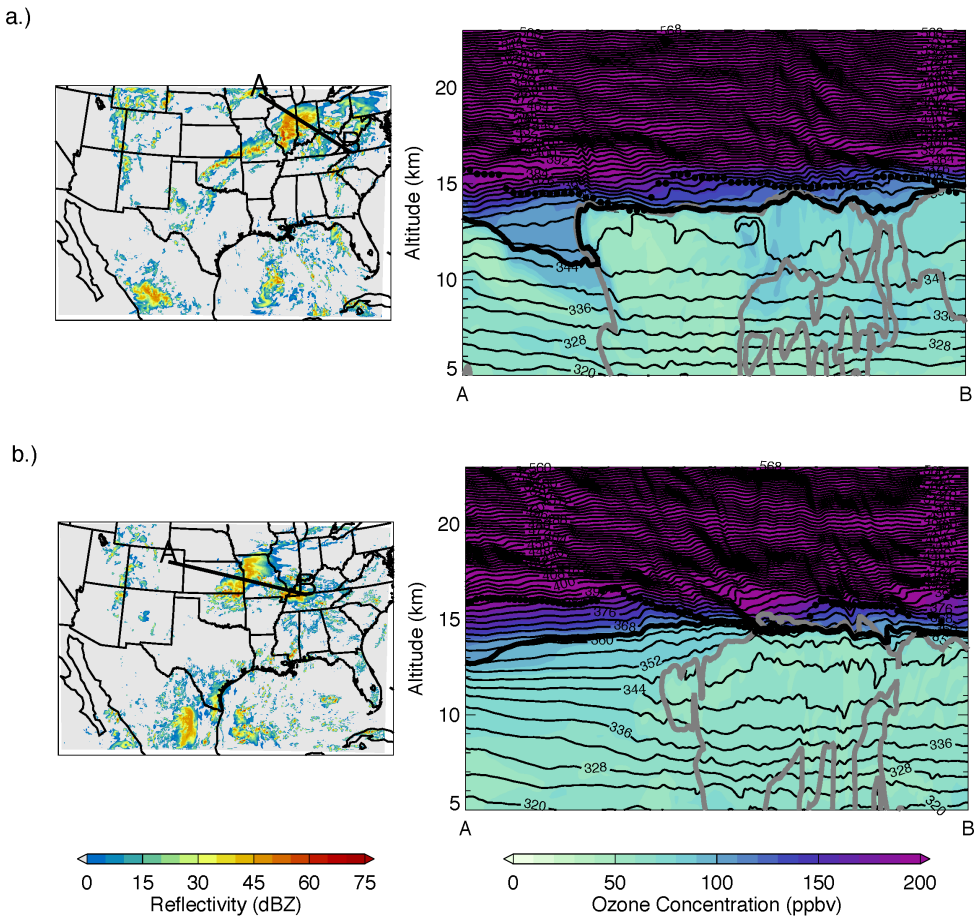

Figure 72. As in Figure 70, but for two cases in August 2013: 9 August 0600 UTC (a) and 12 August 1700 UTC (b).

Chapter 5
Conclusions and Future Work

WRF-Chem simulations were performed to assess the impact of tropopause-penetrating convection on the chemical composition of the upper troposphere and lower stratosphere. Simulations were performed to determine the model sensitivity to simulating these types of storms and transport, the dynamical mechanisms responsible for transport, and the broad impacts that convection has on UTLS composition. Sensitivity tests revealed that WRF-Chem simulations are most sensitive to the choice in BMP, but there was little sensitivity to the chosen chemical mechanism and PBL scheme. As expected, there is measurable sensitivity of the organization and vertical extent of simulated convection to the choice of BMP. Furthermore, the simulations in this study showed that convectively injected water into the stratosphere was also sensitive to the choice of BMP.

High-resolution simulations of STT around the anvil of an MCS indicate that the main contributors to this process of STT are i) the intense convective motions and mass conservation that drive the initial downwelling of air outside of the anvil, and ii) differential advection between outflow air and air outside of the cloud that create an eddy circulation near the anvil edge, leading to wrapping of air down and under the anvil cloud. Trajectory calculations indicate that the wrapped air in WRF simulations was mainly tropopause transition layer air, with air originating above the LRT remaining in the stratosphere. Simulated O_3 in the wrapping feature was lower than observations. Since the initial modeled O_3 was actually higher in the UTLS compared to observations, this suggests that the model did not fully simulate the transport process.

Overall, springtime convection has the largest effect on H_2O mixing ratios in the LS. Locally, convection can increase LS H_2O by ~300% relative to the background (non-convective) environment. Furthermore, large convective events are capable of increasing the LS mean H_2O mixing ratio by 20-30%. Assuming a background LS H_2O mixing ratio of 5 ppmv, LS H_2O mixing ratios can be 10-15 ppmv higher in convectively influenced air, and the effects of convection can raise the H_2O mixing ratio over the US LMS by 1 ppmv. The effects of convection on LS H_2O are greatest in regions with lower tropopause

altitudes, due to the warmer temperatures at the tropopause, at which the air is highly subsaturated with respect to ice. While summertime convection does modify the LS locally, the overall changes are much smaller than those in springtime convection.

Springtime convection also has a larger effect than summertime convection on O_3 and CO in the upper troposphere. Since changes in O_3 and CO are mainly due to air mass transport, this suggests that little air from the boundary layer and lower troposphere is transported to the lower stratosphere. Furthermore, the difference between the layers of maximum H_2O and O_3/CO impact further suggest that changes in LS H_2O are primarily driven by ice crystal sublimation and not air mass transport. Concentrations of O_3 (CO) are lower (higher) in convective air compared to non-convective air because convective air originates in the boundary layer and lower troposphere where concentrations of O_3 (CO) are lower (higher). UT concentrations of O_3 (CO) are higher (lower) in the non-convective air, and argued to be a product of descending transition layer air along the periphery of the convective systems. This is further supported by the O_3 mass budget calculations, which showed the largest changes in O_3 mass are consistent with increases in non-convective O_3 mass following a convective event. Objective analyses to track STT of O_3-rich air revealed that downward transport does frequently occur around large convective systems in lower tropopause altitude environments. This is also supported by the binned vertical profiles that showed the largest difference in UT O_3 to be in environments with tropopause heights between 11 and 13 km. As such, several cases in May showed downward transport, but none did in August. Since mass-continuity has been proposed as the primary driver of subsidence [Chapter 3; *Phoenix et al*., 2019], the storm's ability to meet the tropopause with sufficient force is necessary to induce such circulations. Overall, the primary difference between springtime and summertime environments is the height of the tropopause, which suggests that the tropopause height controls the extent of the impact that overshooting convection has on the UTLS composition.

Given the conclusions of *Lacis et al.* [1990] and *Solomon et al.* [2010], these simulations suggest that convective transport and mixing is capable of increasing the surface radiative forcing over much of the US. The simulated increases in LS H_2O and UT O_3 could potentially lead to more tropospheric warming during periods of active

convection (e.g., springtime). However, since the convectively-induced changes in LS H_2O and UT O_3 only last ~12 hours (based on the analysis presented in section 4.3.1), it is unclear to what extent convection will have an affect on the radiation budget. Future studies should aim to assess the net effect of convection on the radiative budget and expected changes in tropospheric temperatures, especially if deep convective systems are expected to be more prevalent in the future.

While this study sheds light on several important impacts of convection on UTLS composition, there were several limitations that could be improved upon in future studies. Since the model does not completely simulate STT, future model simulations should be performed to test the sensitivity of cross-tropopause transport to vertical resolution in the UTLS and other model design choices. STT simulated on the 2.5 km horizontal grid and 500 m horizontal grid was comparable, suggesting that this type of transport is not sensitive to horizontal resolution. However, as suggested by *Homeyer* [2015], stratosphere-troposphere exchange may be more sensitive to the vertical resolution of the model. Furthermore, the sensitivity tests conducted in Chapter 2 [*Phoenix et al., 2017*] were evaluated with three cases in which high H_2O mixing ratios were observed in the stratosphere, but were not accompanied by significant downward transport around the thunderstorm anvil. It is possible that the PBL scheme used in this study does not best represent the STT that was the target of this high-resolution simulation. Since the YSU PBL scheme is a non-local scheme, it determines the strength of vertical mixing throughout the model depth and perhaps underrepresented mixing in the UTLS region. Sensitivity tests of PBL schemes for the 30 May 2012 event should be done to evaluate this hypothesis. Additionally, several unusual features in the chemical fields (e.g., O_3, CO) were observed in the model, especially near the domain boundaries, which influenced the results of the UT O_3 mass calculations. The elimination of these issues will allow simulations of convective STE to more clearly demonstrate the impacts of convection.

While this study attempted to assess the impact of convection on UTLS composition, it was difficult to determine the relative importance of different storms, due to the temporal resolution of the output files and continuous occurrence of convection. A secondary goal of this study was to assess the relative importance of storm characteristics

(e.g., organization, strength) and environmental characteristics (e.g., tropopause height, gravity wave breaking) to the resulting impact on UTLS composition. However, accurately tracking the evolution of these features and relating them to the resulting chemical impact requires analysis of finer temporal output (~5 minutes) than that used here (hourly). Additionally, given the different interactions between the storm and environment, it is difficult to sort out the competing effects that contribute to changes in the UTLS chemical composition (e.g., tropopause height, updraft size, overshooting depth). A proper method of studying this question would likely require a controlled environment such as one obtained in an idealized modeling framework.

The attempt to relate convective events to changes in H_2O and O_3 mass (as presented in section 4.3.1) was complicated by the continuous occurrence of convection throughout the simulation. To properly assess the long term impact of convection, a perturbation study that holds the atmospheric dynamics fixed but allows convection to vary would likely provide a better understanding on how the chemical composition evolves during and after a series of convective events. Lastly, this study highlighted the complications in assessing cross-tropopause transport in an environment in which the LRT is frequently perturbed. Since cross tropopause-transport is best assessed after convection decays, and since convection was always active during the simulation period, it is unclear to what degree convection impacts the UTLS composition in this study. Cross tropopause transport of H_2O is easier to assess in these simulations since transport of H_2O into the LMS results from mixing of stratospheric air with the overshooting top and the resulting sublimation of ice crystals, which is most likely an irreversible process since the potential temperature of the air parcels would be raised from such mixing. However, transport of CO and O_3 are harder to assess since they are mainly driven by air mass mixing, which is potentially underrepresented in these simulations. The degree to which O_3 and CO were irreversibly mixed is uncertain.

References

Ackerman, S. A. (1996), Global satellite observations of negative brightness temperature differences between 11 and 6.7 μm, *J. Atmos. Sci., 53,* 2803-2812.

Ackermann, I. J., H. Hass, M. Memmesheimer, A. Ebel, F. S. Binkowski, and U. Skankar (1998), Modal aerosol dynamics model for Europe: Development and first applications, *Atmos. Environ., 32*(17), 2981-2999.

Ahmadov, R., et al. (2012), A volatility basis set model for summertime secondary organic aerosols over the eastern United States in 2006, *J. Geophys. Res. Atmos., 117*, D06301.

Anderson, J. G., D. M. Wilmouth, J. B. Smith, and D. S. Sayres (2012), UV dosage levels in summer: Increased risk of ozone loss from convectively injected wayer vapor, *Science, 337*(6096), 835 – 839.

Ansong, J. K. and B. R. Sutherland (2010), Internal gravity waves generated by convective plumes., *J. Fluid Mech.,* 648, 405-434.

Apel, E. C., and Coauthors (2015), Upper tropospheric ozone production from lightning NOx-impacted convection: Smoke ingestion case study from DC3 campaign, *J. Geophys. Res. Atmos,.,* 120, 2505-2523, doi:10.1002/2014JD022121.

Assman, R. (1902), Über die Existenz eines warmen Lufttromes in der Höhe von 10 bis 15 km, *Sitzber. Königl. Preuss. Akad. Wiss. Berlin, 24*, 495-504.

Barth, M. C., S.-W. Kim, W. C. Skamarock, A. L. Stuart, K. E. Pickering, L. E. Ott (2007), Simulations of the redistribution of formaldehyde, formic acid, and peroxides in the 10 July 1996 Stratospheric-Tropospheric Experiment: Radiation, Aerosols, and Ozone deep convection strom, *J. Geophys. Res. Atmos., 112*(D13), doi:10.1029/2006JD008046.

Barth, M. C., J. Lee, A. Hodzic, G. Pfister, W. C. Skamarock, J. Worden, J. Wong, and D. Noone (2012), Thunderstorms and upper troposphere chemistry during the early stages of the 2006 North American Monsoon., *Atmos. Chem. Phys., 12*(22).

Barth, M. C., et al. (2015), The Deep Convective Clouds and Chemistry (DC3) field campaign., *Bull. Am. Meteorol. Soc., 96*.

Bedka, K. M., Brunner, J., Dworak, R., Feltz, W., Otkin, J., and Greenwald, T., (2010), Objective satellite - based overshooting top detection using infrared window channel brightness temperature gradients, *J. Appl. Meteorol. Climatol.*, *49*, 181–202.

Bedka, K. M. and K. Khlopenkov (2016), A propabilistic multispectral pattern regonition method for detection of overshooting cloud tops using passive satellite imager observations, *J. Appl. Meteorl. Clim.,* doi:10.1175/JAMC-D-15-0249.1.

Bela, M. M., et al. (2016), Wet scavenging of soluble gases in DC3 deep convective storms using WRF‐Chem simulations and aircraft observations. *J. Geophys. Res. Atmos., 121*(8), 4233-4257.

Berendes, T. A., et al. (2008), Convective cloud identification and classification in daytime satellite imagery using standard deviation limited adaptive clustering, *J. Geophys. Res., 113*(D20207), doi:10.1029/2008JD010287.

Bethan, S., G. Vaughan, and S. J. Reid (1996), A comparison of ozone and thermal tropopause heights and the impact of tropopause definition on quantifying the ozone content of the tropopause, *Q. J. R. Meteorol. Soc., 112,* 929-944.

Bigelbach, B. C., G. L. Mullendore, and M. Starzec (2014), Differences in deep convective transport characteristics between quasi-isolated strong convection and mesoscale convective systems using seasonal WRF simulations, *J. Geophys Res. Atmos., **119**,* 11,445 – 11,455.

Birner, T., A. Dornbrack, and U. Schumann (2002), How sharp is the tropopause at midlatitudes? *Geophys. Res. Lett., 29*(14), 1700, doi:10.1029/2002GL015142.

Bradshaw, N. G., et al. (2002), Tracer filamentation generated by small-scale Rossby wave breaking in the lower stratosphere, *J. Geophys. Res., 107*(D23), 4689.

Brewer, A. W. (1949), Evidence for a world circulation provided by the measurements of helium and water vapour distribution in the stratosphere, *Q. J. R. Meteorol. Soc*. *75*, 351, doi:10.1002/qj.49707532603.

Brighton, P.W.M. (1978), Strongly stratified flow past three-dimensional obstacles, *Q.J.R.M.S, 104* (440), doi:10.1002/qj.49710444005.

Brooks, H. E. (2013), Severe thunderstorms and climate change, *Atmos. Res., 123*,129-138.

Browell, E. V., et al. (1996), Ozone and aerosol distributions and air mass characteristics over the South Atlantic Basin during the burning season, *J. Geophys. Res., 101*(D19), 24043-24068.

Chameides, W. L. (1978), The photochemical role of tropospheric nitrogen oxides, *Geophys. Res. Lett., 5*(1),17-20.

Chin, M., R. B. Rood, S-J. Lin, J-F. Muller, and A. M. Thompson, 2000a: Atmospheric sulfur cycle simulated in the global model GOCART: Model description and global properties. *J. Geophys. Res*, *105*, 24671–24687

Cohen, A. E., S. M. Cavallo, M. C. Coniglio, and H. E. Brooks (2015), A review of planetary boundary layer parameterization schemes and their sensitivity in simulating southeastern US cold season severe weather environments. *Wea. Forecasting, 30*(3), 591-612.

Coniglio, M. C., J. Correia Jr, P. T. Marsh, and F. Kong (2013), Verification of convection-allowing WRF model forecasts of the planetary boundary layer using sounding observations. *Wea. Forecasting, 28*(3), 842-862.

Cooney, J. W., K. P. Bowman, C. R. Homeyer, and T. M. Fenske (2018), Ten year analysis of tropopause-overshooting convection using GridRad data, *J. Geophys. Res.: Atmos., 123*(1), http://doi.org/10.1002/2017JD027718.

Cooper, O. R., et al. (2006), Large upper tropospheric ozone enhancements above midlatitude North America during summer: In situ evidence from the IONS and MOZAIC ozone measurement network, *J. Geophys. Res.*, *111*(D24S05), doi:10.1029/2006JD007306.

Cooper, O. R., et al. (2007), Evidence for a recurring eastern North America upper t ropospheric ozone maximum during summer, *J. Geophys. Res.*, *112*(D23304), doi:10.1029/2007JD008710.

Crum, T. D., and R. L. Alberty (1993), The WSR-88D and WSR-88D operational support facility, *Bull. Amer. Meteorol. Soc., 74*(9), 1669 – 1687.

Crutzen, P. (1973), A discussion of the chemistry of some minor constituents in the stratosphere and troposphere, *Pure and Applied Geophysics, 106*(1), 1385-1399.

Danielsen, E. F. (1964), Project Springfield Report, *Tech. Rep. 1517,* 110 pp., Defense At. Supp. Agency, Washington, D. C.

Danielsen, E. F. (1968), Stratospheric - tropospheric exchange based on radioactivity, ozone and potential vorticity, *J. Atmos. Sci.*, *25*, 502– 518.

Davis, S. M., A. G. Hallar, L. M. Avallone, and W. Engblom (2007), Measurement of total water with a tunable diode laser hygrometer: Inlet analysis, calibration procedure, and ice water content determination, *J. Atmos. Oceanic Technol.*, *24*(3), 463–475, doi:10.1175/JTECH1975.1.

Dawson, D. T., E. R. Mansell, Y. Jung, L. J. Wicker, M. R. Kumjian, and M. Xue, 2014: Low-level ZDR signatures in supercell forward flanks: The role of size sorting and melting of hail, *J. Atmos. Sci.*, *71*, 276-299, doi:10.1175/JAS-D-13-0118.1.

de Bort, L. T. (1902), Variations de la temperature de l'air libre dans la zone comprise entre 8 km et 13 km d'altitude, *C. R. S. Acad. Sci. Paris, 134,* 987-989.

Dee, D. P., et al. (2011), The ERA-Interim reanalysis: Configuration and performance of the data assimilation system, *Q. J. R. Meteorol. Soc., 137,* 533-597, doi:10.1002/qj.828.

Dickerson, R. R., et al. (1987), Thunderstorms: An important mechanism in the transport of air pollutants, *Science*, *235*, 460– 465.

Diskin, G. S., J. R. Podolske, G. W. Sachse, and T. A. Slate (2002), Open-path airborne tunable diode laser hygrometer, *Proc. SPIE*, *4817*, 196–204, doi:10.1117/12.453736.

Dobson, G. M. B., A. W. Brewer, and B. Cwilong (1946), The meteorology of the stratosphere, *Proc. R. Soc. London Ser. A, 185,* 144-175.

Dorsi, S. W., L. E. Kalnajs, D. W. Toohey, and L. M. Avallone (2014), A fiber-coupled laser hygrometer for airborne total water measurement, *Atmos. Meas. Tech.*, *7*, 215–223, doi:10.5194/amt-7-215-2014.

Dvortsov, V. L., M. A. Geller, S. Solomon, S. M. Schauffler, E. L. Atlas, and D. R. Blake (1999), Rethinking reactive halogen budgets in the midlatitude lower stratosphere, *Geophys. Res. Lett., 26*(12), 1699-1702.

Ertel, H. (1942), Ein neuer hydrodynamischer wirbelsatz, *Met. Z., 59,* 271-281.

Emmons, L. K., Walters, S., Hess, P. G., Lamarque, J.-F., Pfister, G. G., Fillmore, D., Granier, C., Guenther, A., Kinnison, D., Laepple, T., Orlando, J., Tie, X., Tyndall, G., Wiedinmyer, C., Baughcum, S. L., and Kloster, S. (2010), Description and evaluation of the Model for Ozone and Related chemical Tracers, version 4 (MOZART-4), Geosci. Model Dev., *3*, 43–67, doi:10.5194/gmd-3-43-2010.

Fast, J. D., et al. (2006), Evolution of ozone, particulates, and aerosol direct forcing in an urban area using a new fully-coupled meteorology, chemistry, and aerosol model, *J. Geophys. Res., 111,* D21305.

Fischer, H., et al. (2000), Tracer correlation in the northern high latitude lowermost stratosphere: Influence of cross-tropopause mass exchange, *Geophys. Res. Lett., 27*(1), 97-100.

Fischer, H., et al. (2003), Deep convective injection of boundary layer air into the lowermost stratosphere at midlatitudes, *Atmos. Chem. Phys., 3*(3), 739-745.

Forster, P. M. F., and K. P. Shine (1999), Stratospheric water vapour changes as a possible contributor to observed stratospheric cooling, *Geophys. Res. Lett.*, *26*(21), 3309–3312.

Fovell, R., D. Durran, and J. Holton (1992), Numerical simulations of convectively generated stratospheric gravity waves, *J. Atmos. Sci., 49*(16), 1427-1442.

Fried, A., et al. (2008), Role of convection in redistributing formaldehyde to the upper troposphere over North America and the North Atlantic during the summer 2004 INTEX campaign, *J. Geophys. Res.*, *113*(D17306), doi:10.1029/2007JD009760.

Fritz, S., and I. Laszlo (1993), Detection of water vapor in the stratosphere over very high clouds in the tropics, *J. Geophys. Res., 98*(D12), 22959-22967.

Fueglistaler, S., et al. (2009), Tropical tropopause layer, *Rev. Geophys., 47*(1), doi:10.1029/2008RG000267.

Gerbig, C., S. Schmitgen, D. Kley, A. Volz-Thomas, K. Dewey, and D. Haaks (1999), An improved fast-response vacuum-UV resonance fluorescence CO instrument, *J. Geophys. Res.*, *104*(D1), 1699–1704.

Gettleman, A., Hoor, P., Pan, L. L., Randel, W. J., Hegglin, M. I., and T. Birner (2011), The extratropical upper troposphere and lower stratosphere, *Rev. Geophys., 49*(3), doi:10.1029/2011RG000355.

Ginoux, P., M. Chin, I. Tegen, J. Prospero, B. Holben, O. Dubovik, and S-J. Lin, 2001: Sources and distributions of dust aerosols simulated with the GOCART model. *J. Geophys. Res*, *106*, 20225–20273

Gray, S. L. (2003), A case study of stratosphere to troposphere transport: The role of convective transport and the sensitivity to model resolution, *J. Geophys. Res., 108*(D18), 4590.

Grell, G. A., et al. (2005), Fully coupled "online" chemistry in the WRF model, *Atmos. Environ., 39,* 6957 – 6976.

Guenther, C. C., T. Karl, P. Harley, C. Wiedinmyer, P. I. Palmer, and C. Green (2006), Estimates of global terrestrial isoprene emissions using MEGAN (Model of Emissions of Gases and Aerosols from Nature), *Atmos. Chem. Phys.*, *6*.

Hanisco, T. F., et al. (2007), Observations of deep convective influence on stratospheric water vapor and its isotopic composition, *Geophys. Res. Lett., 34*(L04814).

Hassim, M. E. E. and T. P. Lane (2010), A model study on the influence of overshooting convection on TTL water vapour, *Atmos. Chem. Phys., 10,* 9833-9849.

Hegglin, M. I., et al. (2004), Tracing troposphere-to-stratosphere transport above a mid-latitude deep convective system, *Atmos. Chem. Phys., 4*(3) 741- 756.

Hintsa, E. J., et al. (1998), Troposphere-to-stratosphere transport in the lowermost

stratosphere from measurements of H_2O, CO_2, N_2O and O_3, *Geophys. Res. Lett., 25*(14), 2655-2658.

Hodzic, A. and J. L. Jimenez (2011), Modeling anthropogenically controlled secondary organic aerosols in a megacity: a simplified framework for global and climate models, *Geosci. Model Dev., 4*, 901-917, doi:10.5194/gmd-4-901-2011.

Hoerling, M. P., T. K. Schaack, and A. J. Lenzen (1993), A global analysis of stratospheric-tropospheric exchange during northern winter, *Mon. Wea. Rev., 121,* 162-172.

Holton, J. R., P. H. Haynes, M. E. McIntyre, A. R. Douglass, R. B. Rood, and L. Pfister (1995), Stratosphere-troposphere exchange, *Rev. Geophys*., *33*(4), 403–439, doi:10.1029/95RG02097.

Homeyer, C. R., K. P. Bowman, L. L. Pan, E. L. Atlas, R. -S. Gao, and T. L. Campos (2011), Dynamical and chemical characteristics of tropospheric intrusions observed during START08, *J. Geophys. Res.*, *116*(D06111), doi:10.1029/2010JD015098.

Homeyer, C. R. (2014), Formation of the enhanced-v infrared cloud top feature from high-resolution three-dimensional radar observations, *J. Atmos. Sci., 71*, 331 - 348.

Homeyer, C. R., et al. (2014), Convective transport of water vapor into the lower stratosphere observed during double-tropopause events, *J. Geophys. Res. Atmos., 119,* 10941-10958.

Homeyer, C. R. (2015), Numerical simulations of extratropical tropopause – penetrating convection: Sensitivities to grid resolution, *J. Geophys. Res. Atmos., 120,* 7174 – 7188.

Homeyer, C. R., and M. R. Kumjian (2015), Microphysical characteristics of overshooting convection from polarimetric radar observations, *J. Atmos. Sci., 72,* 870 – 891.

Homeyer, C. R., J. D. McAuliffe, and K. M. Bedka (2017), On the development of above-anvil cirrus plumes in extratropical convection, *J. Atmos. Sci.,* doi:10.1175/JAS-D-16-0269.1.

Hong, S-Y., and H-L. Pan (1996), Nonlocal boundary layer vertical diffusion in a medium-range forecast model, *Mon. Wea. Rev., 124,* 2322-2339.

Hong, S.-Y., Noh, Y., and Dudhia, J. (2006), A new vertical diffusion package with an explicit treatment of entrainment processes, *Mon. Wea. Rev., 134*.

Hoor, P., H. Fischer, L. Lange, J. Lelieveld, and D. Brunner (2002), Seasonal variations of a mixing layer in the lowermost stratosphere as identified by the CO-O_3 correlation from in situ measurements, *J. Geophys. Res., 107*(D5), 4044.

Hoskins, B. J., M. E. McIntyre, and A. W. Robertson (1985), On the use and significance of isentropic potential vorticity maps, *Q. J. R. Meteorol. Soc., 111*(470), 877-946.

Houze, R. A., Jr., B. F. Smull, and P. Dodge (1990), Mesoscale organization of springtime rainstorms in Oklahoma, *Mon. Wea. Rev*., *118*, 613-654.

Hsu, J., M. J. Prather, and O. Wild (2005), Diagnosing the stratosphere - to - troposphere flux of ozone in a chemistry transport model, *J. Geophys. Res.: Atmos., 110*(D19), https://doi.org/10.1029/2005JD006045.

Huey, L. G. (2007), Measurement of trace atmospheric species by chemical ionization mass spectrometry: Speciation of reactive nitrogen and future directions, *Mass Spectrom. Rev., 26*(2), 166-184, doi:10.1002/mas.20118.

Iacono, M. J., Delamere, J. S., Mlawer, E. J., Shepard, M. W., Clough, S. A., and Collins, W. D. (2008), Radiative forcing by long-lived greenhouse gases: Calculations with the AER radiative transfer models, *J. Geophys. Res., 113*(D13103).

Igel, A. L., M. R. Igel, and S. C. van den Heever (2015), Make it a double? Sobering results from simulations using single-moment microphysics schemes. *J. Atmos. Sci., 72*, 910 – 925, doi:http://dx.doi.org/10.1175/JAS-D-14-0107.1.

Johnson, W. B. and W. Viezee (1981), Stratospheric ozone in the lower troposphere – I. Presentation and interpretation of aircraft measurements, *Atmos. Environ., 15*(7), 1309-1323.

Jourdain, L., S. S. Kulawik, H. M. Worden, K. E. Pickering, J. Worden, and A. M. Thompson (2010), Lightning NO_X emissions over the USA constrained by TES ozone observation and the GEOS-Chem model, *Atmos. Chem. Phys., 10*, 107-119.

Kim, S. et al. (2007), Measurement of HO_2NO_2 in the free troposphere during the Intercontinental Chemical Transport Experiment-North America 2004, *J. Geophys. Res., 112*(D12S01), doi:10.1029/2006JD007676.

Konopka, P., and L. L. Pan (2012), On the mixing-driven formation of the Extratropical Transition Layer (ExTL), *J. Geophys. Res., 117*(D18301), doi:10.1029/2012JD017876.

Kunz, A., P. Konopka, R. Mueller, and L. Pan (2011), Dynamical tropopause based on isentropic PV gradients, *J. Geophys. Res., 116*(D01110), doi:10.1029/2010JD014343.

Lacis, A. A., D. J. Wuebbles, and J. A. Logan (1990), Radiative forcing of climate by changes in the vertical distribution of ozone, *J. Geophys. Res.: Atmos., 95*(D7), 9971-9981.

Lamarque, J.-F. and P. G. Hess (1994), Cross-tropopause mass exchange and potential vorticity budget in a simulated tropopause folding, *J. Atmos. Sci., 51*(15), 2246-2269.

Lane, T. P. (2008), The vertical response to penetrative convection and the associated gravity-wave generation, *Atmos. Sci. Lett., 9*(3), 103-110.

Lane, T. P. and R. D. Sharman (2006), Gravity wave breaking, secondary wave generation, and mixing above deep convection in a three-dimensional cloud model, *Geophys. Res. Lett., 33*(L23813), doi:10.1029/2006GL027.

Lane, T. P., and R. D. Sharman (2014), Intensity of thunderstorm-generated turbulence revealed by large-eddy simulation, *Geophys. Res. Lett., 41,* 2221 – 2227.

Lane, T. P., M. J. Reeder, and T. L. Clark (2001), Numerical modeling of gravity wave generation by deep tropical convection, *J. Atmos. Sci., 58*(10), 1249-1274.

Langford, A. O., and Reid, S. J. (1998), Dissipation and mixing of a small - scale stratospheric intrusion in the upper troposphere, *J. Geophys. Res.*, *103*(D23), 31265– 31276.

Lelieveld, J. and F. J. Dentener (2000), What controls tropospheric ozone? *J. Geophys. Res.: Atmos., 105*(D3), 3531-3551.

Levy, H. (1973), Tropospheric budgets for methane, carbon monoxide, and related species, *J. Geophys. Res.: Oceans,* doi:10.1029/JC078i024p05325.

Lin, M., Fiore, A. M., Cooper, O. R., Horowitz, L. W., Langford, A. O., Levy, H., Johnson, B. J., Naik, V., Oltmans, S. J., and Senff, C. J. (2012), Springtime high surface ozone events over the western United States: Quantifying the role of stratospheric intrusions, *J. Geophys. Res.*, *117*(D00V22), doi:10.1029/2012JD018151.

Lindsey, D. T., and L. Grasso (2008), An effective radius retrieval for thick ice clouds using GOES, *J. Appl. Meteor. Clim., 47*, 1222-1231.

Liu, S. C., D. Kley, M. McFarland, J. D. Mahlman, H. Levy II (1980), On the origin of tropospheric ozone, *J. Geophys. Res.: Oceans, 85*(C12), 7546-7552.

Logan, J. A. (1985), Tropspheric ozone: Seasonal behavior, trends, and anthropogenic influence, *J. Geophys. Res.: Atmos, 90*(D6), 10463-10482.

Logan, J. A., et al. (1999), Trends in the vertical distribution of ozone: A comparision of two analyses of ozonesonde data, *J. Geophys. Res., 104*(D21), 26373-26399.

Long, R. (1970), Blocking effects in flow over obstacles, Tellus, 22:5, 471-480, DOI: 10.3402/tellusa.v22i5.1024

Jaeglé, L., D. J. Jacob, W. H. Brune, D. Tan, I. C. Faloona, A. J. Weinheimer, B. A. Ridley, T. L. Campos, and G. W. Sachse (1998), Sources of HO_X and production of ozone in the upper troposphere over the United States, 1709-1712, doi:10.1029/98GL00041.

Jung, Y., G. Zhang, and M. Xue (2008), Assimilation of simulated polarimetric radar data for a convective storm using ensemble Kalman filter. Part I: Observation operators for reflectivity and polarimetric variables, *Mon. Wea. Rev.*, *136*, 2228-2245.

LeTexier, H., S. Solomon, and R. R. Garcia (1988), The role of molecular hydrogen and methane oxidation in the water vapour budget of the stratosphere, *Q. J. R. M. Soc., 144*(480), doi: 10.1002/qj.49711448002.

Maddox, E. M. and G. L. Mullendore (2018), Determination of best tropopause definition for convective transport studies, *J. Atmos. Sci.,* doi:10.1175/JAS-D-18-0032.1.

Mansell, E. R., Ziegler, C. L., and Bruning, E. C. (2010), Simulated Electrification of a small thunderstorm with two-moment bulk microphysics, *J. Atmos. Sci., 67*.

Martin, D. W., R. A. Kohrs, F. R. Mosher, C. M. Medaglia, and C. Adamo (2008), Over-ocean validation of the Global Convective Diagnostic, J. Appl. Meteor. Climatol., 47, 525-543.

Milbrandt, J. A. and M. K. Yau (2005), A Multimoment Bulk Microphysics Parameterization. Part I: Analysis of the Role of the Spectral Shape Parameter. *J. Atmos. Sci., 62*(9), 3051-3064.

Morrison, H., J. A. Curry, and V. I. Khvorostyanov (2005), A new double-moment microphysics parameterization for application in cloud and climate models. Part1: Description, *J. Atmos. Sci., 62,* 1665-1677.

Mote, P. W., et al. (1996), An atmospheric tape recorder: The imprint of tropical tropopause temperatures on stratospheric water vapor, *J. Geophys. Res. 101*(D2), 3989, doi:10.1029/95JD03422.

Mullendore, G. L., D. R. Durran, and J. R. Holton (2005), Cross-tropopause tracer transport in midlatitude convection, *J. Geophys. Res., 110*(D06113).

National Center for Atmospheric Research (2013), XPMS2D User's Guide. [Available at

http://www.eol.ucar.edu/raf/Software/xpms2d.html.]

Neu, J. L. and M. J. Prather (2012), Toward a more physical representation of precipitation scavenging in global chemistry models: cloud overlap and ice physics and their impact on tropospheric ozone, *Atmos. Chem. Phys.,* 3289-3310, doi:10.5194/acp-12-3289-2012.

Newman, P. A. and M. R. Scoeberl (1995), A reinterpretation of the data from the NASA stratosphere-troposphere exchange project, *Geophys. Res. Lett., 22*(18), 2501-2504.

Noh, Y., W. G. Cheon, S-Y. Hong, and S. Raasch (2003), Improvement of the K-profile model for the planetary boundary layer based on large eddy simulation data, *Bound.-Layer Meteor., 107,* 401-427.

O'Connor, F. M., G. Vaughan, and H. De Backer (1999), Observations of subtropical air in the European mid-latitude lower stratosphere, *Q. J. R. Meteorol. Soc., 125,* 2965-2986.

Olsen, M. A., et al. (2008), HIRDLS observations and simulation of a lower stratospheric intrusion of tropical air to high latitudes, *Geophys. Res. Lett., 35*(L21813).

Olsen, M. A., et al. (2010), Interannual variability of ozone in the winter lower stratosphere and relationship to laminar and irreversible transport, *J. Geophys. Res., 115*(D15305).

Pan, L. L., W. J. Randel, B. L. Gary, M. J. Mahoney, and E. J. Hintsa (2004), Definitions and sharpness of the extratropical tropopause: A trace gas perspective, *J. Geophys. Res., 109*(D23103), doi:10.1029/2004JD004982.

Pan, L. L., W. J., J. C. Gille, W. D. Hall, B. Nardi, S. Massie, V. Yudin, R. Khosravi, P. Konopka, and D. Tarasick (2009), Tropospheric intrusions associated with the secondary tropopause, *J. Geophys. Res.*, *114*(D10302), doi:10.1029/2008JD011374.

Pan, L. L., et al. (2010), The Stratosphere - Troposphere Analyses of Regional Transport 2008 experiment, *Bull. Am. Meteorol. Soc.*, *91*, 327– 342.

Pan, L. L., et al. (2014), Thunderstorms enhance tropospheric ozone by wrapping and shedding stratospheric air, *Geophys. Res. Lett., 41,* 7785 – 7790.

Pickering, K. E., and Coauthors (1990), Model calculations of tropospheric ozone production potential following observed convective events, *J. Geophys. Res.: Atmos., 95*(D9), 14049-14062, doi:10.1029/JD095iD0p14049.

Phoenix, D. B., C. R. Homeyer, and M. C. Barth (2017), Sensitivity of simulated

convection-driven stratosphere-troposphere exchange in WRF-Chem to the choice of physical and chemical parameterization, *Earth and Space Science, 4*, 454-471, doi:10.1002/2017EA000287.

Phoenix, D.B., C. R. Homeyer, M. C. Barth, and S. B. Trier (2019), Mechanisms responsible for stratosphere-to-troposphere transport around a mesoscale convective system anvil, *J. Geophys. Res.: Atmos.,* submitted.

Pleim, J. E. (2007a), A combined local and nonlocal closure model for the atmospheric boundary layer. Part I: Model description and testing, *J. Appl. Meteor. Climatol., 46,* 13-83-1395.

Pollack, I. B., et al. (2016), Airborne quantification of upper tropospheric NOx production from lightning in deep convective storms over the United States Great Plains, *J. Geophys. Res. Atmos., 121,* 2002-2028, doi:10.1002/2015JD023941.

Poulida, O., Dickerson, R. R., and Heymsfield, A. (1996), Stratosphere troposphere exchange in a midlatitude mesoscale convective complex, *J. Geophys. Res.*, *101*, 6823–6836, doi:10.1029/95JD03523.

Price, J. D. and G. Vaughan (1993), The potential for stratosphere-troposphere exchange in cut-off-low systems, *Q. J. R. Meteorol. Soc., 119*, 343-365.

Ramanathan, V. and Dickinson, R. E., (1979), The role of stratospheric ozone in the zonal and seasonal radiative energy balance of the Earth-troposphere system, *J. Atmos. Sci., 36,* 1084-1104.

Randel, W. J., et al. (2010), Asian monsoon transport of pollution to the stratosphere, *Science, 328,* 611-613.

Ray, E. A., et al. (2004), Evidence of the effect of summertime midlatitude convection on the subtropical lower stratosphere from CRYSTAL-FACE tracer measurements, *J. Geophys. Res., 109*, D18304.

Ridley, B. A., F. E. Grahek, and J. G. Walega (1992), A small high-sensitivity, medium-response ozone detector suitable for measurements from light aircraft, *J. Atmos. Oceanic Technol., 9*(2), 142-148, doi:10.1175/1520-0426(1992)<0142:ASHSMR>2.0.CO;2.

Ridley, B., J. G. Walega, J. E. Dye, and F. E. Grahek (1994), Distributions of NO, NO_X, NO_Y, and O_3 to 12 km altitude during the summer monsoon season over New Mexico, *J. Geophys. Res., 99*, 25519-25534, doi:10.1029/94JD02210.

Ridley, B., and Coauthors (2004), Florida thunderstorms: A faucet of reactive nitrogen to the upper troposphere, *J. Geophys. Res., 109*(D17305), doi:10.1029/2004JD004769

Rohs, S., et al. (2006), Long-term changes of methane and hydrogen in the stratosphere in the period 1978–2003 and their impact on the abundance of stratospheric water vapor, *J. Geophys. Res., 111*(D14315), doi:10.1029/2005JD006877.

Rosenfeld, D., et al. (2008), Satellite detection of severe convective storms by their retrieved vertical profiles of cloud particle effective radius and thermodynamic phase, *J. Geophys. Res., 113*(D04208), doi:10.1029/2007JD008600.

Rossby, C. G. (1940), Planetary flow patterns in the atmosphere, *Q. J. R. Meteorol. Soc., 66,* suppl., 68-87.

Ryerson, T. B., L. G. Huey, K. Knapp, J. A. Neuman, D. D. Parrish, D. T. Sueper, and F. C. Fehsenfeld (1999), Design and intial characterization of an inlet for gas-phase NO*y* measurements from aircraft, *J. Geophys. Res.*, *104*(D5), 5483–5492.

Sandu, R. and Sander, R (2006), Technical note: Simulating chemical systems in Fortran90 and Matlab with the Kinetic PreProcessor KPP-2.1, *Atmos. Chem. Phys., 6*, 187-195, doi: 10.5194/acp-6-187-2006.

Schell, B., I. J. Ackermann, H. Hass, F. S. Binkowski, and A. Ebel, (2001), Modeling the formation of secondary organic aerosol within a comprehensive air quality model system. *J. Geophys. Res. Atmos., 106*(D22), 28275-28293.

Schmetz, J., S. A. Tjemkes, M. Gube, and L. van de Berg (1997), Monitoring deep convection and convective overshooting with Meteosat, *Adv. Space Res.*, *19*, 433–441, doi:https://doi.org/10.1016/S0273-1177(97)0005.

Setvak, M., R. M. Rabin, and P. K. Wang (2007), Contribution of the MODIS instrument to observations of deep convective storms and stratospheric moisture detection in GOES and MSG imagery, *Atmos. Res., 83,* 505-518.

Shapiro, M. A. (1980), Turbulent mixing within tropopause folds as a mechanism for the exchange of chemical constituents between the stratosphere and troposphere, *J. Atmos. Sci.*, *37*, 994– 1004.

Sherwood, S. C. and Dessler, A. E. (2001), A model for transport across the tropical tropopause, *J. Atmos. Sci. 58,* 765.

Shindell, D. T. (2001), Climate and ozone response to increased stratospheric water vapor, *Geophys. Res. Lett. 28,* 1551, doi:10.1029/1999GL011197.

Skamarock, W. C., et al. (2008), A description of the advanced research WRF version 3, NCAR Technical Note, NCAR/TN-475+STR, 125 pp.

Solomon, S., Rosenlof, K. H., Portmann, R. W., Daniel, J. S., Davis, S. M., Sanford, T.

J., Plattner, G.-K. (2010), Contributions of stratospheric water vapor to decadal changes in the rate of global warming, *Science*, *327*(5970), 1219-1223, doi:10.1126/science.1182488.

Sprenger, M. and H. Wernli (2003), A northern hemispheric climatology of cross-tropopause exchange for the ERA15 time period (1979-1993), *J. Geophys. Res.: Atmos., 108*(D12).

Stenchikov, G., Dickerson, R., Pickering, K., Ellis, W., Doddridge, B., Kondragunta, S., Poulida, O., Scala, J., and Tao, W. - K. (1996), Stratosphere - troposphere exchange in a midlatitude mesoscale convective complex: 2. Numerical simulations, *J. Geophys. Res.*, *101*, 6837– 6851, doi:10.1029/95JD02468.

Stockwell, W. R., et al. (1997), A new mechanism for regional atmospheric chemistry modeling, *J. Geophys. Res., 102*, 25,847 – 25879.

Sukoriansky, S., B. Galperian, and V. Perov (2005), Application of a new spectral theory of stable stratified turbulence to the atmospheric boundary layer over sea ice, *Bound.-Layer Meteor., 117,* 231-257.

Tang, Q., Prather, M. J., and Hsu, J. (2011), Stratosphere - troposphere exchange ozone flux related to deep convection, *Geophys. Res. Lett.*, *38*(L03806), doi:10.1029/2010GL046039.

Thompson, A. M., G. S. Young, G. Morris, B. Johnson, S. Oltmans, and H. B. Selkirk (2016), SEACIONS During the 2012 Asian Monsoon: Stratgic approach to determining convective impacts on the tropospheric ozone and TTL gravity waves, *NASA Tech. Report.*

Thornton, D. C., A. R. Brandy, B. W. Blomquist, J. D. Bradshaw, and D. R. Blake (1997), Vertical transport of sulfur dioxide and dimethyl sulfide in deep convection and its role in new particle formation, *J. Geophys. Res. Atmos., 102*(D23), 28501-28509, doi: 10.1029/97JD01647.

Tilmes, S., et al. (2010), An aircraft-based upper troposphere lower stratosphere O_3, CO, and H2O climatology for the Northern Hemisphere, *J. Geophys. Res.: Atmos., 115*(D14), doi:10.1029/2009JD012731.

Trier, S. B. and R. D. Sharman (2009), Convection-permitting simulations of the environment supporting widespread turbulence within the upper-level outflow of a mesoscale convective system, *Mon. Wea. Rev.*, *137*, 1972-1990.

Trier, S. B., R. D. Sharman, R. G. Fovell, and R. G. Frehlich (2010), Numerical simulation of radial cloud bands within the upper-level outflow of an observed mesoscale convective system, *J. Atmos. Sci.*, *67*, 2990-2999.

Trier, S. B., R. D. Sharman, and T. P. Lane (2012), Impacts of moist convection on a cold- season outbreak of the clear-air turbulence (CAT), *Mon. Wea. Rev.*, *140*, 2477-2496.

Vaughan, G. and C. Timmis (1998), Transport of near-tropopause air into the lower midlatitude stratosphere, *Q. J. R. Meteorol. Soc., 124,* 1559-1578.

Vömel, H., D. David, and K. Smith (2007), Accuracy of tropospheric and stratospheric water vapor measurements by the cryogenic frost point hydrometer: Instrument details and observations, *J. Geophys. Res., 112*(D08305), doi:10.1029/2006JD007224.

Wang, P. K. (2003), Moisture plumes above thunderstorm anvils and their contributions to cross-tropopause transport of water vapor in midlatitudes, *J. Geophys. Res., 108*(D6), 4194.

Wang, W. C., Pinto, J. P., and Yung, Y. L. (1980), Climatic effects due to halogenated compounds in the Earth's atmosphere, *J. Atmos. Sci*., 37, 333-338.

Waugh, D. W. (2005), Impact of potential vorticity intrusions on subtropical upper tropospheric humidity, *J. Geophys. Res., 110*(D11305).

Waugh, D. W. and L. M. Polvani (2000), Climatology of intrusions into the tropical upper troposphere, *Geophys. Res. Lett., 27*(23), 3857-3860.

Wild, O., X. Zhu, and M. J. Prather (2000), Fast-J: Accurate simulation of in-and below-cloud photolysis in tropospheric chemical models. *J. Atmos. Chem.*, *37*(3), 245-282.

World Meteorological Organization (1957), Definition of the tropopause, *WMO Bull., 6,* 136.

World Meteorological Organization (WMO), The stratosphere 1981 (1982): Theory and measurements, Rep. 11, 516 pp., WMO Global Ozone Res. And Monit. Proj., Geneva.

World Meteorological Organization (WMO), Atmospheric ozone 1985 (1986), vol. III, Rep. 16, 1095 pp., WMO Global Ozone Res. And Monit. Proj., Geneva.

Zaveri, R. A. and L. K. Peters (1999), A new lumped structure photochemical mechanism for large-scale applications, *J. Geophys. Res., 104*(D23)*,* 30,387-30,415.

Zaveri, R. A., R. C. Easter, J. D. Fast, and L. K. Peters (2008), Model for simulating aerosol interactions and chemistry, *J. Geophys. Res. Atmos., 113*(D13).

Zondlo, M. A., M. E. Paige, S. M. Massick, and J. A. Silver (2010), Vertical cavity laser hygrometer for the national science foundation gulfstream-V aircraft, *J. Geophys. Res*., *115*(D20309), doi:10.1029/2010JD014445.